The tilt and twist of emerging solar active regions

Dissertation
zur Erlangung des mathematisch-naturwissenschaftlichen Doktorgrades

“Doctor rerum naturalium”

der Georg-August-Universität Göttingen

im Promotionsstudiengang Physik
der Georg-August University School of Science (GAUSS)

vorgelegt von

Christian Baumgartner

aus Wolfsberg, Österreich

Göttingen, 2021

Betreuungsausschuss

Prof. Dr. Laurent Gizon
Max-Planck-Institut für Sonnensystemforschung und
Institut für Astrophysik, Georg-August-Universität Göttingen, Deutschland

Dr. Aaron C. Birch
Max-Planck-Institut für Sonnensystemforschung, Göttingen, Deutschland

Dr. Natalie Krivova
Max-Planck-Institut für Sonnensystemforschung, Göttingen, Deutschland

Mitglieder der Prüfungskommision

Referent: Prof. Dr. Laurent Gizon
Max-Planck-Institut für Sonnensystemforschung und
Institut für Astrophysik, Georg-August-Universität Göttingen, Deutschland

Korreferent: Prof. Dr. Stefan Dreizler
Institut für Astrophysik, Georg-August-Universität Göttingen, Deutschland

Weitere Mitglieder der Prüfungskommission:

Prof. Dr. Wolfram Kollatschny
Institut für Astrophysik, Georg-August-Universität Göttingen, Deutschland

Prof. Dr. Hardi Peter
Max-Planck-Institut für Sonnensystemforschung, Göttingen, Deutschland

Prof. Dr. Ramin Yahyapour
Gesellschaft für wissenschaftliche Datenverarbeitung mbH Göttingen und
Institut für Informatik, Georg-August-Universität Göttingen, Deutschland

Prof. Dr. Thorsten Hohage
Institut für numerische und angewandte Mathematik, Göttingen, Deutschland

Tag der mündlichen Prüfung: 09.12.2021

Contents

Summary 13

Zusammenfassung 15

1 Introduction 17

1.1 Active regions 17
  1.1.1 The magnetic Sun 17
  1.1.2 Origin of magnetic fields in the solar atmosphere 17
  1.1.3 Definition of active regions 18
  1.1.4 Observed properties of active regions 18
1.2 Joy’s law 22
  1.2.1 Measurements of Joy’s law 22
  1.2.2 Origin of Joy’s law 23
1.3 Magnetic helicity 24
  1.3.1 Definition of magnetic helicity 24
  1.3.2 Self-helicity: twist and writhe 25
  1.3.3 Hemispheric helicity sign rule 26
  1.3.4 Origin of twist in flux tubes 27
  1.3.5 Twist estimation methods 28
  1.3.6 The connection between the tilt and twist of active regions 30
1.4 SDO/HMI 30
1.5 Motivation of the thesis 31
1.6 Structure of the thesis 32

2 Average motion of emerging solar active region polarities: Joy’s law 33

2.1 Abstract 33
2.2 Introduction 34
2.3 Measuring the tilt angle of the polarities 35
2.4 Tilt angle as a function of active region evolution 36
2.5 Scatter of the tilt angle as a function of time and flux 37
2.6 Tilt angle and separation as a function of latitude 39
2.7 Discussion of the Coriolis effect 40
2.8 Implications for the tilt angle relaxation 41
2.9 Summary and discussion 43
2.10 Appendix 44
  2.10.1 Polarity centres identified by shifting the search mask for AR 11072 44

2.10.2 Polarity centres identified in high-resolution maps 45
2.10.3 Modelling the latitudinal separation between polarities during emergence 47

3 Impact of spatially correlated fluctuations in sunspots on metrics related to magnetic twist 55
3.1 Abstract 55
3.2 Introduction 56
3.3 SDO/HMI vector magnetogram observations of our reference sunspot in active region NOAA 11072 58
3.4 Estimating the spatial covariance of magnetic field fluctuations from the observations 58
3.5 A model for the reference sunspot 61
3.6 Summary and implementation of twist measurement methods 65
3.6.1 The twist proxy α 65
3.6.2 Average twist 65
3.6.3 Peak twist 66
3.6.4 Twist density 66
3.7 Example sunspot model with correlated magnetic field fluctuations compared to HMI observations 67
3.7.1 The vector magnetic field 67
3.7.2 The magnetic field's twist 67
3.8 Sensitivity of twist measurements to correlated temporal fluctuations of the magnetic field 69
3.9 Summary and Conclusion 74
3.10 Appendix 76
3.10.1 Vector transformation 76
3.10.2 Possible causes for the measured spatial correlation of magnetic field fluctuations 77
3.10.3 Derivatives with different stencil sizes 77
3.10.4 Using Stokes' theorem for calculating J_z 79
3.10.5 Comparison of different stencil sizes for calculating J_z 79
3.10.6 Interpretation of α_z 82

4 Twist measurements in emerging active regions 85
4.1 Data and methods 85
4.2 Examples of twist measurements in two active region observations 86
4.3 Measuring the hemispheric helicity sign rule 87
4.4 Evolution of twist in the leading and following polarity of emerging active regions 92
4.5 Vertical current and twist in an averaged polarity patch 93
4.6 Summary and Discussion 97

5 Discussion and outlook 101
5.1 Joy's law 101
5.2 Interpretation of α_z 101

5.3 Measurements of twist and vertical currents in HMI observations 102

Bibliography **105**

A List of active regions used in chapter 4 **117**

Scientific contributions **119**

Acknowledgements **121**

Curriculum vitae **123**

List of Figures

1.1 Vector magnetic field and continuum observation by SDO/HMI of NOAA AR 11080 . . . 19
1.2 SDO/HMI continuum observation of NOAA AR 11072's leading sunspot 19
1.3 The butterfly diagram and averaged daily sunspot coverage . . . 21
1.4 The magnetic butterfly diagram . . . 21

2.1 Sketch of the orientation of a pair of polarities with a positive tilt angle in the northern hemisphere . . . 37
2.2 Averaged tilt angle and standard deviation of the tilt angle of the polarities as a function of time . . . 38
2.3 East-west separation, north-south separation, and tilt angle of the polarities as a function of latitude at the emergence time and two days later . . . 40
2.4 Separation velocity of the polarities in the east-west direction and the north-south direction at the emergence time as a function of latitude . . . 42
2.5 Change in tilt angle between 2.1 days and 0.1 days as a function of the tilt angle at the emergence time . . . 43
2.6 Comparison of polarity centres identified by shifting the magnetic field maps and shifting the search mask for AR 11072 . . . 46
2.7 Example of line-of-sight magnetic field maps and identified locations of the positive (following) polarity at `TI+09` and `TI+10` of NOAA AR 11072 47
2.8 Average position of 153 positive and negative polarities relative to the corrected centre of the map from -18.4 hours before the emergence time, until 2.1 days after . . . 48
2.9 High-resolution time-averaged line-of-sight magnetogram maps of AR 11066, AR 11158, and AR 11414 . . . 49
2.10 Average position of the polarities from -18.4h before the emergence time, until 2.1 days after . . . 50
2.11 Median separation and tilt angle of 95 EARs with valid measurements of their location at all times from 0.1 to 2.1 days after the emergence . . . 52
2.12 Change in east-west separation, north-south separation, and change in tilt angle in the first two days after emergence as a function of latitude . . . 53

3.1 SDO/HMI vector magnetogram of active region active region NOAA 11072's leading sunspot . . . 59

3.2 SDO/HMI vector magnetogram of active region NOAA 11072's leading sunspot with the horizontal field plotted as arrows on top of the vertical vector component . . . 60
3.3 Sketch of the detrending process . . . 60
3.4 Average spatial correlation of the detrended time series of a pixel within the leading sunspot of active region NOAA 11072 relative to its neighbors 62
3.5 Example realizations of magnetic field fluctuations for each vector component . . . 63
3.6 Comparison of the magnetic vector field components between the HMI observations of active region NOAA 11072 and the model with and without magnetic field fluctuations . . . 64
3.7 Comparison of α_z maps measured from the original HMI observation, the model with and without fluctuations of the magenetic field . . . 68
3.8 The temporal evolution of α_z in the leading sunspot of active region NOAA 11072 . . . 70
3.9 The temporal evolution of the sign of α_z in the leading sunspot of active region NOAA 11072 . . . 71
3.10 HMI continuum image of the leading sunspot of active region NOAA 11072 72
3.11 Monte-Carlo simulation results for methods using the differential approach for calculating J_z . . . 73
3.12 Monte-Carlo simulation results when α_z is spatially averaged over the whole sunspot using the differential approach for calculating J_z . . . 74
3.13 Normalized point spread function for HMI . . . 78
3.14 Cuts through the average spatial correlation profile of neighboring pixels and the normalized estimated PSF . . . 78
3.15 Monte-Carlo simulation results for methods based on α_z when Stokes' theorem is used for calculating J_z . . . 80
3.16 Monte-Carlo simulation results for methods based on α_z spatially averaged over the whole sunspot and when Stokes' theorem is used for calculating J_z . . . 80

4.1 SDO/HMI vector magnetic field observation of active region 11080 . . . 88
4.2 Continuum, vertical current and α_z maps of active region 11080 . . . 89
4.3 SDO/HMI vector magnetic field observation of active region 11158 . . . 90
4.4 Continuum, vertical current and α_z maps of active region 11158 . . . 91
4.5 Spatial average of α_z weighted by B_z^2 of active regions versus solar latitude 92
4.6 Spatial average of α_z weighted by B_z^2 over all active region's negative and positive polarities as well as averages over both polarities in the northern and southern hemisphere versus time relative to emergence . . . 94
4.7 Vector magnetic field components of the averaged leading polarity based on 152 active regions . . . 96
4.8 Profile of the vertical current J_z in the averaged leading polarity at different times relative to emergence . . . 97
4.9 Profile of α_z in the average leading polarity at different times relative to emergence . . . 98

4.10 Maps of the vertical current J_z of the average leading polarity in different longitude bins . . . 99
4.11 The angle of the connection line between positive and negative centers of mass (J_z) in the averaged leading polarity relative to the east-west direction as a function of longitude . . . 100

List of Tables

3.1 Comparison of the different twist calculation methods between the model reference without any fluctuations of the magnetic field and the Monte-Carlo simulations when using derivatives for calculating J_z 74
3.2 Weighting factors and normalization factors for stencil sizes of 7, 5 and 3 pixels when using Savitzky-Golay filter for derivatives 79
3.3 Comparison of the different twist calculation methods between the model reference without any fluctuations of the magnetic field and the Monte-Carlo simulations when using integration for calculating J_z 81
3.4 Monte-Carlo simulation results for using derivatives to calculate α_z with different stencil sizes 81
3.5 Monte-Carlo simulation results for using integration to calculate α_z with different stencil sizes 81

Summary

The aim of this thesis is to characterize the tilt and twist of the emerging magnetic field in the solar photosphere, which play an important role in understanding the origin and dynamics of the solar magnetic field. The tilt refers to Joy's law, the latitude dependent inclination of solar active regions relative to the east-west direction. The second observable is the magnetic field's twist, which measures how often magnetic field lines wind around each other.

The first study focuses on Joy's law. We used the helioseismic emerging active region survey (HEAR, Schunker et al. 2016) to measure the temporal evolution of Joy's law in line-of-sight magnetograms during the emergence of 182 active regions. We found that on average active regions emerge with zero tilt. The leading and following polarities have an inherit north-south separation speed of unknown origin, which causes Joy's law to develop within one to two days after emergence. These findings are not expected by a popular theory according to which the Coriolis force creates the tilt by acting on plasma flows contained within the rising magnetic field before emergence at the solar surface. Other explanations for Joy's law may be linked to the magnetic field's twist and the conservation of magnetic helicity.

We need robust quantitative measurements of the magnetic field's twist to constrain theories of magnetic flux emergence. In the second study, we test the sensitivity of various twist proxies to a fluctuating magnetic field. We modelled a sunspot's magnetic field and its fluctuations based on a time series of HMI/SDO vector magnetic field observations of the leading sunspot in active region NOAA 11072. We found that the magnetic field's temporal fluctuations are spatially correlated on scales up to 1.4 Mm, which is more than expected from the instrument's point spread function alone. We used Monte-Carlo simulations of this sunspot model with different realizations of field fluctuations and found that most twist proxies can be robustly measured with errors that are typically one order of magnitude smaller than the model's inherent twist.

In the third study, we extend the characterization of the twist proxy α_z, which measures the ratio of the vertical current to the vertical magnetic field, to vector magnetic field measurements in emerging active regions of the HEAR survey. The hemispheric helicity sign rule, which states that the magnetic field has a preferential orientation of twist with opposite direction in the northern and southern hemisphere, can be retrieved from the data set, when α_z is spatially averaged over whole active regions. Averages over the leading and following polarities have opposite signs, which is inconsistent with theories that the polarities are connected by uniformly twisted flux tubes. A closer inspection of the averaged leading polarity revealed a dependence of its α_z profile on its longitudinal position relative to the Sun's central meridian. The source of this systematic effect and how it affects the twist measurements must be further studied.

Zusammenfassung

Ziel dieser Arbeit ist es, die Neigung und Verwindung des solaren Magnetfeldes zu charakterisieren, welche eine wichtige Rolle im Verständis über den Ursprung und Dynamik des Magnetfeldes spielen. Die Neigung bezieht sich auf das Gesetz von Joy, das die von der heliographischen Breite abhängige Neigung von aktiven Regionen relativ zur Ost-West-Richtung beschreibt. Die zweite Größe ist die Verwindung des Magnetfeldes, welche misst, wie oft sich magnetische Feldlinien umeinander wickeln.

Die erste Studie konzentriert sich auf das Gesetz von Joy. Wir haben die HEAR Studie (Schunker et al. 2016) verwendet, um die zeitliche Entwicklung des Joy'schen Gesetzes in "line-of-sight" Magnetogrammen während der Entstehung von 182 aktiven Regionen zu messen. Wir fanden heraus, dass aktive Regionen beim Auftauchen im Durchschnitt nicht geneigt sind. Die führende und nachfolgende Polarität werden in Nord-Süd-Richtung auseinandergetrieben und das Gesetz von Joy wird innerhalb von 1-2 Tagen nach dem Auftauchen sichtbar. Der treibende Grund für diese Trennung ist nicht klar. Dieses Ergebnis widerspricht einer gängigen Theorie, wonach die Corioliskraft die Neigung vor dem Auftauchen des Magnetfeldes an der Sonnenoberfläche erzeugt, indem sie auf Plasmaströme innerhalb des aufsteigenden Magnetfeld wirkt. Andere Erklärungen für das Gesetz von Joy können mit der Verwindung des Magnetfeldes und der Erhaltung der magnetischen Helizität zusammenhängen.

Wir benötigen robuste quantitative Messungen der Verdrehung des Magnetfelds, um Theorien über die Entwicklung des Magnetfeldes zu überprüfen. In der zweiten Studie testen wir die Empfindlichkeit verschiedener Näherungswerte (Proxies) für die Magnetfeld-Verwindung in einem fluktuierendem Magnetfeld. Wir modellierten das Magnetfeld und dessen Fluktuationen anhand einer Zeitserie des führenden Sonnenflecks in der aktiven Region NOAA 11072 basierend auf HMI/SDO-Vektormagnetfeldbeobachtungen. Wir haben festgestellt, dass die zeitlichen Fluktuationen des Magnetfeldes auf räumlichen Skalen bis zu 1.4 Mm korreliert sind. Dies ist mehr als von der Punktspreizfunktion des Instruments erwartet wird. Wir haben Monte-Carlo Simulationen des Sonnenfleck-Modells mit unterschiedlichen Realisationen von Magnetfeld-Fluktuationen durchgeführt. Es zeigt sich, dass die meisten Verwindungs-Proxies robust gemessen werden können. Sie zeigen typischerweise Fehler, die eine Größenordnung kleiner sind als die bekannte Verwindung des Modells.

In der dritten Studie charakterisieren wir den Verwindungs-Proxy α_z in Magnetfeldbeobachtungen der HEAR Studie, welcher das Verhältnis von vertikalem Strom zu vertikalem Magnetfeld misst. Die hemisphärische Helizitätsvorzeichenregel (HHVR) besagt, dass die Verdrehung des Magnetfeldes eine bevorzugte Orientierung mit unterschiedlichem Vorzeichen in der nördlichen und südlichen Sonnenhemisphäre hat. Die HHVR kann aus dem Datensatz abgeleitet werden kann, wenn α_z räumlich über ganze aktive Regionen

gemittelt wird. Die Mittelwerte über die führende und die folgende Polarität haben entgegengesetzte Vorzeichen, was der Theorie widerspricht, dass die Polaritäten durch gleichmäßig gewundene Flussröhren verbunden sind. Die nähere Untersuchung einer gemittelten führenden Polarität ergab eine Abhängigkeit ihres α_z-Profils von ihrer longitudinalen Position relativ zum zentralen Meridian der Sonne. Die Quelle dieses systematischen Effekts und seine Auswirkungen auf die Messungen der Magnetfeldverwindung müssen weiter untersucht werden.

1 Introduction

1.1 Active regions

1.1.1 The magnetic Sun

The first hints of the presence of magnetic fields on the Sun come from dark areas on its surface, so-called sunspots. They are the Sun's most prominent features, which can sometimes even be seen with naked eye (Keller and Friedli 1992). Therefore, the existence of sunspots was already known in ancient China, documented in "the book of change" in about 800 B.C. (Xu 1980), although it was not understood what causes them until many centuries later. With the invention of telescopes at the beginning of the 17th century, systematic studies of sunspots started. Hale (1908) studied the light spectra of the Sun and was the first to suggest the existence of magnetic fields in sunspots, when he observed split spectral lines, which he attributed to the Zeeman effect (Zeeman 1897). Since then, it is well established that the Sun's magnetic field not only impacts many observed phenomena on the Sun itself, but its influence also extends far into interplanetary space. Yet, many aspects about its origin and dynamics are not fully understood.

1.1.2 Origin of magnetic fields in the solar atmosphere

The solar magnetic field is produced by dynamo processes in the outermost Section of the solar interior, the convection zone, which extents from about 0.7 solar radii to the Sun's surface. Various theories exist about how these dynamo processes work and where in the convection zone the magnetic field is produced, but there is no conclusive picture yet. The prevalent theory (e.g. Parker 1993) is that the magnetic field is produced and stored at the base of the convection zone at the tachocline. The tachocline is a transition region separating the radiative and convective zone at about 0.7 solar radii, where the Sun's rotation profile changes from rigid in the radiative zone to differential in the convective zone. The differential rotation profile describes that the Sun fully rotates at the equator approximately every 25 days and progressively slower at higher latitudes (Schou et al. 1998).

Parker (1975) suggests, when enough magnetic field is accumulated at the tachocline, a coherent bundle of magnetic field, also called magnetic flux tube, starts to rise due to magnetic buoyancy. To explain magnetic buoyancy, we assume high plasma-β, i.e. the gas pressure (p_{gas}) is significantly higher than the magnetic pressure (p_B) and directs the motion of plasma and magnetic field. The pressure equilibrium of the flux tube is defined by

$$p_{\text{gas,int.}} + p_{\text{B}} = p_{\text{gas,ext.}}, \tag{1.1}$$

where $p_{\text{gas,int.}}$ and $p_{\text{gas,ext.}}$ describes the internal and external gas pressure with respect to the flux tube. If the whole system is in thermal equilibrium, the flux tube's internal gas pressure and consequently plasma density has to be lower compared to the surroundings, due to the additional magnetic pressure in the interior. The density imbalance creates an upwards directed force and the flux tube rises buoyantly towards the surface, where strong magnetic flux concentrations emerge into the photosphere to create active regions.

1.1.3 Definition of active regions

Active regions are a manifestation of the solar magnetic field. The name comes from the wide variety of dynamic events that occur within these regions, which range from small brightenings to huge energy releases, called flares, and coronal mass ejections.

Driel-Gesztelyi and Green (2015) defines active regions as the set of all observable phenomena at wavelengths from radio to γ-rays in the whole solar atmosphere that are caused by the emergence and evolution of strong magnetic flux ($\geq 10^{20}$ Mx). The National Oceanic and Atmospheric Administration (NOAA) adds an additional criterion: Emerging magnetic flux has to produce at least one sunspot that can be observed in white-light (= continuum) in the photosphere.

The simplest field configuration for an active region is a bipolar one, as shown by the example of NOAA AR 11080 vector magnetic field observations in the left panel of Fig. 1.1. The vector magnetic field in active regions is often described in a local Cartesian coordinate system, where the B_x and B_y components are located in a plane parallel to the solar surface and point from east to west and south to north, respectively. B_z is the vector component perpendicular to the surface. By definition, the B_z component of the magnetic field points away from the Sun in the positive (white) polarity and inward in the negative (black) polarity.

The right panel of Fig. 1.1 shows sunspots of the active region in a continuum image. Sunspots are the result of strong magnetic flux hindering the convection of the highly ionized plasma in the convection zone below the photosphere. This leads to cooling of the plasma confined within the magnetic field and consequently less thermal emission and a darker appearance in continuum observations compared to the surrounding plasma. Fig. 1.2 displays a well established sunspot of NOAA AR 11072. It shows the typical structure of well established sunspots with a dark central area, called umbra, and a slightly brighter annular area, the penumbra, that surrounds the umbra. It is important to note, while sunspots are a consequence of strong magnetic flux concentrations, they are not necessarily observable at the same time as magnetic flux emerges in the photosphere. They usually appear later, when enough flux is accumulated.

1.1.4 Observed properties of active regions

The magnetic complexity of active regions can drastically increase after multiple flux emergences occur in close vicinity, if compared to the simple bipolar configuration shown in Fig. 1.1. Nevertheless, various statistical properties of emerged magnetic field and

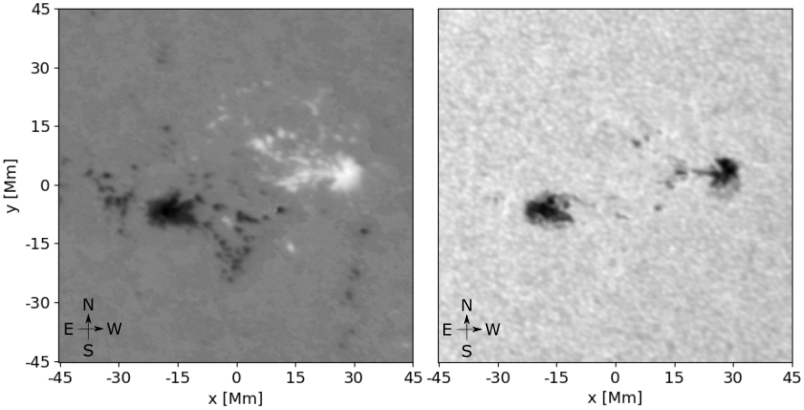
45
30
15
0
-15
-30
-45
y [Mm]
N
E
W
S
-45
-30
-15
0
15
30
45
x [Mm]
x [Mm]

Figure 1.1: SDO/HMI observation of a simple bipolar active region NOAA AR 11080. The left image shows measurements of the magnetic field's vector component perpendicular to the solar surface (2010.06.11 03:48:00, hmi.b_720s). The leading (positive) and following (negative) polarity are displayed in white and black, respectively. The right panel shows sunspots of this active region from continuum observations (2010.06.11 03:52:30, hmi.ic_45s). These images are courtesy of NASA/SDO and the HMI Science Team.

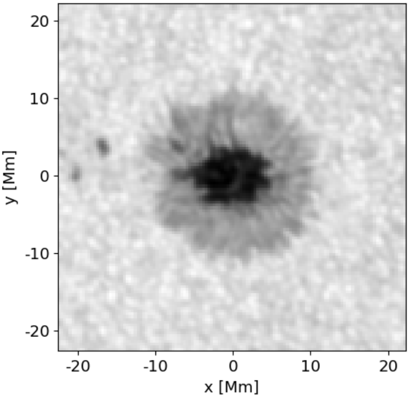
20
10
0
-10
-20
y [Mm]
-20
-10
0
10
20
x [Mm]

Figure 1.2: SDO/HMI continuum observation of NOAA AR 11072's leading sunspot (2010.05.25 03:00:00). The image is courtesy of NASA/SDO and the HMI Science Team.

active regions have been found, which are named after their discoverer: the Schwabe-cycle as well as Spörer's, Hale's and Joy's law.

Schwabe (1843) noticed through routine sunspot observations between 1826 and 1843 that the number of sunspots varies periodically. The bottom panel of Fig. 1.3 presents the average daily sunspot coverage on the visible solar disc. It shows a reoccurring pattern of high and low sunspot coverage with a periodicity of about 11 years on average, which is named the Schwabe-cycle. These observations also established the terms solar maximum and minimum, when the Sun's magnetic activity and sunspot number is at its highest or lowest, respectively.

Spörer's law was first described in Carrington (1858), who discovered that sunspots appear at different latitudes during one solar cycle. This sunspot behavior was later named after Gustav Spörer, who refined these findings (Spoerer and Maunder 1890). It states that sunspots appear at higher latitudes at the start of a solar cycle and then occur at progressively lower latitudes as the cycle goes on. The top panel of Fig. 1.3 shows this observation in a so-called butterfly diagram, due to its characteristic shape. One can see that the sunspot occurrence is predominantly limited to a band of 5° to 35° latitude north and south of the equator.

Hale's law (Hale and Nicholson 1925) states that active regions have opposite signs of their leading polarity (in direction of solar rotation) in each hemisphere during one solar cycle. These signs reverse with each solar cycle, causing a recurrence of the same magnetic pattern approximately every 22 years. This magnetic cycle is called the Hale-cycle. Fig. 1.4 shows the magnetic butterfly diagram and Hale's law.

Joy's law (Hale et al. 1919) says that the leading polarity of active regions is typically closer to the equator than the following one. Therefore, active regions bipoles are tilted relative to the east-west direction. This tilt becomes stronger with increasing solar latitude. Joy's law will be discussed in further detail in Section 1.2.

Furthermore, there are some characteristics of active regions that are well known, but have not been named. Most notably, the polarities show intrinsic asymmetries. The leading/following polarities exhibit a pro-/retrograde motion relative to the solar rotation and move towards the equator/pole, respectively (e.g. Chou and Wang 1987, Herdiwijaya et al. 1997, Schunker et al. 2019). The leading polarity has typically a more coherent structure with longer lifetimes than the dispersed following one (e.g. Zwaan 1981). On average, the location of the magnetic polarity inversion line lies closer to the leading polarity (e.g. van Driel-Gesztelyi and Petrovay 1990, Petrovay et al. 1990). Caligari et al. (1995) explains these effects by the Coriolis force acting on plasma flows within rising flux tubes, causing a retrograde motion of the apex, which moves it closer to the following polarity. A consequence of this effect is that the magnetic field in the following polarity is close to being vertical, while the leading polarity's field becomes significantly inclined (Moreno-Insertis et al. 1994). Leading and following polarities appear to be elongated during the emergence. These observational features are named "magnetic tongues" and are the result of emerging magnetic field being twisted. Due to the twist, the vertical projection of the azimuthal field component of rising flux tubes creates the impression of elongated polarities (López Fuentes et al. 2000, Luoni et al. 2011). Leka et al. (1996) were the first to show in observations that emerging magnetic field is twisted. Related to such twist, Tian and Alexander (2009) report significant difference in the helicity injection rate (see Section 1.3 for an explanation of magnetic helicity), with the leading polarity

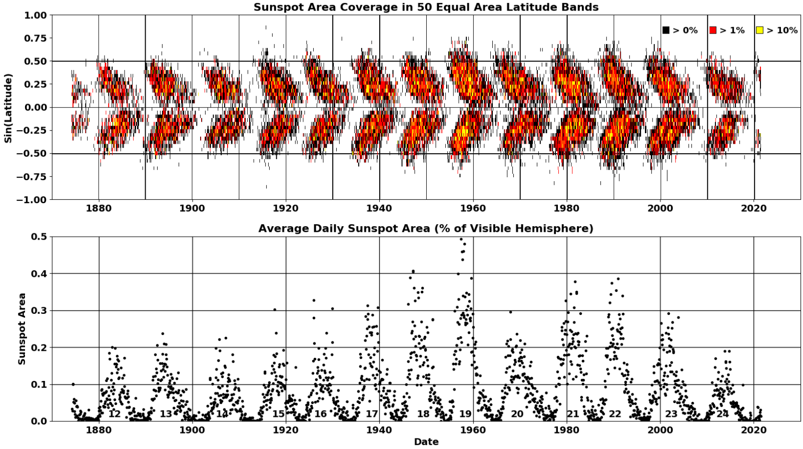

Figure 1.3: Representation of Spörer's law (top) and the Schwabe-cylce (bottom). Top: The butterfly diagram showing the latitudinal sunspot coverage versus time. Bottom: The averaged daily sunspot coverage on the visible hemisphere versus time. From http://solarcyclescience.com/solarcycle.html August 2021, with permission by Dr. David Hathaway.

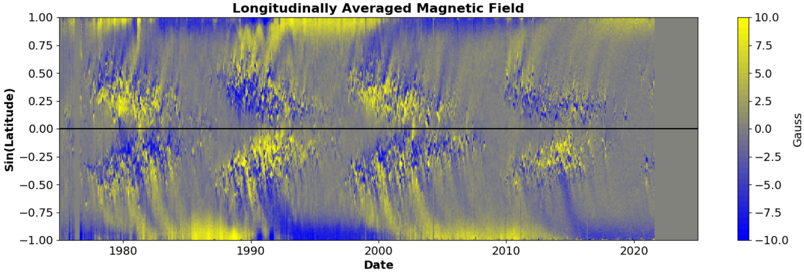

Figure 1.4: Magnetic butterfly diagram showing the longitudinally averaged radial field from 1975 to 2021 versus latitude. From http://solarcyclescience.com/solarcycle.html August 2021, with permission by Dr. David Hathaway.

injecting 3-10 times more than the following one. They attribute this effect to different emergence speeds between the leading and following legs of the rising flux tube, due to the flux tube being inclined as described by Caligari et al. (1995).

1.2 Joy's law

Joy's law is a statistical property of solar active regions. It says that the east-west aligned polarities show a systematic tilt, with the leading polarity typically being closer to the equator than the following one. This effect becomes stronger with increasing latitude.

1.2.1 Measurements of Joy's law

Joy's law is named after Alfred Harrison Joy, who studied sunspot drawings from Carrington and Spörer (1856-1893, 2633 active regions) and found the systematic tilt of active regions that is related to the latitude of their appearance. His findings were first published in Hale et al. (1919). Wolf and Brunner (1930) confirmed Joy's law later based on sunspot observations made in Zurich between 1894 and 1928.

Tang et al. (1984) used daily magnetograms from the Mount Wilson observatory that cover 15 years (1967-1981) and find that the orientation of active regions does not depend on latitude at all. Wang and Sheeley (1989) (Kitty Peak magnetograms, 1975-1986), Howard (1991) and Fisher et al. (1995) (both Mt. Wilson white-light observations, 1917-1985) confirm the latitude dependence, while Fisher et al. (1995) also finds a dependence on the total magnetic flux in the active region. They estimate the magnetic flux content of active regions from continuum images by the separation distance of the leading and following polarties, with larger separations signaling also bigger active regions and consequently higher magnetic flux content. Sivaraman et al. (1999) use sunspot data from Kodaikanal observatory (1906-1987) and Mount Wilson observatory (1917-1985) and find that the scatter from the average tilt angle at a specific latitude becomes smaller with larger active regions. Jiang et al. (2014) found a weak dependence that bigger sunspot groups have also a bigger tilt and the scatter in tilt angle goes down with increasing size of active regions.

Kosovichev and Stenflo (2008), Stenflo and Kosovichev (2012) and Tlatov et al. (2013) used magnetic field observations from space based on data from SOHO/MDI (Scherrer et al. 1995) and SDO/HMI (Scherrer et al. 2012) to investigate Joy's law. The first two confirm a dependence on latitude, but none on the magnetic flux contained within the active regions. In contrast, Tlatov et al. (2013) finds a systematic dependence on the size of bipolar regions. Small bipolar regions (less than 30 Mm in diameter, also called ephemeral regions) show tilt angles of the opposite sign compared to larger bipoles. Kosovichev and Stenflo (2008) reports that the tilt angle at emergence time appears to be random but is on average is zero. The tilt, known as Joy's law, then develops after emergence. They find that the tilt of active regions shows no dependence on their total magnetic flux. They also report no evidence for a relaxation to the east-west direction of magnetic flux tubes, after the emergence. Such a relaxation would be caused by the Coriolis force stopping to act after the magnetic field is fully emerged. Then magnetic tension forces would draw the flux tube back to an east-west direction to be aligned again with the magnetic field at the base of the convection zone, where it originally rose from and is still rooted to. Tilt angles rather relax to Joy's law in their observations, and they suggest that Joy's law is a representation of the spiral orientation of the global magnetic field (Babcock 1961, see Section 1.2.2).

McClintock and Norton (2013) reevaluated the Mount Wilson sunspot data set (1917-1985) and suggests that the tilt has only a weak dependence on latitude, and the tilt in theoretical models should not be forced to zero at the equator. They state that active region tilt varies with solar cycle and hemisphere. This finding is in agreement with Sivaraman et al. (1999) and Dasi-Espuig et al. (2010), who analyzed white-light images from the Mount Wilson and Kodaikanal observatories. Based on their results, McClintock and Norton (2013) suggest that Joy's law is caused by a combination of the Coriolis force and the global spiral-like field structure as described in Babcock (1961)'s dynamo model.

McClintock and Norton (2016) used continuum observations of sunspots from SDO HMI and analyze the tilt angle evolution relative to the time, when the umbral area is biggest. They report a clear dependence of the tilt on the umbral area. Active regions with large umbral areas, that cover approximately 110 MSH[1], show a steadily increase in their tilt angle during the observations. Regions with mid-sized umbras ($\approx$ 50 MSH) remain constant tilt, while small regions (umbra with $\approx$ 30 MSH) have random or even negative tilt angles before the umbral area peaks. Notably, the tilt angle of large active regions is close to zero during emergence.

This Section shows that studies of Joy's law provided often contradicting results, and we still only have a rough understanding of what causes the active region tilt. A huge fraction of observations so far was based on sunspots. As Section 1.1.3 describes, sunspots only form after sufficient magnetic flux has emerged at the solar surface. Therefore, sunspot observations miss the early phases of magnetic field emergence, which are important in identifying the mechanisms that lead to Joy's law. Another issue of sunspot observations is that one cannot distinguish positive and negative polarities. Consequently, it is easy to misjudge the magnetic field's tilt, when multiple flux emergences occur in close vicinity and the field's polarities can't be identified. Additionally, there is no way to tell active regions apart that obey or don't obey Hale's polarity law. Therefore, observations of the magnetic field in high spatial and temporal resolution, especially during the emergence phase, are crucial to get a better understanding of Joy's law.

1.2.2 Origin of Joy's law

The origin of Joy's law is tightly linked to theories of the solar dynamo and magnetic flux emergence, and is still under debate.

The first attempt to explain Joy's law was made by Babcock (1961). The Sun's magnetic field is described with two magnetic field components in his dynamo model: a poloidal field with radial and tangential field components (north-south aligned) and a toroidal field, which has no radial component (east-west aligned). During a solar cycle the poloidal field is converted to a toroidal field, due to the differential rotation of the Sun (Ω-effect). This creates a spiral-like structure of the magnetic field wrapping around the Sun. Babcock (1961) suggests that Joy's law is a reflection of this global field structure. Observations suggest that the active region tilt is close to zero at the equator and becomes progressively stronger with increasing solar latitude. However, the wound up magnetic field's tilt is higher at lower latitudes compared to higher latitudes in Babcock (1961)'s model. Therefore, it is doubtful that this theory explains Joy's law.

---

[1] Millionths of Solar Hemisphere

The Coriolis force is another factor, that was suggested to be responsible for creating active region tilt. The Coriolis force deflects the path of moving objects in a rotating system to conserve angular momentum. In terms of force per volume unit it is described by $2\rho(\mathbf{v} \times \boldsymbol{\omega})$, where ρ is the mass density, $\mathbf{v}$ the velocity of the moving object and $\boldsymbol{\omega}$ the angular velocity of the rotating reference frame. On the Sun, the Coriolis force acts on plasma flows within or around flux tubes, which drag the magnetic field with them, due to high plasma beta in the solar interior and the photosphere. When the Coriolis force acts on plasma flows within a rising flux tube, it is assumed that the amount of tilt created is proportional to the amount of magnetic flux within the tube. A flux tube with more magnetic flux is less susceptible to drag and has stronger downward directed plasma flows, which consequently creates a stronger tilt that could be observed as Joy's law (Fan et al. 1994). The amount of tilt caused by the Coriolis force should also vary with solar latitude. The ascent and expansion of a flux tube drives plasma flows from the apex to the foot points of the loop. It can be shown that in a simple theoretical model the strength of the induced tilt by the Coriolis force on a flux tube is proportional to $\sin\theta$, where θ is the solar latitude (e.g. D'Silva and Choudhuri 1993).

Babcock (1961) also gives a possible explanation for Joy's law based on the Coriolis force. He suggests that the Coriolis force acts on the convective flows surrounding the active region as the origin of the tilt. On the other hand, Wang and Sheeley (1991) suggest that the Coriolis force acting on plasma flows within a flux tube is responsible for Joy's law, while it rises through the convection zone. The last idea works well in simulations (e.g., D'Silva and Choudhuri 1993, Fan 2009, Weber et al. 2011). Schmidt (1968) proposes that flux-tubes emerge in upwelling, east-west aligned supergranular cells and the surface flows drives the polarities apart.

Leighton (1969) proposes that the kink instability may cause the tilt. A deformation, i.e. kinking, in a highly twisted flux tube will cause a magnetic pressure imbalance, which is known as kink instability. On the inside of the kink, the azimuthal field lines are moving closer together, causing the magnetic pressure to rise, while the opposite happens on the outside of the kink. This pressure gradient causes a force in the same direction as the kinking occurs. If not stabilized by other forces (e.g. the gas pressure gradient) the instability continues to grow. The twist of the flux tube is consequently converted into a deformation of the flux tube axis to conserve magnetic helicity that can eventually be observed as Joy's law.

1.3 Magnetic helicity

One parameter that can give further insights into Joy's law and constrain theories of the magnetic field's evolution in the solar interior, is the twist of the magnetic field. The twist of the magnetic field can be characterized through magnetic helicity.

1.3.1 Definition of magnetic helicity

The Gauss linking number describes the topological structure of interlinked closed curves. Magnetic helicity is a generalization of the Gauss linking number for magnetic fields $\mathbf{B}$ (Pevtsov et al. 2014) and measures how twisted, sheared, linked and braided magnetic field lines contained in a volume V are (Berger and Field 1984). Magnetic helicity H is described as

$$H = \int_V \mathbf{A} \cdot \mathbf{B}\, dV, \tag{1.2}$$

where $\mathbf{A}$ is the vector potential ($\mathbf{B} = \nabla \times \mathbf{A}$).

Magnetic helicity is a conserved quantity under two conditions (Webb 2018). First, the magnetic field has to be located in an environment with infinite conductivity. The conditions on the Sun allow for almost perfect conservation of magnetic helicity, due to high magnetic Reynolds numbers from the Sun's interior to the corona (10^6 – $10^{15,}$ Hood and Hughes 2011, Pevtsov et al. 2014), which measures the ratio of induction over diffusion. Berger (1984) state that even resistive events (e.g. magnetic reconnection, which describes a breaking and restructuring of magnetic field lines) have little influence on the conservation of magnetic helicity. Second, the whole magnetic field structure has to be fully confined in a volume V with a boundary surface S so that $\mathbf{B} \cdot \mathbf{n}|_S = 0$, where $\mathbf{n}$ is a vector normal to the surface. In this case Eq. 1.2 is gauge-invariant, i.e. H does not depend on the transformation used to derive $\mathbf{A}$ (Priest 2014).

If magnetic field lines enter or leave the volume in which magnetic helicity is calculated, Eq. 1.2 is no longer gauge-invariant. Berger and Field (1984) show that when the helicity of two field structures (which only differ in a small volume V) is calculated in an infinite volume, the difference in helicity depends solely on the small volume, where the field is different. Therefore, they propose the relative magnetic helicity H_r, which is again gauge-invariant:

$$H_r = \int_V (\mathbf{A} + \mathbf{A_P}) \cdot (\mathbf{B} - \mathbf{B_P})\, dV. \tag{1.3}$$

$\mathbf{A_P}$ and $\mathbf{B_P}$ refer to a reference potential field ($\nabla \times \mathbf{B_P} = 0$), which is fully determined by $\mathbf{B_P} \cdot \mathbf{n}|_S = \mathbf{B} \cdot \mathbf{n}|_S$. The relative helicity is typically used in solar physics because the photosphere provides a natural bounding surface for magnetic field observations, and magnetic vector field measurements below the Sun's surface are not available.

1.3.2 Self-helicity: twist and writhe

The magnetic field in active regions and in particular in individual sunspots is often modelled with flux tubes, which are coherent bundles of magnetic field. The magnetic helicity of multiple interlinked flux tubes can be decomposed into mutual helicity and self-helicity. While mutual helicity measures the linkage and braiding of individual flux tubes, self-helicity is a measure for the internal structure of a single flux tube and has two components: writhe W and twist T (Moffatt and Ricca 1992). Writhe measures the deformation of the flux tube's axis, while twist measures how often a set of field lines turns around the tube's axis. In a uniformly twisted flux tube, the twist can be described with

$$T = qL, \tag{1.4}$$

with L being the length of the flux tube and the twist density q describing how often the magnetic field turns around the tube's axis per length unit.

Self- and mutual helicity can be exchanged during reconnection processes, while the total helicity of the field structure stays approximately conserved (Wright and Berger

1989). Without any external influence, the self-helicity of a single flux tube $H = T + W$ is conserved.

When measuring helicity directly from photospheric observations, simplifications must be made to get estimates for the twist and writhe of the magnetic field. It is assumed that the magnetic field in sunspots can be described as a vertical uniformly twisted flux tube. Therefore, twist measurements estimate the twist density of such a flux tube either based on the force-free parameter α (e.g. Longcope et al. 1998, Hagino and Sakurai 2004, Leka et al. 2005) or a least-squares fitting approach of the twist density relative to a reference model of the flux tube (e.g. Nandy et al. 2008, Crouch 2012). The writhe is qualitatively often put on equal terms with the tilt of active regions (e.g. Canfield and Pevtsov 1998, Tian et al. 2001). This assumption is based on the idea that the magnetic field in simple bipolar active regions is rooted to the global toroidal magnetic field and any deviations of the magnetic field's orientation from this east-west direction is interpreted as writhe.

1.3.3 Hemispheric helicity sign rule

The hemispheric helicity sign rule (HHSR) is an observed statistical tendency of the solar magnetic field's helicity to be preferentially negative (left-handed chirality)/positive (right-handed chirality) in the northern/southern hemisphere, respectively. It is an important characteristic of the magnetic field that solar dynamo models should be able to recreate (Charbonneau 2020). First suggestions for the HHSR came from Hale (1927), who observed "hydrogen whirls" in sunspots, which have a preferential chirality in the northern and southern hemisphere, which does not change with solar cycle. The majority of reports about the HHSR is now based on observations of the magnetic field of active regions (e.g. Seehafer 1990, Pevtsov et al. 1995, Longcope et al. 1998, Pevtsov et al. 2001, Hagino and Sakurai 2005, Zhang 2006, Tiwari et al. 2009a), but also other sources were used, e.g. X-ray sigmoids (Rust and Kumar 1996), filament channels (Martin et al. 1994) or the quiet Sun network (Pevtsov et al. 2001).

Pevtsov et al. (2008) studies the HHSR in 19 years of vector magnetograms that cover 3 solar cycles (21-23) and state that the HHSR is independent of the solar cycle. Various other studies (e.g. Zhang and Bao 1998, Hagino and Sakurai 2005, Hao and Zhang 2011) suggest that the HHSR depends on the phase within a solar cycle, i.e. that the HHSR is present during phases of solar maximum but cannot be found during a solar minimum. Zhang et al. (2010) and Choudhuri et al. (2004) confirms the HHSR but also reports short periods during the transition of solar cycles, when the HHSR reverses.

Manek and Brummell (2021) propose an explanation why the HHSR is usually measured as a weak statistical tendency and why its strength varies during a solar cycle. They simulated the rise of initially twisted flux tubes in the background poloidal field of the Sun. They found that if the azimuthal field at the bottom of the flux tube is aligned with the background magnetic field an upwards directed tension force is created that additionally aids buoyancy. In contrast, when the background field is aligned with the azimuthal field at the top of the flux tube, a downwards directed tension force hinders the rise. Manek et al. (2020) describe that a background field strength of about 6-16% of the axial field strength of the flux tube is enough to suppress the ascent. Manek and Brummell (2021) found in Monte-Carlo simulations that 76% of flux tubes with random initial twist and orientation were able to rise, similar to previous observational studies of the HHSR. If the initial field strengths are above this threshold, a twisted flux tube can still rise through an unfavorably aligned background field, which explains the observed scatter in the HHSR. This model also predicts that the HHSR becomes more (less) pronounced during the rise (fall) to solar maximum (minimum). This is because at the beginning of a solar cycle (at solar minimum) the poloidal field in the convection zone has still dominantly the orientation of the previous cycle. The new solar cycle's poloidal field orientation becomes more prevalent and stronger in the convection zone towards solar maximum. Consequently, less flux tubes with twist opposing the HHSR are able to rise.

1.3.4 Origin of twist in flux tubes

Theories have so far assumed that flux tubes rising through the convection zone have to be twisted due to a strong tendency for fragmentation otherwise (Schuessler 1979, Longcope et al. 1996, Moreno-Insertis and Emonet 1996, Fan et al. 1998a, Abbett et al. 2000, Fan 2001). Knizhnik et al. (2021) recently show in simulations that also untwisted magnetic flux can reach the photosphere. Various different mechanism can impose twist on a flux tube.

The α-effect is a key mechanism in mean field dynamo theory, that imposes twist on the magnetic field. The idea of the α-effect is that statistically homogeneous fluctuations of a velocity field (i.e. plasma motions) and the magnetic field create an electromotive force along the mean magnetic field. This electromotive force generates magnetic helicity of opposite signs in the mean field and the fluctuations (e.g. Moffatt 1978, Seehafer 1996). The necessary plasma motions can arise by themselves from instabilities of the magnetic field (Brandenburg and Schmitt 1998). Ferriz-Mas et al. (1994) studied magnetic buoyancy instabilities in this regime. They find that weak, slowly growing instabilities are affected by the Coriolis force and develop as helical waves along the flux tube and impart twist on it. Such an α-effect would eventually cause twist in flux tubes opposite to the HHSR. Another important aspect is that the α-effect weakens when the magnetic field exceeds the magnetic equipartition field strength, i.e. the magnetic energy density exceeds the kinetic energy density of the plasma motions. This effect is called α-quenching. This is because the magnetic field will at a certain field strength resist the influence of small scale/weak plasma motions (Brandenburg et al. 2008). Due to the wrong imposed sign of twist and the α-quenching, the α-effect plays a subordinate role in theories trying to explain the observed twist distribution in the photosphere.

Longcope et al. (1998) introduced the Σ-effect: A magnetic flux tube would gain its twist through interaction with its surrounding turbulent velocities during the ascent through the convection zone. This is the main difference to the α-effect, where helical turbulent velocities act within the magnetic field structure. The surrounding plasma motions, which have a non-vanishing kinetic helicity, cause small-scale deformations of the tube's axis and impose writhe. Because of helicity conservation, this writhe will then be compensated through twist. Longcope et al. (1998) show that the Σ-effect creates twist as expected by the HHSR and is not limited like the α-effect is by α-quenching.

The Coriolis force acts on plasma flows within a rising flux tube, which tilts the flux tube away from the toroidal east-west direction, as described in Section 1.2.2. This tilting can be interpreted as an addition of writhe (i.e. a deformation of the flux tube axis) when assumed that the flux tube is still rooted to the toroidal field. Then the flux tube becomes twisted to compensate for the writhe and to conserve magnetic helicity. The sign of this twist is in agreement with the HHSR, but is thought to be too small in comparison to the twist observed in active regions (Choudhuri and Gilman 1987, Longcope and Klapper 1997, Fan and Gong 2000, Wang 2013).

Another source that adds helicity to the solar magnetic field is differential rotation (DeVore 2000). In simple bipolar active regions, the surface differential rotation causes the magnetic polarities to rotate and move with different speeds relative to each other due to active region tilt. This adds twist and writhe to the magnetic field. Démoulin et al. (2002) show that surface differential rotation is an ineffective way to inject twist into the solar magnetic field. Similarly, Green et al. (2002) studied the helicity budged of an active region that caused coronal mass ejections (CME) and find that surface differential rotation cannot account for the huge amount of helicity loss after a CME. Longcope et al. (1999) state that differential rotations acts too slowly to affect individual flux tubes. Berger and Ruzmaikin (2000) studied the helicity generation in the solar interior over 22 years of observations (1976-1998) and suggest that differential rotation in the convection zone can contribute to the total magnetic helicity observed in the solar atmosphere.

Another possibility is that twist is built up through the accretion of the background poloidal field during the ascent of a flux tube through the convection zone. A flux tube that rises from the toroidal field cannot simply cut through the poloidal field due to the high magnetic Reynolds numbers in the convection zone. It pushes the poloidal field, which reconnects in the ascending flux tube's wake. The poloidal field, which now wraps around the rising flux tube, imparts twist on the flux tube in accordance to the HHSR (Choudhuri 2003, Chatterjee et al. 2006). This effect can explain, why some studies (e.g. Zhang et al. 2010, Choudhuri et al. 2004) report brief periods during the transition from one solar cycle to the next, in which the HHSR is reversed. During this time the poloidal field in the solar convection zone is still dominated by the one generated during the preceding cylce. The newly generated toroidal flux tube emerge into this "old" magnetic field, which consequently imparts twist on the rising flux tube opposite to what is expected from the HHSR. Around solar maximum the poloidal field changes sign (compare Fig. 1.4), which eventually leads again to twist in accordance to the HHSR.

1.3.5 Twist estimation methods

This Section provides an overview of methods to estimate the magnetic field's twist. This thesis uses methods that estimate the twist directly from a single vector magnetic field observation without the need of any extrapolations. They are based either on the force-free parameter α or a fit of the magnetic field's winding rate q.

Observations of the solar magnetic field are routinely done in the photosphere, although measurements in the chromosphere or corona exist as well (e.g. Lin et al. 2004). They provide vector magnetic field data at a single layer from a specific optical depth. Calculations of magnetic helicity require information about the magnetic field in 3D space (see Eq. 1.2 and 1.3). Due to the lack of observational information, various methods have been developed to estimate proxies for the solar magnetic field's helicity content from 2D observations.

One set of methods is based on the force-free equation $\nabla \times \mathbf{B} = \mathbf{J} = \alpha \mathbf{B}$. Ampere's law describes that a twisted magnetic field **B** produces a current with density **J**. Force-free magnetic fields occur when the plasma pressure is small in comparison to the magnetic pressure, i.e. areas with a small plasma-β. This results in vanishing Lorentz forces, hence the name "force-free", and currents are co-aligned with the magnetic field ($\mathbf{J} = \alpha\mathbf{B}$) and proportional to the force-free parameter α. Therefore, α can be seen as a relative measure for how twisted the magnetic field is and is used as a proxy for the magnetic field's helicity content (Pevtsov et al. 2014).

Woltjer (1958) gives a more sophisticated description how magnetic helicity and the force-free parameter α are connected. They demonstrate that a magnetic field structure with a certain magnetic helicity content corresponds to a linear force-free field in its lowest attainable energy state.

In force-free magnetic field extrapolations, α is constant along an individual field line. If α is constant for all field lines within the model, the model is called linear. In contrast, nonlinear models allow α to change from one field line to the other.

The α value of the best fitting linear force-free magnetic field extrapolation is one possibility to characterize the helicity content of active regions (e.g. Pevtsov et al. 1995, α_{Best}). If one wants to avoid field extrapolations, the so-called "vertical component" of the force-free parameter $\alpha_z = (\frac{\partial B_y}{\partial x} - \frac{\partial B_x}{\partial y})/B_z$ can be used. Burnette et al. (2004) measured spatial averages over 34 active regions. They find that these averages are well correlated with α_{Best} of the respective regions. This suggests that a two-dimensional spatial average can be used to characterize the helicity content of an active region, which should be calculated in three-dimensional space.

Longcope et al. (1998) uses spatial averages of α_z over whole active regions to characterize their helicity content. Hagino and Sakurai (2004) suggest to use weighted averages of α_z either by the squared or absolute vertical field component B_z. This is done to avoid the influence of weak field, where vector magnetic field measurements are less accurate.

Leka et al. (2005) study the twist in single flux tubes. They show that a spatial average of α_z underestimates the tube's twist content (also see Leamon et al. 2003, Valori et al. 2005). They find that only a single value of α_z (α_{Peak}) at a uniformly twisted flux tube's axis, where the α_z profile peaks, can be directly related to the tube's twist density q ($\alpha_{\mathrm{Peak}} = 2q$).

Another approach to estimate the helicity content in individual sunspots directly from photospheric observations is done by least-squares fitting methods of the twist density. These have the advantage of not relying on the force-free assumption, which is thought to be violated in the photosphere (e.g. Gary 2001). It must be mentioned in this context that Duan et al. (2020) recently measured Lorentz forces in the photosphere. They claimed that the photosphere is closer to a force-free state than so far assumed.

Nandy et al. (2008) least-squares fitting approach assumes that a sunspot's magnetic field can be approximated by a monolithic vertical flux tube with a constant winding rate q so that the tube's azimuthal field $B_\theta = qrB_z$, where B_z is the vertical field strength and r is the distance from the flux tube's axis. For this approach, the spot's center is estimated by calculting the flux weighted center of $|B_z|$. The ratio B_θ over B_r can then be plotted as a function of the distance from the spot's estimated center, and the resulting slope q corresponds to the spot's twist density.

The following methods are not used in this thesis, but are briefly mentioned for the sake of completeness. Démoulin and Berger (2003) state that with a time series of magnetic field observations, measurements of the magnetic field and surface velocities can be used to estimate helicity fluxes through the photopshere. This helicity flux can be decomposed into a braiding (writhe) and spinning (twist) term (Longcope et al. 2007). The reliability of these helicity flux estimates is debated, as Welsch et al. (2007) shows in MHD simulations that derived helicity fluxes are not always valid.

Longcope and Malanushenko (2008) show that the twist can also be found from generalizations of the relative helicity (Eq. 1.3) for a subvolume of the whole magnetic field, i.e. a flux tube. They define a so-called additive self-helicity, which can be related to the twist, and the unconfined self-helicity, which behaves like the sum of twist and writhe, i.e. the total self-helicity content.

1.3.6 The connection between the tilt and twist of active regions

When simple bipolar regions are modelled with a uniformly twisted flux tube, the total helicity content within the flux tube can be described as the sum of its writhe and twist ($H = T + W$, see Section 1.3.2). Due to the conservation of magnetic helicity, any change of twist or writhe will be compensated with the same amount but opposite sign of the other quantity. If a flux tube is initially straight and untwisted ($H = 0$) and twist or writhe would be imposed, one would expect: $\mathrm{sign}(T) = -\mathrm{sign}(W)$. This would be the case if e.g. the Coriolis force imparts twist on the flux tube. If kink instability is triggered in an already highly twisted flux tube, twist is converted to writhe. In such a case, the twist and writhe are expected to have the same sign: $\mathrm{sign}(T) = \mathrm{sign}(W)$.

Pevtsov and Canfield (1998) find a positive correlation of active region tilt and the twist proxy α, in active regions that strongly depart from Joy's law. They suggest that in these cases the kink instability plays an important role in creating the observed tilt. Tian et al. (2001) and Tian and Liu (2003) report a negative correlation, therefore favoring the Coriolis force as the primary contributor for the observed active region tilt. Studies by López Fuentes et al. (2003) revealed rather inconclusive results. They found a similar amount of active regions, where the twist/tilt relation could be attributed to either the kink instability or the Coriolis force. Holder et al. (2004) conducted one of the biggest studies of tilt and twist in 356 active regions. They find no correlation of twist and tilt for active regions that follow Joy's law. Active regions that strongly deviate from Joy's law show a positive correlation of twist and tilt, signaling a relation to kink instabilities in their creation. They also support the Σ-effect for creating twist in rising flux tubes, since they find no relation between the scatter of tilt angles and the twist, which is in agreement with the theory by Longcope et al. (1998).

Judging from these results it is not clear, which theory describes the connection between the twist and tilt of active regions. It is likely that in individual cases different mechanism play a more dominant role than others.

1.4 SDO/HMI

This Section presents an overview of the Helioseismic and Magnetic Imager (HMI, Scherrer et al. 2012) on board of the Solar Dynamic Observatory (SDO, Pesnell et al. 2012), which gathered the data used in this thesis.

The SDO satellite was launched on February 11th 2010 to a geosynchronous orbit above its ground station in New Mexico (USA). It was the first mission in NASA's "Living with a star" program, which has a main focus on space weather research. SDO is equipped with instruments to investigate the generation and structure of the solar magnetic field, the storage and release of magnetic energy, the observation of energetic particles as well as the solar irradiance. The instrument for this purpose are the Atmospheric Imaging Assembly (AIA), Extreme Ultraviolet Variability Experiment (EVE) and the Helioseismic and Magnetic Imager (HMI).

This thesis uses data from HMI. The instrument is designed to measure solar oscillation and the magnetic field in full-disk observations. HMI is equipped with 2 high-resolution cameras (4096×4096 pixels) and observes the Sun with a pixel scale of 0.5 arcseconds. The so-called Doppler camera focuses on measuring the continuum intensity and the Fe I line (6173 Å), which is used to infer Dopplergrams and the line-of-sight magnetic field. The Vector camera observes in parallel the linear and circular polarisation of the incoming light. The observed Stokes profile, which contains information about the intensity and polarisation of the observed light, is then processed by using the "Very Fast Inversion of the Stokes vector" (Borrero et al. 2011) algorithm to determine the vector magnetic field.

Various data products based on these observations are publicly available. In chapter 2 we use observations of the line-of-sight magnetic field (hmi.m_45s), which are provided with a cadence of 45 seconds. Data used in chapter 3 and 4 originate from the vector magnetic field observations (hmi.b_720s) which have a cadence of 12 minutes. Continuum observations, which are taken every 45 seconds, are from the hmi.ic_45s series.

1.5 Motivation of the thesis

The first paper in this thesis presents a systematic study of Joy's law during the emergence of active regions observed in HMI line-of-sight magnetograms. Observation of Joy's law are traditionally based on continuum intensity images of sunspots and, therefore, already well established active regions. As a result a common property of theories about the origin of Joy's law is that the tilt develops while the magnetic field rises through the convection zone and is visible as soon as the field reaches the surface. Continuum observations of sunspot do not capture early phases of magnetic field emergence because sunspots only appear in continuum images, when the magnetic flux concentration is sufficiently high enough. Since Joy's law is a statistical property of active regions, a big data set is needed to capture systematic properties of magnetic flux emergence and few studies have been made that try to capture Joy's law during the emergence process (e.g. Kosovichev and Stenflo 2008, McClintock and Norton 2016, see Section 1.2.1 for details) with varying results. Kosovichev and Stenflo (2008) surprisingly found using SOHO/MDI data that on average active regions emerge without tilt, contradicting the paradigm that the magnetic field should already be tilted when it emerges.

We use the HEAR survey (Schunker et al. 2016) to measure the tilt angle of 182 active regions during their emergence process. The HEAR survey tracks emerging active regions in SDO/HMI observations (pixel scale of 0.5 arcsec and 45 second cadence), which provide higher spatial and temporal resolution than the data set Kosovichev and

Stenflo (2008) used from SOHO/MDI (pixel scale of 2 arcsec and 96 minute cadence). This gives us a more detailed picture on the evolution of Joy's law during the emergence of active regions.

Measurements of the twist in the photospheric magnetic field can constrain models of flux emergence, which try explain the origin of Joy's law. The twist distribution at the solar surface is also a constraining factor for solar dynamo models in general. Therefore, we look into measurement methods to infer the magnetic field's twist directly from photospheric observations in the second part of this thesis. It is crucial to understand how reliable these twist measurements are. The twist of sunspots or even whole active regions is often characterized with a single parameter, i.e. suggesting a uniform twist. But observations typically reveal complex twist patterns (Pevtsov et al. 1994, Socas-Navarro 2005, Su et al. 2009). The nature of these pattern is not clear. There might be an underlying uniformly twisted field structure in accordance to the HHSR, but due to the forced environment in the photosphere, this structure can be distorted. Open questions are, whether temporal fluctuations of a uniformly twisted magnetic field can create the complex twist pattern seen in observations and how robust twist measurements are under such fluctuations.

We plan to test various twist calculation methods with a uniformly twisted semi-empirical sunspot model that includes spatially correlated fluctuations of the magnetic field based on in SDO/HMI observations. These test shall help with the interpretation of twist measurements. We also apply these methods to the observations in the HEAR survey to characterize the magnetic field's twist in emerging active regions based on the tested methods.

1.6 Structure of the thesis

In chapter 2, we study the evolution of tilt angles in 182 active regions using the HEAR survey (Schunker et al. 2016) in order to find systematic behavior of Joy's law during their emergence. In chapter 3, we test the robustness of the force-free parameter α and a least-squares fitting method proposed by Nandy et al. (2008) as proxies for the magnetic field twist in a fluctuating magnetic field. In chapter 4, we extend the results with twist measurements from emerging active regions and conclude the thesis in chapter 5 with a discussion and outlook for future research opportunities.

2 Average motion of emerging solar active region polarities: Joy’s law

2.1 Abstract

The tilt of solar active regions described by Joy’s law is essential for converting a toroidal field to a poloidal field in Babcock-Leighton dynamo models. In thin flux tube models the Coriolis force causes what we observe as Joy’s law, acting on east-west flows as they rise towards the surface.

Our goal is to measure the evolution of the average tilt angle of hundreds of active regions as they emerge, so that we can constrain the origins of Joy’s law.

We measured the tilt angle of the primary bipoles in 153 emerging active regions (EARs) in the Solar Dynamics Observatory Helioseismic Emerging Active Region (SDO/HEAR) survey. We used line-of-sight magnetic field measurements averaged over 6 hours to define the polarities and measure the tilt angle up to four days after emergence.

We find that at the time of emergence the polarities are on average aligned east-west, and that neither the separation nor the tilt depends on latitude. We do find, however, that EARs at higher latitudes have a faster north-south separation speed than those closer to the equator at the emergence time. After emergence, the tilt angle increases and Joy’s law is evident about two days later. The scatter in the tilt angle is independent of flux until about one day after emergence, when we find that higher-flux regions have a smaller scatter in tilt angle than lower-flux regions.

Our finding that active regions emerge with an east-west alignment is consistent with earlier observations, but is still surprising since thin flux tube models predict that tilt angles of rising flux tubes are generated below the surface. Previously reported tilt angle relaxation of deeply anchored flux tubes can be largely explained by the change in east-west separation. We conclude that Joy’s law is caused by an inherent north-south separation speed present when the flux first reaches the surface, and that the scatter in the tilt angle is consistent with buffeting of the polarities by supergranulation.[1]

---

[1] This chapter reproduces the article *Average motion of merging solar active region polarities: Joy’s law* by H. Schunker, C. Baumgartner, A. C. Birch, R. H. Cameron, D. C. Braun and L. Gizon, published in Astronomy and Astrophysics, 640, A116 (2020). C. Baumgartner tested the reproducibility of the results and high-resolution tests, specifically Appendix A and Appendix B. He contributed to writing the manuscript.

2.2 Introduction

There are two well-known constraints for dynamo models from early studies of flux emergence: Hale's law, which tells us that the magnetic bipoles of larger active regions that emerge in the northern and southern hemispheres have opposite polarities, and Joy's law, which describes the observed statistical tendency of the leading polarity of an active region to be closer to the equator than the following polarity (Hale et al. 1919). This tilt angle between the leading and following polarities tends to increase with unsigned latitude (e.g. Driel-Gesztelyi and Green 2015, and references therein), and plays an essential role in the Babcock-Leighton dynamo model (Babcock 1961, Cameron and Schüssler 2015, Karak and Miesch 2017).

Given the increase in tilt angle with latitude, the physical cause of Joy's law is believed to lie in the Coriolis force. This immediately raises the question: Upon what motions does the Coriolis force act?

One possibility is the motion associated with the buoyant rise of the magnetic flux tube through the solar convection zone (e.g. Wang and Sheeley 1991, D'Silva and Choudhuri 1993, Fisher et al. 1995, Weber et al. 2011). An alternative possibility is the motion of the turbulent convection (e.g. Parker 1955, Choudhuri and D'Silva 1990, Brandenburg 2005), with Schmidt (1968) having suggested that active region bipoles emerge in upwelling supergranular cells with an east-west orientation, and that the surface flows in the cell move the polarities outwards, away from one another.

Apart from the question of the motions involved in producing Joy's law, there is the question of what causes the large observed scatter in the tilt angle (Joy's law is a statistical tendency with large variations between individual active regions). This scatter has been found to be smaller for active regions with a higher flux (e.g. Jiang et al. 2014). This could be due to the surface polarities with lower flux being more susceptible to buffeting by the convection (e.g. Fan et al. 1994, Longcope et al. 1996, Weber et al. 2011), or, as suggested in Schunker et al. (2019), the measurement of the position of larger polarities (with higher flux) has less scatter because the centre of gravity is not as affected by the buffeting by convection.

Traditionally, Joy's law has been measured from continuum intensity images of sunspots (e.g. McClintock and Norton 2016). The measured tilt angles are therefore of mostly well-established, stable active regions. To understand the origin of active region tilt angles it is therefore necessary to use magnetic field observations to capture the very beginnings of the emergence process, and to follow the evolution as a function of active region lifetime.

Observations from monitoring instruments such as the Michelson Doppler Imager on board the Solar and Heliospheric Observatory (SOHO/MDI; Scherrer et al. 1995) and the Helioseismic and Magnetic Imager on board the Solar Dynamics Observatory (SDO/HMI; Scherrer et al. 2012) make it possible to capture the emergence process of active regions both in intensity and magnetic field observations (e.g. Kosovichev and Stenflo 2008, McClintock and Norton 2016).

Kosovichev and Stenflo (2008) studied more than 700 bipolar active regions using SOHO/MDI 96-minute cadence magnetic field observations, and found that the tilt angle of active regions at the time of emergence was statistically zero, and that the tilt angle is established during the emergence process (which lasts about 1-1.5 days). In one case study using heliosesimology to measure subsurface flows, González Hernández et al. (2013) showed that the direction of subsurface vortical flows below an anti-Joy's law active region (AR11073) is consistent with driving the leading polarity away from the equator. The advantage of using SDO/HMI is that it has observed hundreds of relatively simple active region emergence processes.

In this paper we present the statistical evolution of the tilt angle of 153 emerging active region (EAR) polarities from the Solar Dynamics Observatory Helioseismic Emerging Active Region (SDO/HEAR) survey (Schunker et al. 2016, 2019) in an effort to understand the origins of Joy's law. Using the SDO/HEAR survey, Schunker et al. (2019) identified two distinct phases of emergence. In phase 1 the speed of the separation between the polarities increases starting when the bipole first appears at the surface, and lasts until about 0.5 days after the time of emergence. Phase 2 then begins when the speed of the separation starts to decrease and lasts until about two days after the emergence time when the polarities stop separating. We follow the evolution of the tilt angle in relation to these phases, and as a function of latitude to characterise Joy's law. Birch et al. (2016) found by averaging over the emerging active regions in the SDO/HEAR survey that there are no significant outflows during emergence, although these surface outflows are predicted by thin flux tube theory. Birch et al. (2019) did, however, find an average east-west elongated prograde flow just prior to emergence.

We now turn our attention to the evolution of the tilt angle and Joy's law. First, in Sect. 2.3, we briefly describe how we measure the tilt angle of polarity pairs in emerging active regions from measurements in the SDO/HEAR survey. We then show the evolution of the tilt angle and the scatter in the tilt angle as a function of time and flux in Sects. 2.4 and 2.5. In Sect. 2.6 we show the north-south separation, east-west separation, and tilt angle as a function of latitude at the time of emergence and two days later. We discuss the change in tilt angle with latitude in relation to what we would expect from the Coriolis effect in Sect. 2.7. In Sect. 2.8 we explain how the apparent tilt angle relaxation can be largely reproduced by the change in east-west separation. We summarise our results in Sect. 2.9 and discuss the models we think are useful to describe Joy's law.

2.3 Measuring the tilt angle of the polarities

We computed the tilt angle of the polarities in 153 active regions from measurements of the location of the polarities as described in Schunker et al. (2019). The algorithm used in this paper was slightly modified from the previous measurements. We summarise the relevant details below.

The SDO/HEAR survey (Schunker et al. 2016) consists of 182 emerging active regions observed by SDO/HMI between May 2010 and July 2014. The 716 × 716 Mm (512 × 512 pixel) Postel-projected maps of the SDO/HMI line-of-sight magnetic field are centred on the active region and tracked at the Carrington rotation rate up to seven days before and after the emergence. We are interested in the evolution of the active regions on timescales of a fraction of a day. For helioseismology purposes the data is divided into 6.825-hour datacubes, and are labelled with a time interval (`TI`) relative to the emergence time (`TI+00`). We retained these time intervals for consistency and convenience and averaged the line-of-sight magnetogram maps over this time interval. Table B.1 in

Schunker et al. (2019) lists the mid-time of the averaged `TI` to the time of emergence, $\tau = 0$, for each time interval label. They measured the position of the polarities in each of these averaged line-of-sight magnetic field maps using a feature recognition algorithm designed to determine the centroid position of the primary opposite polarities. The averaged line-of-sight magnetogram map was first shifted so that the centre of the map coincides with the centre of the active region (as defined by Birch et al. 2013). This was done using bilinear interpolation using the four nearest pixels which sometimes affected the identified location of the polarities, particularly in the more dispersed, following polarity at later times (see Appendix 2.10.1). In this paper we first identify the locations of the polarities without shifting the maps, and then compute the locations relative to the active region centre. This procedure introduced differences in locations for some individual AR but this change does not affect the previous results presented in Schunker et al. (2019). Appendix 2.10.1 shows an example of the differences in position of the polarities for an individual active region and the resulting average position of the polarities.

Waves used for helioseismology are sensitive to scales larger than a few megametres, but to measure the location of the polarities it might be necessary to have a higher resolution. In Appendix 2.10.2 we show that the resolution of the maps does not significantly affect the average positions of the polarities or the tilt angle.

As in Schunker et al. (2019) we excluded 29 active regions where it was difficult to track the locations of the polarities correctly, or where the active regions have sustained anti-Hale orientation (see Appendix 2 in Schunker et al. 2019). Our statistical analysis of the tilt angles was based on the remaining 153 EARs.

In Schunker et al. (2019), active regions in the southern hemisphere had their polarities inverted, so that they had a negative leading polarity and a positive following polarity as for northern hemisphere regions, and were flipped in the latitudinal direction to account for Joy's law. Then the separation between the polarities in the y-direction, $\delta y(\tau) = y_\mathrm{l}(\tau) - y_\mathrm{f}(\tau)$, is negative (positive) when the leading polarity, y_l, is closer to (further from) the equator than the following polarity, y_f. The separation in the x-direction, $\delta x(\tau) = x_\mathrm{l}(\tau) - x_\mathrm{f}(\tau)$, is defined as positive (negative) when the leading polarity is in the prograde (retrograde) direction from the following polarity. From these measurements in Schunker et al. (2019), we define the tilt angle as

$$\gamma(\tau) = \arctan\left(\frac{-\delta y(\tau)}{\delta x(\tau)}\right). \tag{2.1}$$

The tilt angle is positive when the leading polarity is closer to the equator (and negative when it is further from the equator) than the following polarity (see Fig. 2.1).

2.4 Tilt angle as a function of active region evolution

Understanding the origin and evolution of the tilt angle, as well as the dependence of the tilt angle on flux will constrain models of active region emergence, and the location of the global toroidal magnetic field.

We averaged the tilt angle over all valid active regions at each time step, as well as over regions with a maximum flux higher than or equal to, and lower than the median 4.6×10^{21} Mx. In Table A.1 of Schunker et al. (2019) active regions with a maximum

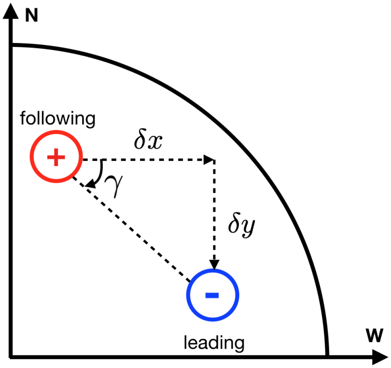

Figure 2.1: Sketch of the orientation of a pair of polarities with a positive tilt angle in the northern hemisphere during solar cycle 24 where the leading negative polarity is closer to the equator than the following positive polarity.

flux value higher than or equal to the median of the 105 active regions used in Schunker et al. (2016) have an asterisk. However, here we use the median value of the 153 valid active regions used in this paper. We found that at the time of emergence the tilt angle is small, 1.8 ± 2.2°(Fig. 2.2, top panel) and then increases over the course of the following day, after which it remains constant within the uncertainties. This excludes a constant tilt angle model, consistent with Fig. 2 in Schunker et al. (2019). This figure also shows that there is no significant dependence of the tilt angle on flux.

Fisher et al. (1995) found that at a fixed latitude, the tilt angle of white-light sunspot groups is smaller for polarities that are closer together, and hence have lower flux (Wang and Sheeley 1989, Howard 1992). However, we have shown that, within the errors, the tilt angle (and north-south separation) does not depend on the eventual maximum flux of the active region, and only on the evolutionary stage of the active region: large, high-flux active regions also begin as small, low-flux active regions with negligible inclination. Relative to our definition of emergence time (Schunker et al. 2016), on average the active regions do not show unambiguous intensity darkening in the HMI full-disk continuum until about one day after emergence, and circular sunspots with a well-defined penumbra only form about two days after emergence. So another possible interpretation of the results in Fisher et al. (1995) would be that many polarities that are close together have low flux and are near the beginning of emergence, whereas the polarities that are further apart have higher flux and are further evolved.

2.5 Scatter of the tilt angle as a function of time and flux

We found that on average the tilt angle increases as an active region emerges, but the evolution of the average tilt angle itself is not dependent on the maximum flux of the active region. Measuring the scatter in the tilt angle will help us to understand what

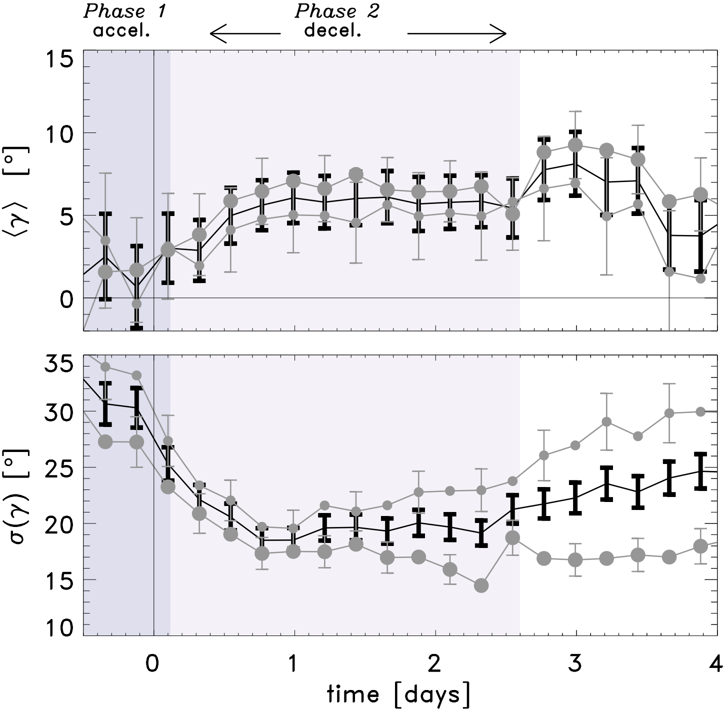

Figure 2.2: Averaged tilt angle (top) and standard deviation of the tilt angle (bottom) of the polarities as a function of time for all EARs (black), EARs with a higher (lower) maximum flux than the median in large grey circles (small grey circles). The EARs are divided into higher than or equal to, and lower than, the median maximum flux value, 4.6×10^{21} Mx. The standard deviation of the sample standard deviation at each time interval is described in Schunker et al. (2019, Appendix E). The shaded regions indicate two different phases of emergence, an increasing separation speed between the polarities followed by a decreasing separation speed (Schunker et al. 2019).

causes the deviations from Joy's law.

We found that the scatter in the tilt angle at the emergence time (when the active regions are small and close together) is large, 25 ± 2°, and decreases, to about 20 ± 1°, over the first day after emergence (bottom panel Fig. 2.2). This is consistent with previous observations showing that there is less scatter in the tilt angle of high-flux regions (e.g. Stenflo and Kosovichev 2012, Jiang et al. 2014), and demonstrates that the evolutionary stage of the active region is an important factor when characterising the tilt angle.

Schunker et al. (2019) showed that the scatter in the motion of the polarities is largely independent of flux, but that the scatter increases with time and that the scatter of the leading polarity is systematically larger than the following polarity. The following polarity is known to be more diffuse than the leading polarity, and Schunker et al. (2019) argued that both polarities are buffeted equally by supergranulation, but that the centre of gravity of the following polarity is not significantly affected by buffeting at its edges. From this argument, larger, higher-flux regions would be expected to have less scatter in their tilt angles due to their larger size, and not a stronger resistance to buffeting by convection. In the bottom panel of Fig. 2.2 we show that this is true after about one day after emergence. The scatter in the tilt angle for higher-flux regions remains roughly constant after this. However, the scatter in lower-flux regions continues to increase; this is probably due to the short lifetimes and decay of weak active regions (e.g. Schunker et al. 2016).

2.6 Tilt angle and separation as a function of latitude

Joy's law states that the average tilt angle of active region polarities increases with latitude, for example as measured by Wang and Sheeley (1991) from line-of-sight magnetograms as $\sin\gamma = 0.48 \sin\lambda + 0.03$ where λ is unsigned latitude. To reflect this definition, we multiplied the north-south displacement and the tilt angle by the sign of the latitude of the active region for the remaining analysis, $\mathrm{sgn}(\lambda)\gamma$ and $\mathrm{sgn}(\lambda)\delta y$. Therefore, active regions that obey Joy's law will have a negative tilt angle and positive north-south displacement in the southern hemisphere.

We examined the longitudinal and latitudinal separation, as well as the tilt angle of the polarities as a function of latitude. Figure 2.3 (left) shows that at the emergence time, `TI+00`, the active regions have an east-west separation of about 20.3 ± 0.6 Mm, a north-south separation of -1.1 ± 0.7 Mm, and a small tilt angle of about $1.8 \pm 2.2°$ (recalling that there is already observable flux at the surface at this time). As expected from Schunker et al. (2019), low-flux regions tend to be closer together than large flux regions. Joy's law is not evident because neither the separation nor the tilt angle varies significantly from the mean. This is not consistent with thin flux tube simulations, where the flux tubes are tilted by the latitudinally dependent Coriolis effect acting as the tubes rise to the surface (e.g. Weber et al. 2011). These simulations are valid in the regions where convection is relatively weak, and so in the remaining rise through the convection towards the surface this tilt angle would have to be somehow undone or hidden to accommodate the observations. However, the east-west orientation is consistent with the surface activity representing the subsurface toroidal flux (e.g. Parker 1955, Cameron et al. 2018).

In this section we have excluded ten additional active regions (11122, 11242, 11327, 11396, 11597, 11686, 11736, 11843, 11978, 12011) because they did not have valid

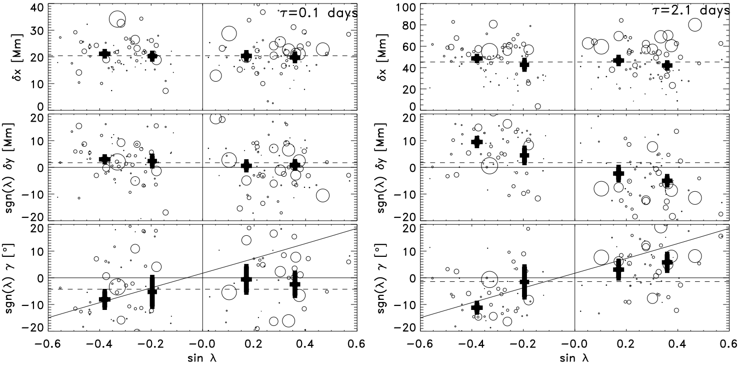

Figure 2.3: East-west separation, δx (top); north-south separation, δy (middle); and tilt angle, γ (bottom) of the polarities as a function of latitude, λ, at the emergence time (left) and two days later (right). The sign of the north-south separation and the tilt angle of active regions in the southern hemisphere have been adjusted, i.e. in the southern (northern) hemisphere a negative (positive) δy and a negative (positive) γ is consistent with Joy's law (black curve, Wang and Sheeley 1991). The size of the circle is proportional to the maximum flux of the active region. The thick black points with error bars show latitudinal averages between 0 and 15° ($\sin\lambda = 0.26$) and 15° to 40° ($\sin\lambda = 0.64$) in the northern hemisphere, and the equivalent in the southern hemisphere. The dashed lines are the mean values.

position measurements at both `TI+00` and `TI+09`. There are three active regions that maintain a large anti-Joy tilt angle, two in the southern hemisphere AR 11400 ($\lambda = -14°$, $\mathrm{sgn}(\lambda)\gamma = 80°$ at `TI+09`), AR 11780 ($\lambda = -8°$, $\mathrm{sgn}(\lambda)\gamma = 72°$ at `TI+09`) and one in the northern hemisphere AR 11146 ($\lambda = 23°$, $\mathrm{sgn}(\lambda)\gamma = -68°$ at `TI+09`). We keep these active regions in our analysis; excluding these active regions does not change the results dramatically.

Figure 2.3 (right) shows the displacement and tilt angle of the active region polarities two days after emergence. The east-west separation has increased to 44.7 ± 1.4 Mm, retaining the expected flux dependence, and the north-south separation now varies with latitude, suggesting that whatever drives the north-south separation is responsible for the tilt angle. We find no dependence of the north-south separation on flux.

2.7 Discussion of the Coriolis effect

The Coriolis force acts perpendicular to the direction of motion and to the axis of rotation. In the thin flux tube theory it acts on east-west flows in the flux tube driving a north-south displacement of the legs of the flux tube: flux tubes with higher magnetic flux have faster east-west flows and larger tilt angles. We do not find, however, any evidence of flux dependence in the tilt angle.

Schunker et al. (2019) estimated the north-south separation speed numerically $\dot{\delta y}(i) = (\delta y(i+1) - \delta y(i-1)) \,/\, (\tau(i+1) - \tau(i-1))$, where i is the temporal index, and similarly for the east-west separation speed $\dot{\delta x}$, and $\dot{\delta}(i) = \sqrt{\dot{\delta x}(i)^2 + \dot{\delta y}(i)^2}$. This revealed two clear phases of the emergence: Phase 1, when the speed of the separation between the polarities is increasing (accelerating), followed by Phase 2, when the speed is decreasing (decelerating). We indicated these phases for the tilt angle in Fig. 2.2.

The north-south separation speed is dependent on latitude at the time of emergence during Phase 1 (Fig. 2.4). This demonstrates that the polarities emerge mostly east-west aligned, imbued with an inherent north-south velocity that is consistent with Joy's law. It is not clear what drives this north-south velocity. Given its dependence on latitude, a natural conclusion is that the Coriolis force is responsible, but it is not clear upon which east-west velocities it is acting. Naively, the Coriolis force should produce an acceleration in the north-south direction, but we see from Fig. 4 in Schunker et al. (2019) that the acceleration of the separation 0.1 days after emergence, at the end of Phase 1, is zero within the uncertainties. This means that if the Coriolis force is acting, then it is only during a relatively short time to initiate the north-south velocity, or it is counteracted by an equal and opposite force. One candidate is the drag force (e.g. Fan 2009).

In Appendix 2.10.3 we model the expected separation of the polarities as a function of time and latitude for three models: a constant tilt angle model, the Coriolis effect acting on the east-west separation speed of the polarities, and a constant initial velocity model. Our models show that a constant tilt angle model is not viable (as already shown in Fig. 2, Schunker et al. 2019). However it is difficult to conclude anything further due to the large uncertainties in the separation of the polarities.

2.8 Implications for the tilt angle relaxation

Howard (1996) observed the tendency for the tilt angle to move towards a more east-west orientation after emergence, which is not what is expected from the Coriolis force, and described it as a 'relaxation'. This was interpreted in terms of magnetic tension by Longcope and Choudhuri (2002). In this interpretation the tilt angle evolves towards the position of the tube at the depth where the tube is disconnected, and they determined that this was likely to be occurring at the base of the convection zone. The initial scatter in the positions of the two polarities, imparted by the turbulent convective motions in the upper convection zone, should dissipate as the magnetic field at the surface becomes stronger and less susceptible to buffeting by the convective motions (e.g. Longcope and Choudhuri 2002, Tóth and Gerlei 2004). In Fig. 2.5 we also show that the tilt angles appear to develop a more east-west orientation, at a rate of $-0.33 \pm 0.06^\circ$ per day (the change in tilt angle over two days).

Schunker et al. (2019) established that the average east-west separation of the polarities is larger than the average separation in the north-south direction. This east-west motion would cause a change in the measured tilt angle, rather than a circular motion of the polarities about a common centre.

To test this idea, we modelled the change in tilt angle, $\Delta\gamma_{\mathrm{est}}$, due to the change in the east-west separation of the polarities only, by using the measured $\Delta x = \delta x(\tau = 2.1 \text{ days}) - \delta x(\tau = 0.1 \text{ day})$ and leaving δy constant at $\delta y(\tau = 0.1 \text{ day})$. In Fig. 2.5 the red circles

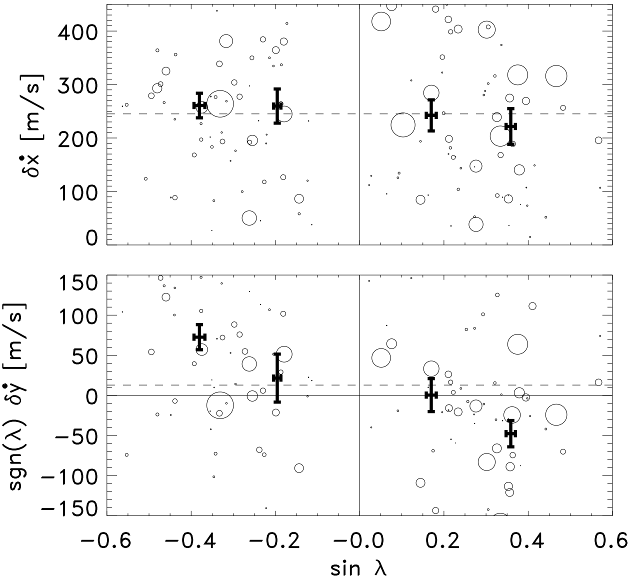

Figure 2.4: Separation velocity of the polarities in the east-west direction, $\dot{\delta x}$, (top panel) and the north-south direction, $\dot{\delta y}$, (bottom panel) at the emergence time, `TI+00`, as a function of latitude, λ. The size of the circle is proportional to the maximum flux of the active region. The thick black points with error bars show the averages over different ranges of latitude (between 0 and 15° ($\sin\lambda = 0.26$) and 15° to 40° ($\sin\lambda = 0.64$) in the northern hemisphere, and the equivalent in the southern hemisphere). The dashed lines are the mean values.

represent

$$\Delta\gamma_{\mathrm{est}} = \arctan\left(\frac{-\delta y(\tau = 0.1\ \mathrm{day})}{\delta x(\tau = 2.1\ \mathrm{day})}\right) - \gamma(\tau = 0.1\ \mathrm{day}), \tag{2.2}$$

and we can see that this reproduces much of the apparent relaxation.

If we subtract the model tilt angle, $\Delta\gamma_{\mathrm{est}}$, the dependency of the change in tilt angle on the initial tilt angle vanishes. From our analysis of the independent motion of the polarities we have demonstrated that what was previously interpreted as a tilt angle relaxation is a straightforward consequence of the east-west separation of the polarities. Any constraints placed on models of emerging flux tubes using the apparent tilt angle relaxation need to be carefully reconsidered.

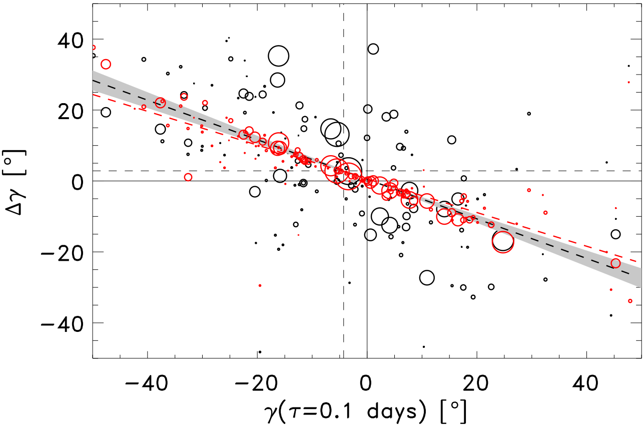

Figure 2.5: Change in tilt angle, Δγ, between τ = 2.1 day and τ = 0.1 day as a function of the tilt angle, γ, at the emergence time (grey circles). The size of the circle represents the maximum flux of the active region. The dotted grey line is a linear best fit to the observed Δγ (grey circles) with a slope of -0.65 ± 0.06 , and the shaded grey area indicates the uncertainty in the fitted slope parameter. The red circles are the expected change in tilt angle for each EAR if only δx changed and δy remained constant (see Eqn. 2.2). The red dotted line is a linear best fit to the red circles with slope -0.52 ± 0.06.

2.9 Summary and discussion

Our finding that, on average, active regions emerge with an east-west alignment is consistent with earlier observations, but is still surprising since thin-flux-tube models predict that tilt angles of rising flux tubes are generated below the surface.

Our results show that the forces driving Joy's law are observed as an inherent north-south separation speed of the polarities that depends on latitude but is independent of flux. The origin of the north-south separation remains unclear. Our results indicate that if it is due to the Coriolis effect acting on flows within the emerging flux tube, then the flows in the tube must be largely directed away from the loop apex and independent of flux.

Chen et al. (2017) simulate the emergence of a thin flux tube through the top 20 Mm of the convection zone. The locations of the polarities at the surface lie above the location of the polarities at the footpoints (bottom of the box). The simulations do not include solar rotation per se, but the time evolution of the flux tube at the bottom boundary does. The simulation of one single active region cannot be directly compared to an average of many active regions, and so we are hesitant to compare the tilt angle development.

One explanation for the initial observed east-west orientation is that the initial emerging flux tube has the correct amount of twist and writhe (e.g. López Fuentes et al. 2003) so that the field at the apex of the emerging loop is east-west aligned. When the apex breaks the surface, the twisted field is aligned east-west, with Joy's law developing as the writhe becomes more evident.

It is known that there is a relationship between the supergranulation pattern and where flux emergence occurs (Birch et al. 2019). We speculate that if the supergranulation is guiding the initial emergence process an alternative explanation for our results is that the emergence into predominantly east-west aligned north-south converging flows (Birch et al. 2019) leads to a preference for east-west alignment of the polarities. Why the emergence location is preferentially in east-west aligned inflows is not clear.

Our findings are consistent with the model of emerging flux as presented in Schunker et al. (2019). During Phase 1, active region polarities emerge east-west aligned (zero tilt angle) with an increasing separation speed, which lasts until about 0.5 day after the emergence time, and the tilt angle begins to develop. Phase 2 begins when the separation speed starts to decrease, until the polarities stop separating about $2.5 - 3$ days after the time of emergence. The latitudinal dependence of the tilt angle, characteristic of Joy's law sets in during this second phase. In the first day after emergence, the scatter in the tilt angle decreases independent to the maximum flux, consistent with the polarities being buffeted by near-surface convection as they move to lie over their footpoints anchored at some depth below the surface. Analysis of the flows at and below the surface leading up to the emergence will help to constrain the subsurface picture.

Acknowledgements

CB is a member of the International Max Planck Research School for Solar System Science at the University of Göttingen. CB tested the reproducibility of the results and high-resolution tests, specifically Appendix A and Appendix B. The German Data Center for SDO, funded by the German Aerospace Center (DLR), provided the IT infrastructure for this project. Observations courtesy of NASA/SDO and the HMI science teams. ACB, RHC, and LG acknowledge partial support from the European Research Council Synergy Grant WHOLE SUN #810218. This work utilised the Pegasus workflow management system. DCB is supported by the Solar Terrestrial program of the US National Science Foundation (grant AGS-1623844) and by the Heliophysics Division of NASA (grants 80NSSC18K0068 and 80NSSC18K0066).

2.10 Appendix

2.10.1 Polarity centres identified by shifting the search mask for AR 11072

As described in Section 2 of Schunker et al. (2019), we define a search area to be limited to all pixels within a radius of 100 Mm from the centre of the map, with magnetic field strength averaged over all active regions greater than 10 G. This resulted in a roughly circular search area at the centre of the map for early time intervals, which increased in size, and became more elliptical with the semi-major axis in the east-west direction in time. The search mask is the corresponding map where pixels that satisfy this condition have a value of 1, and 0 otherwise.

We then shifted the individual line of sight magnetic field maps so that the location of emergence was at the centre. This shift used a bilinear interpolation over four pixels. We found that at later times, when the following polarity is more dispersed, if we did not shift the maps, but instead shifted the search mask to lie over the location of the emergence, the displacement of some of the features relative to the active region centres was significantly different.

Figure 2.6 shows an example of the location of the following and leading polarities for AR 11072. This example shows the differences in the location of the leading and following polarity computed by either shifting the magnetic field maps or the search mask, which can be significant for an individual active region. Figure 2.7 shows the maps for `TI+09` where the bilinear interpolation of the magnetic field map can cause a significant difference in the identified location of the following polarity, and `TI+10` where it does not. The largest difference is where the bilinear interpolation has introduced values a factor of five larger (> 900 G, in the white region below the red cross in the `TI+09` difference map). This moves the centre of gravity of a 25 pixel diameter feature more in this direction. In the case of `TI+10`, the interpolator does not introduce such large differences. However, in Fig. 2.8, which is an updated version of Fig. 2, Schunker et al. (2019) shows that there are no significant differences in the average polarity positions.

2.10.2 Polarity centres identified in high-resolution maps

For helioseismology purposes it is sufficient to have a coarser resolution (about 1.4 Mm per pixel) than nominally observed by HMI (about 0.35 Mm per pixel) since the waves are not sensitive to these scales. However, when measuring the location of the polarities, it could be the case that a higher resolution is required for a more precise result.

We repeated our analysis using high-resolution time-averaged line-of-sight magnetic field maps at 0.35 Mm per pixel and shifting the search mask. The high-resolution maps show more structure in the polarities than the low-resolution maps, particularly for the more dispersed following polarity (see Fig. 2.9). This makes identifying the primary polarity more difficult at later times, and so we retain the threshold parameters used in the low resolution case, in particular we still search for features with a diameter of 35 Mm. The search area (see black contour in Fig. 2.9) is based on the average of 78 emerging active regions (listed below), and so it is similar but not identical to the search area used in the main analysis of the paper and Schunker et al. (2019). As an example, we show the position of the polarities and the tilt angle for both low- and high-resolution maps of some example active regions in Fig. 2.9.

We computed the average position of 78 active regions as a representative subset in the high-resolution maps (Fig. 2.10). There is no significant difference between the average position of the polarities in the high- and low-resolution maps of the same 78 active regions. For our purposes of identifying the location of the primary leading and following polarities, the lower resolution maps suffice.

The subset of 78 emerging active regions used to compare the locations of the polarities in the high- and low-resolution time-averaged line-of-sight magnetogram maps are the following: 11066, 11070, 11072, 11074, 11075, 11076, 11079, 11080, 11081, 11086, 11088, 11098, 11103, 11105, 11114, 11116, 11122, 11130, 11132, 11136, 11137, 11138, 11141, 11142, 11143, 11145, 11146, 11148, 11152, 11154, 11156, 11157, 11158, 11159, 11167, 11174, 11182, 11290, 11291, 11294, 11297, 11300, 11304, 11310, 11311, 11318, 11322, 11326, 11327, 11331, 11334, 11370, 11381, 11385, 11396, 11397, 11400, 11404,

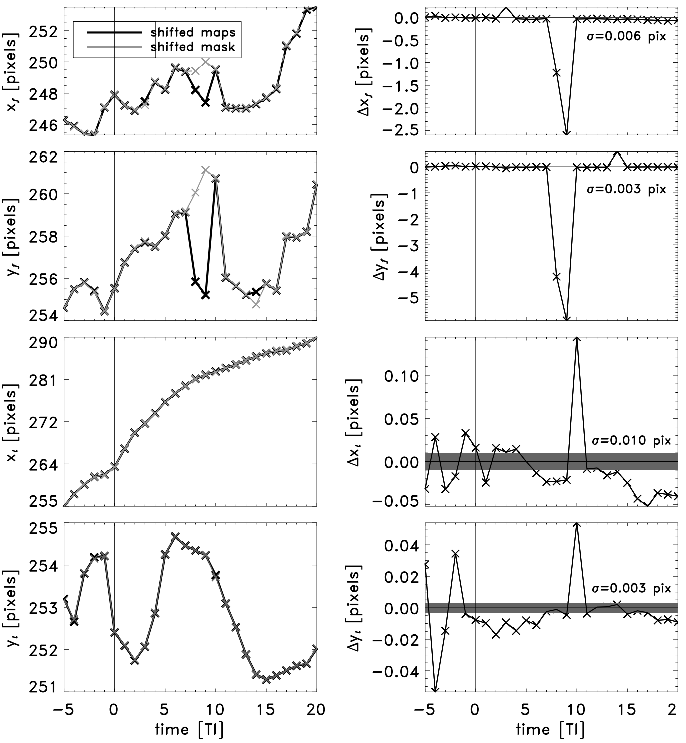

Figure 2.6: Comparison of polarity centres identified by shifting the magnetic field maps (previous algorithm) and shifting the search mask (updated algorithm) for AR 11072. The left column shows the feature locations from the previous algorithm (black) and the updated algorithm (grey) in the x and y directions of the following polarity (x_f, y_f, top two rows) and leading polarity (x_l, y_l, bottom two rows). The right column shows the difference between the previous and updated algorithm. The grey shaded regions indicate the uncertainty in the data (also given by σ) from averaging every fourth image of `TI+02` datacube of AR 11072 and finding the feature (as shown for AR 11075 in Schunker et al. 2019, , Appendix D). The differences can be outside of the uncertainties in the data. AR 11072 is an active region in the southern hemisphere. The active region is shown with the sign of the polarities inverted and the map reversed in the latitudinal direction, as used in the statistical analysis.

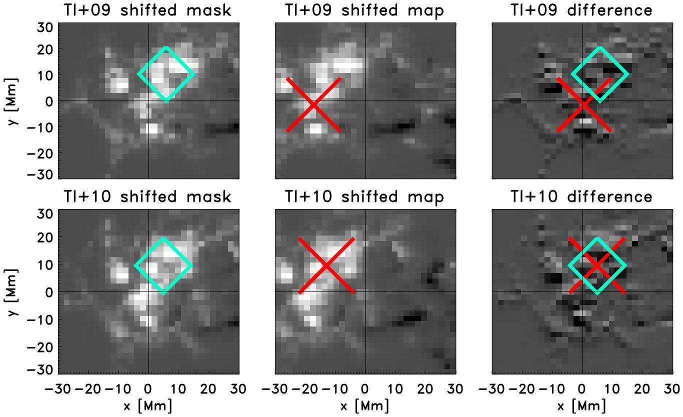

Figure 2.7: Line-of-sight magnetic field maps and identified locations of the positive (following) polarity at `TI+09` (top row) and `TI+10` (bottom row) of example active region 11072. The greyscale is from −500 G to 1200 G. The left panel shows the map and location of the polarity (teal diamond) by shifting the search mask. The middle panel shows the location of the polarity (red cross) after shifting the magnetic field map using bilinear interpolation. The size of the symbol is proportional to the radius of the detected feature. The right panel shows the difference accounting for the integer shift in the maps. The root mean square of the difference map is 147 G. The largest absolute difference (> 900 G) occurs in the white region below the red cross in the `TI+09` difference map.

11406, 11414, 11416, 11431, 11437, 11446, 11449, 11450, 11456, 11466, 11472, 11497, 11500, 11510, 11511, 11523, 11531, 11547, 11549, 11551.

2.10.3 Modelling the latitudinal separation between polarities during emergence

In this section we explore the change in tilt angle in relation to the Coriolis force, separation speed, and lifetime of the active regions in the SDO/HEARs database.

We explore three models to describe the north-south displacement:

1. Constant tilt angle: It has been suggested that the flux tube arrives at the surface already tilted satisfying Joy's law (e.g. Weber et al. 2013), but distorted by convection. Here we test if it is statistically possible that the regions have a constant tilt angle. We model the north-south displacement due to a constant tilt angle at the time of emergence, as $\delta y(\tau) = -\tan\left[\gamma(\tau = 0)\right]\delta x(\tau)$.

2. Coriolis effect: Joy's law is a function of latitude, reminiscent of the Coriolis force. Howard (1994) showed that bipolar magnetic regions (identified in white light im-

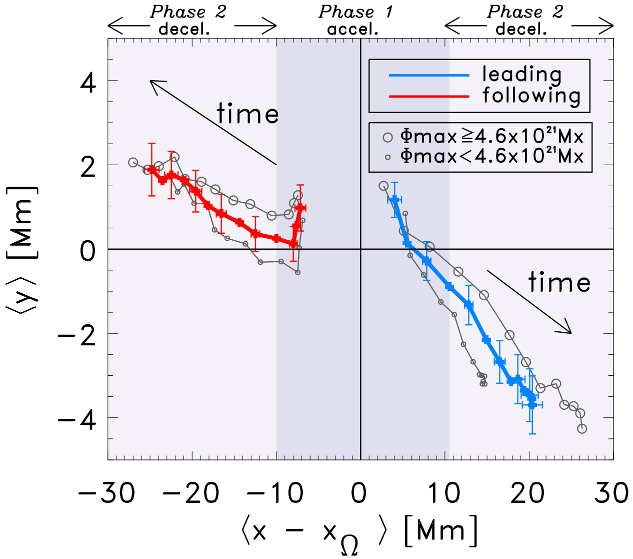

Figure 2.8: Updated Fig. 2 from Schunker et al. (2019) using the updated algorithm. Average over the position of 153 positive (red) and negative (blue) polarities relative to the corrected centre of the map from $\tau = -18.4$ hours (three time intervals, `TI-03`) before the emergence time, until $\tau = 2.1$ days after (`TI+09`). The centre of each of the maps were tracked at the Carrington rotation rate (Snodgrass 1984). We corrected the centre of the map by subtracting the displacement due to difference between the quiet-Sun plasma rotation rate $x_\Omega = R_\odot \Omega(\lambda) \cos(\lambda) \Delta\tau$, where λ is the latitude of the centre of the Postel projected map (see Table A.1 in Schunker et al. 2016). The blue and red curves cover the time intervals from `TI-03` to `TI+09`. The grey lines with large (small) circles shows the motion of the polarities belonging to regions with maximum flux higher (lower) than the median flux. The shaded regions indicate Phase 1, when the separation speed between the polarities increases, and Phase 2 when the separation speed decreases (see Fig. 4, Schunker et al. 2019).

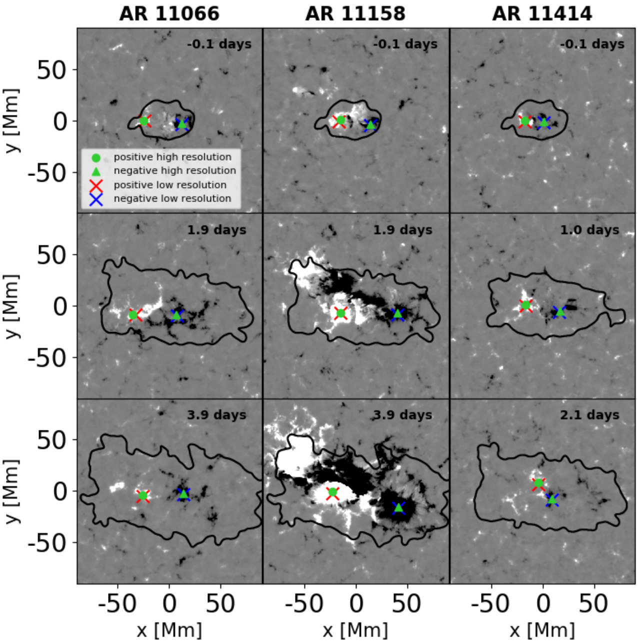

Figure 2.9: Similar to Fig. 1 in Schunker et al. (2019). High-resolution (0.35 Mm per pixel) time-averaged line-of-sight magnetogram maps of AR 11066 (left), AR 11158 (middle), and AR 11414 (right). These high-resolution maps can be directly compared with the low-resolution maps in Fig. 1 in Schunker et al. (2019). The grey scale is ±1000 G. The black contour indicates the search area to identify the polarities in the high-resolution maps. The green triangle (circle) shows the position of the negative (positive) polarity identified using the high-resolution maps. The position of the negative (blue cross) and positive (red cross) polarities computed from the low-resolution (1.4 Mm per pixel) time-averaged line-of-sight magnetograms are shown for comparison.

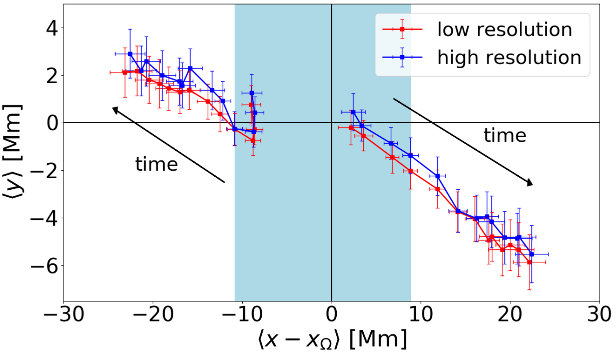

Figure 2.10: Average position of the polarities from $\tau = -18.4$ h (three time intervals, `TI-03`) before the emergence time, until $\tau = 2.1$ days after (`TI+09`) increasing in distance away from the centre. This figure is similar to Fig. 2 Schunker et al. (2019), except that only 78 of the emerging active regions have been used in both the low- and high-resolution cases (red and blue, respectively). Differences between the high- and low-resolution cases do not change our previous science conclusions or about the onset of Joy's law. The blue shaded region indicates Phase 1 of the emergence process (Schunker et al. 2019) when the polarity separation speed is increasing.

ages) that move further apart or closer together change tilt angle in the sense expected from the Coriolis force acting on this change in separation. This study only considered day-to-day changes in separation and tilt, and not the evolutionary stage of the bipolar magnetic regions. Here we model the north-south displacement of the polarities due to the Coriolis force given the east-west separation speed and the surface latitudinal differential rotation. The Coriolis acceleration in the north-south direction, $\delta\ddot{y}_C(\tau)$, acting on a velocity in the east-west direction, $\delta\dot{x}(\tau)$, in a coordinate system rotating at the local rotation rate, Ω, is

$$\delta\ddot{y}_C(\tau) = -2\,\Omega\,\sin\lambda\,\delta\dot{x}(\tau), \tag{2.3}$$

where λ is the latitude and τ is time. The displacement in the north-south direction is related to the velocity and acceleration, a as

$$\begin{aligned}
\delta y(\tau) &= \int_{\tau_0}^{\tau} \delta\dot{y}_C(\tau')\mathrm{d}\tau' + \delta y(\tau_0) \\
&= \int_{\tau_0}^{\tau}\left(\int_{\tau_0}^{\tau'} \delta\ddot{y}_C(\tau'')\mathrm{d}\tau'' + \delta\dot{y}(\tau_0)\right)\mathrm{d}\tau' + \delta y(\tau_0) \\
&= \int_{\tau_0}^{\tau}\left(\int_{\tau_0}^{\tau'} -2\Omega\sin\lambda\,\delta\dot{x}(\tau'')\mathrm{d}\tau'' + \delta\dot{y}(\tau_0)\right)\mathrm{d}\tau' + \delta y(\tau_0) \\
&= \int_{\tau_0}^{\tau}\left(-2\Omega\sin\lambda\,[\delta x(\tau'')]_{\tau_0}^{\tau'} + \delta\dot{y}(\tau_0)\right)\mathrm{d}\tau' + \delta y(\tau_0) \\
&= -2\Omega\sin\lambda\left(\int_{\tau_0}^{\tau} \delta x(\tau')\mathrm{d}\tau' - \delta x(\tau_0)[\tau-\tau_0]\right) \\
&+ \delta\dot{y}(\tau_0)[\tau-\tau_0] + \delta y(\tau_0).
\end{aligned} \tag{2.4}$$

In this derivation we assumed that any changes in λ in time have a small effect on $\sin\lambda$ and $\Omega(\lambda)$. We set $\tau_0 = 0$ and refer to the three terms in this equation separately as the Coriolis component of displacement $\delta y_C = -2\Omega\sin\lambda\left(\int_0^{\tau}\delta x(\tau')\mathrm{d}\tau' - \delta x(0)\tau\right)$, the initial north-south velocity component of displacement, $\delta y_P = \delta\dot{y}(0)\tau$, and the initial displacement component, $\delta y_0 = \delta y(0)$.

3. Initial north-south velocity component of displacement: Removing the Coriolis effect from Eq. 2.4 leaves $\delta y(\tau) = \delta y_P + \delta y_0$.

First we compare the models to the observations as a function of time in the first two days after emergence. We have selected only the EARs which have valid measurements in each time interval from $\tau = 0.1$ days to $\tau = 2.1$ days (see Table B.1 in Schunker et al. 2019). Fig. 2.11 shows that the constant tilt angle model can be excluded: the displacement in the north-south direction would not change significantly given the change in separation in the east-west direction. The north-south displacement due to the constant, initial north-south velocity component of displacement agrees with the measured displacement best, and the addition of the Coriolis effect acting on the east west separation speed is relatively small.

We then compare the models to the observations as a function of latitude. We measure the change over the first two days after emergence in the separation between the polarities, $\Delta x = \delta x(\tau = 2.1\text{ days}) - \delta x(\tau = 0.1\text{ days})$ and $\Delta y = \delta y(\tau = 2.1\text{ days}) - \delta y(\tau = 0.1\text{ days})$, and the change in tilt angle, $\Delta\gamma = \gamma(\tau = 2.1\text{ days}) - \gamma(\tau = 0.1\text{ days})$. The time interval is given in units of days (see Table B.1 in Schunker et al. 2019). Figure 2.12 shows the change in displacement and tilt angle over two days as a function of latitude. The separation in the east-west direction is not dependent on latitude, however, the separation in the north-south direction and the tilt angle is, showing that the tilt angle comes predominantly from the north-south motion. Again, we see that the constant tilt angle model cannot explain the north-south displacement.

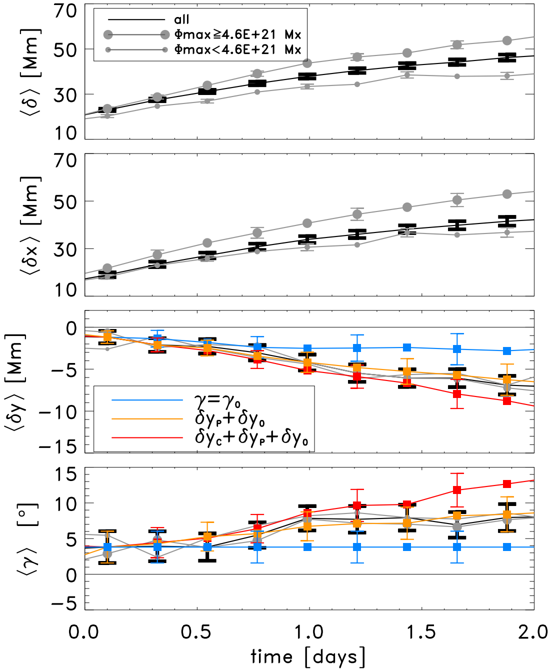

Figure 2.11: Median separation (top three panels) and tilt angle (bottom panel) of 95 EARs with valid measurements of their location at all times from $\tau = 0.1$ to $\tau = 2.1$ days (black curve). This is less than the 153 active regions used in the body of the paper because in this case the EAR is required to have a valid measurement at all time intervals shown. This does not change the results significantly from using all EARs with valid measurements at each time. High- and low-flux observation samples are indicated by the size of the grey circles. Bottom two panels the coloured curves show the different models of displacement and tilt angle, and grey represents the observations.

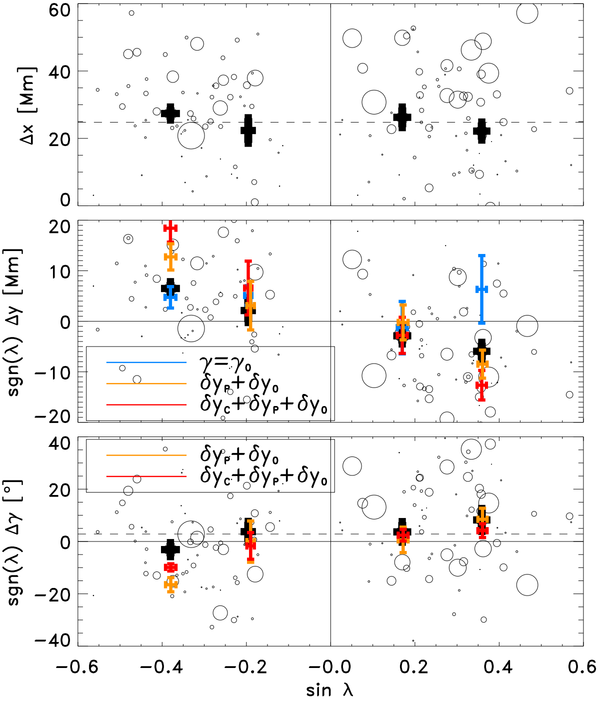

Figure 2.12: Change in east-west separation, Δx, (top panel); north-south separation, Δy, (second panel); and change in tilt angle, $\Delta\gamma$ (bottom panel) in the first two days after emergence as a function of latitude, λ. The size of the circle is proportional to the maximum flux of the active region. The thick black points with error bars show the averages for active regions in different latitude ranges. The coloured points with error bars show latitudinal averages (between 0° and 15° ($\sin\lambda = 0.26$) and 15° and 40° ($\sin\lambda = 0.64$) in the northern hemisphere, and the equivalent in the southern hemisphere) for the modelled north-south separation and change in tilt angle for the constant tilt angle model in blue, the Coriolis effect in red, and the initial north-south velocity of the polarities in yellow.

3 Impact of spatially correlated fluctuations in sunspots on metrics related to magnetic twist

3.1 Abstract

The twist of the magnetic field above a sunspot is an important quantity in solar physics. For example, magnetic twist plays a role as in the initiation of flares and CMEs. Various proxies for the twist above the photosphere, motivated by models of uniformly-twisted flux tubes, are routinely computed from single photospheric vector magnetograms. One class of proxies is based on α_z, the ratio of the vertical current to the vertical magnetic field. Another class of proxies is based on the so-called twist density, q, which depends on the ratio of the azimuthal field to the vertical field. However, the sensitivity of these proxies to temporal fluctuations of the magnetic field has not been well characterized yet.

We aim to determine the sensitivity of twist proxies to temporal fluctuations of the magnetic field as estimated from time series of SDO/HMI vector magnetic field maps.

In order to do so, we introduce a model of a sunspot with a peak vertical field of 2370 Gauss at the photosphere and a uniform twist density $q = -0.024\ \mathrm{Mm}^{-1}$. We add realizations of the temporal fluctuations of the magnetic field that are consistent with SDO/HMI observations, including the spatial correlations. Using a Monte-Carlo approach, we determine the robustness of the different proxies to the temporal fluctuations.

The temporal fluctuations of the three components of the magnetic field are correlated for spatial separations up to 1.4 Mm (more than expected from the point spread function alone). The Monte-Carlo approach enables us to demonstrate that several proxies for the twist of the magnetic field are not biased in each of the individual magnetograms. The associated random errors on the proxies have standard deviations in the range between 0.002 to 0.006 Mm^{-1}, smaller by approximately one order of magnitude than the mean value of q.[1]

---

[1] This chapter reproduces the article *Impact of spatially correlated fluctuations in sunspots on metrics related to magnetic twist* C. Baumgartner, A. C. Birch, H. Schunker, R. H. Cameron and L. Gizon, accepted by Astronomy and Astrophysics (17.03.2022). C. Baumgartner modelled the sunspot with spatially correlated fluctuations of the magnetic field, conducted the Monte-Carlo simulations, contributed to the interpretation of the results and wrote the manuscript.

3.2 Introduction

The magnetic field in solar active regions is often modelled by coherent bundles of magnetic field lines, so-called flux tubes. The magnetic helicity $H = \int_V \mathbf{A} \cdot \mathbf{B} \, dV$, where $\mathbf{A}$ is the magnetic vector potential and $\mathbf{B}$ is the magnetic field, can be used to describe the topological structure of flux tubes fully contained in a volume V (Berger and Field 1984). The magnetic helicity of a single flux tube has two components: writhe, which measures the deformation of its axis, and twist. If one imagines the magnetic field as a straight ribbon with each end being rotated in opposite directions, the twist T measures how often the ribbon turns around its straight axis

$$T = qL, \tag{3.1}$$

where L is the length of the ribbon and q is the twist density, which counts how often the ribbon fully turns per unit length.

Measurements of the magnetic field's twist play an important role in many different areas of solar physics: The twist distribution in the photosphere constrains models of the solar dynamo and magnetic flux emergence (e.g. Gilman and Charbonneau 1999, Brandenburg 2005, Pipin et al. 2013). As an example, the hemispheric helicity sign rule describes an observed latitudinal dependence of the twist with predominantly negative(counter-clockwise)/positive(clockwise) twist in the Northern/Southern hemisphere (Seehafer 1990, Pevtsov et al. 1995, Longcope et al. 1998, Nandy 2006), which is a key ingredient that solar dynamo models should be able to reproduce (Charbonneau 2020). The magnetic field's twist plays an essential part in the dynamics of the solar atmosphere, e.g. a highly twisted flux tube can become susceptible to kink-instability, which leads to a deformation of the flux tube's axis in exchange for its twist. This is a possible trigger mechanism for solar flares and coronal mass ejections (e.g. Török and Kliem 2003, Török et al. 2004, Leka et al. 2005, Fan 2005). Furthermore, the observed twist of photospheric magnetic field is used as an input to inject twist into coronal magnetic field extrapolations (e.g. Yeates et al. 2008, Wiegelmann and Sakurai 2012).

Various methods have been developed to measure the magnetic field's twist density in active regions directly from individual photospheric observations. These methods either use the force-free parameter, α, as a proxy for the twist density or try to fit the twist density directly.

Woltjer (1958) shows that the force-free parameter α in a closed system corresponds to the helicity content of a linear force-free field structure in its lowest attainable energy state. Therefore, α is used in observations as a proxy for the magnetic field's helicity (Pevtsov et al. 2014).

Since we have observations at only one height in the photosphere from instruments like HMI, we cannot measure α directly. We are limited to calculating the vertical current density J_z and consequently $\alpha_z = J_z/B_z$ at one height, where B_z is the vertical field strength. Burnette et al. (2004) studied 34 active regions and show that a 2-dimensional spatial average of α_z over an active region is correlated with the α value corresponding to the 3-dimensional linear-force free extrapolation with the best least-squares fit to the observed field. Therefore, spatial averages of α_z are often used to characterize the magnetic field's helicity and twist in active regions or individual sunspots (e.g., Longcope et al. 1998, Hagino and Sakurai 2004). Leka et al. (2005) chose a single peak value of α_z close to a sunspot's center (α_{Peak}) to characterize the magnetic field's twist. This is because in simple models α_z relates only at the axis of a flux tube directly to the twist density ($\alpha_{\text{Peak}} = 2q$).

Nandy et al. (2008) suggested a method to infer the magnetic field's twist density q that avoids the force-free assumption. They assume that the magnetic field in a sunspot can be approximated by a monolithic vertical flux tube with a constant twist density. Then they use a least-squares fitting approach to fit the observations to this reference model to obtain the twist density.

Various tests of these methods have been conducted. Leka and Skumanich (1999) and Leka (1999) used observations to compare methods of using moments of the distribution of α_z, a global α from force-free extrapolations, and a fitting approach of the function $J_z = \alpha B_z$. They find a quantitative agreement between these methods. They assessed the influence of instrumental effects like spatial resolution and a limited field-of-view. They also considered noise, by restricting the α_z measurements to certain noise thresholds. Leka et al. (2005) successfully retrieved the twist density using their α_{Peak} method on a model by Fan and Gibson (2004) in the absence of errors. Crouch (2012) evaluated different least-squares fitting methods of the twist density from a model flux tube. They find that the inferred twist density can be significantly different depending on the model assumptions used for fitting, also in the absence of noise. Tiwari et al. (2009b) used a linear force-free magnetic field model to test the effect of random polarimetric noise on estimates of the global α value of the synthetic field structure. They find that noise does not influence the sign of α and the global twist can be measured accurately.

To interpret twist density measurements from a single observation, we need to understand how these measurements are affected by temporal variations of the magnetic field. HMI observes the magnetic field in the photosphere, where the force-free assumption is thought to be violated (Gary 2001). Temporal fluctuations of the magnetic field may arise in such an environment, e.g. a twisted magnetic field structure can be distorted by its surrounding plasma flows. We need to model the fluctuations of the magnetic field in a sunspot from SDO/HMI observations to characterize the sensitivity of twist measurements to these fluctuations.

We plan to test the robustness of existing methods to infer the magnetic field's twist under temporal variations of the magnetic field from SDO/HMI observations. We model the well-established leading sunspot of active region NOAA 11072 (observed by SDO/HMI at 2010.05.25 03:00:00 TAI) with the semi-empirical sunspot model by Cameron et al. (2011) with added uniform twist. We study the spatial covariance of the magnetic field's temporal fluctuations and create a model based on our findings. We test the robustness of methods to measure twist by using Monte-Carlo simulations of the sunspot and fluctuation model.

In section 3.3 we present vector magnetic field observations of the reference sunspot in active region NOAA 11072. Section 3.4 and section 3.5 describe the fluctuation and sunspot model, respectively. In section 3.6 we present a summary of the twist measurement methods and their implementation, that we test in this paper. We then qualitatively compare our sunspot model to the SDO/HMI observations of the reference sunspot in section 3.7. In section 3.8 we present Monte-Carlo simulations to test how the twist measurement methods fare under the influence of temporally fluctuating magnetic field.

3.3 SDO/HMI vector magnetogram observations of our reference sunspot in active region NOAA 11072

In this section, we present a sunspot observed by SDO/HMI that we selected as a reference for our sunspot model. The reference sunspot should closely resemble the assumption that its magnetic field structure could be described as a monolithic uniformly twisted flux tube. Therefore, we looked for sunspots that are well established, roughly circular and with little influence of other strong magnetic field in its vicinity. We model the sunspot with uniform twist to test various methods to measure the twist under temporal fluctuations of the magnetic field.

We chose the leading sunspot of active region NOAA 11072 (2010.05.25 03:00:00 TAI), which was located about 30° away from disc center at the Stonyhurst heliographic coordinates 27° East and 13° South. Fig. 3.1 shows the Postel-projected sunspot transformed to local cylindrical coordinates from SDO/HMI vector magnetogram observations (hmi.b_720s, Hoeksema et al. 2014). B_z is the component normal to the surface. B_r and B_θ are located in a plane parallel to the surface. B_r points radially away from the spot's center and B_θ is always perpendicular to B_r. For a detailed description of the coordinate systems and transformations used, see appendix 3.10.1.

The sunspots we considered have a dominant radial B_r and weak azimuthal B_θ component, as shown for the example of the reference sunspot in Fig. 3.2. This is a known characteristic of sunspots (Borrero and Ichimoto 2011). We noticed that the azimuthal component, which carries the information about the handedness of the twist in a uniformly twisted flux tube, shows that the sunspot has regions with opposite sign of twist.

3.4 Estimating the spatial covariance of magnetic field fluctuations from the observations

We aimed to derive a model for the temporal fluctuations of the magnetic field in SDO/HMI vector magnetogram observations. To do so, we used an approximately seven hour time series of our reference spot (2010.05.25, 03:00:00 - 9:48:00 TAI) to look at each local Cartesian vector component (B_x, B_y, B_z) in Postel-projected maps individually. The observations have a cadence of 12 minutes. B_z is the vector component normal to the surface, B_x and B_y point from solar east to west and south to north, respectively. The time frame was chosen so that the spot is stable.

We tracked the proper motion of the sunspot by first calculating the flux-weighted centroid of $|B_z|$ within the sunspot in each observation. We defined the area for this calculation based on pixels with a value below 0.85 in normalized continuum maps of the sunspot. We found that the sunspot moved approximately three pixels over this time period almost linearly. We fit a line to the location of the centroid in the x- and y- direction, and used the fit to shift the centroids of each image to the same location.

We then detrended the time-series of each pixel by fitting a third order polynomial to the data and keeping the residuals (sketched in Fig. 3.3) to remove any long-term trends. We calculated the spatial correlation of these detrended time series using the Pearson correlation coefficent. Fig. 3.4 shows for each vector magnetic field component the average

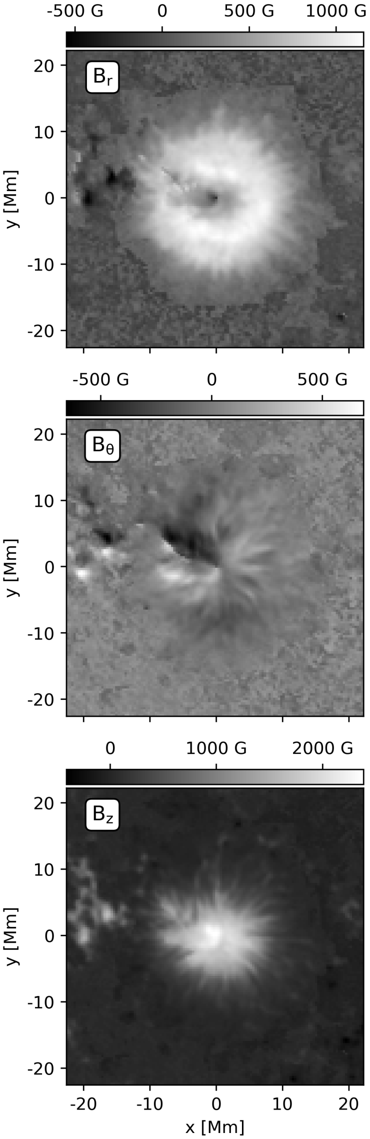

Figure 3.1: SDO/HMI vector magnetogram of active region active region NOAA 11072's leading sunspot (2010.05.25 03:00:00 TAI) in cylindrical coordinates. B_r (top), B_θ (mid) and B_z (bottom) show the radial, azimuthal and vertical component of the magnetic field.

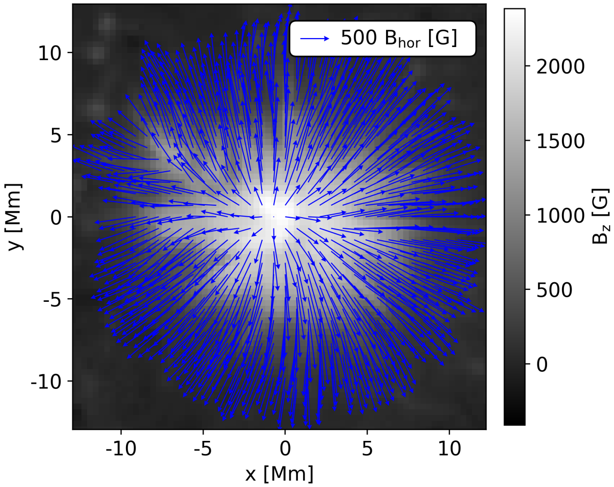

Figure 3.2: SDO/HMI vector magnetogram of active region NOAA 11072's leading sunspot (2010.05.25 03:00:00 TAI) with the horizontal field B_{hor} plotted as arrows on top of the vertical vector component B_z.

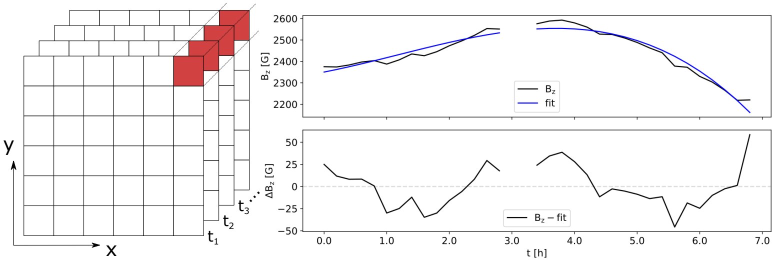

Figure 3.3: Sketch of the detrending process. A series of consecutive vector magnetograms (for example the B_z component), labeled with different time steps (t_1, t_2, t_3,...), is shown on the left. The black line (data) in the top right panel represents the temporal evolution of one pixel in this time series (marked in red in the left panel). The blue line is a third-order polynomial fit to the data. The bottom right panel displays the detrended time series, which shows the residuals of the data with respect to the fit.

correlation within the sunspot of a pixel relative to its neighbors. We find that, on average, pixels in the observations are correlated with their neighbors up to 3-4 pixels away.

In Appendix 3.10.2, we considered whether the observed correlations were due to the Postel projection, the detrending method, HMI's 12 and 24 hour periodicity caused by the satellites changing radial velocity relative to the Sun (Hoeksema et al. 2014) or HMI's point spread function. We concluded that these correlations are caused by HMI's point spread function and the dynamic changes of the magnetic field over time.

We incorporated the information about these time variations of the magnetic field in our model. Knowing that adjacent pixels are correlated but the strength of correlation depends on their position within the spot, we calculated the covariance matrix for all detrended time series and for each vector component individually. We used the Cholesky decomposition (Haddad 2009) of these covariance matrices to create random correlated maps that reflect spatially correlated temporal fluctuations of the magnetic field. Fig. 3.5 shows example realizations of such maps for each vector component.

3.5 A model for the reference sunspot

In this section we present the semi-empirical sunspot model developed by (Cameron et al. 2011) modified to represent a uniformly twisted field structure.

Cameron et al. (2011) describes a three-dimensional magnetic field model of an axisymmetric sunspot with a radial B_r and vertical B_z component. It lacks the azimuthal component B_θ, which is essential for creating twist. We added a B_θ component that is only dependant on the radius without violating the requirement of $\nabla \cdot \mathbf{B} = 0$ in 3D space. We were only interested in the magnetic field structure on the photospheric level (z = 0) to model a sunspot observed by SDO/HMI. Specifically, the magnetic field at the photosphere is

$$\begin{aligned} B_z(r) &= B_0 \exp\left[-(\log_e 2)\left(\frac{r}{h_0}\right)^2\right], && (3.2)\\ B_r(r) &= \frac{rB_z(r)}{8a_0\sqrt{1+b^2}}, && (3.3)\\ B_\theta(r) &= bB_r(r), && (3.4) \end{aligned}$$

where B_0 is the magnetic field strength at the spot's center, r is the distance from the spot's center and h_0 defines the radius of the umbra-/penumbra boundary. The parameter a_0 controls the inclination of the field and b governs the amount of twist in the model. Cameron et al. (2011)'s model is designed so that the inclination of the magnetic field at the umbra/penumbra boundary is 45 degrees. Due to the additional azimuthal component B_θ and to keep the same inclination profile we adjusted the parameter controlling the inclination a_0 in accordance with the injected twist by multiplying it with $\sqrt{1+b^2}$.
The pixel scale of our model is the same as HMI's pixel scale of 0.5", which corresponds to approximately 0.35 Mm at disc center. We fit the 4 free parameters (B_0, h_0, a_0, b) to the reference spot. We use a least-squares fitting approach to best match the azimuthal averages of B_z, B_r and B_θ around the reference sunspots's flux-weighted center of $|B_z|$.

The information about the spot's twist is stored in B_θ. As shown in Fig. 3.1 and Fig. 3.2, B_θ does not show an symmetric behaviour about the spot's center and azimuthal

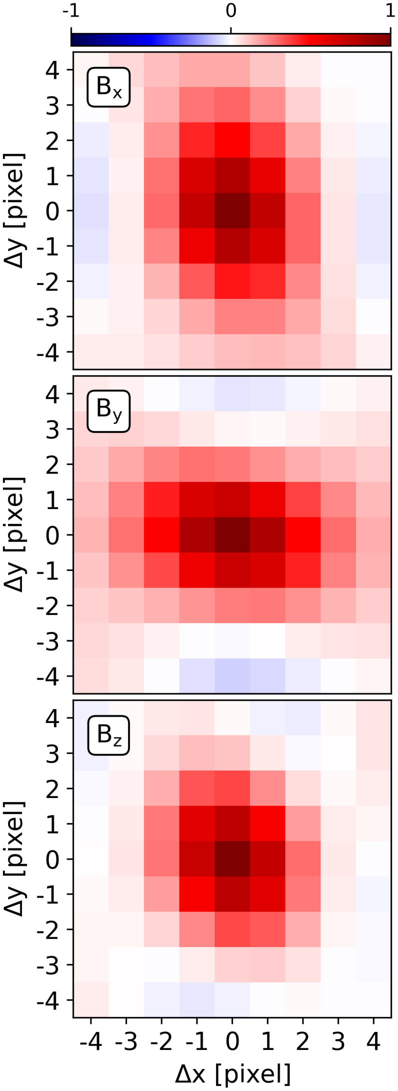

Figure 3.4: Average spatial correlation of the detrended time series of a pixel within the leading sunspot of active region NOAA 11072 (2010.05.25 03:00:00- 2010.05.25 9:38:00 TAI) relative to its neighbors for the magnetic field vector components B_x, B_y and B_z.

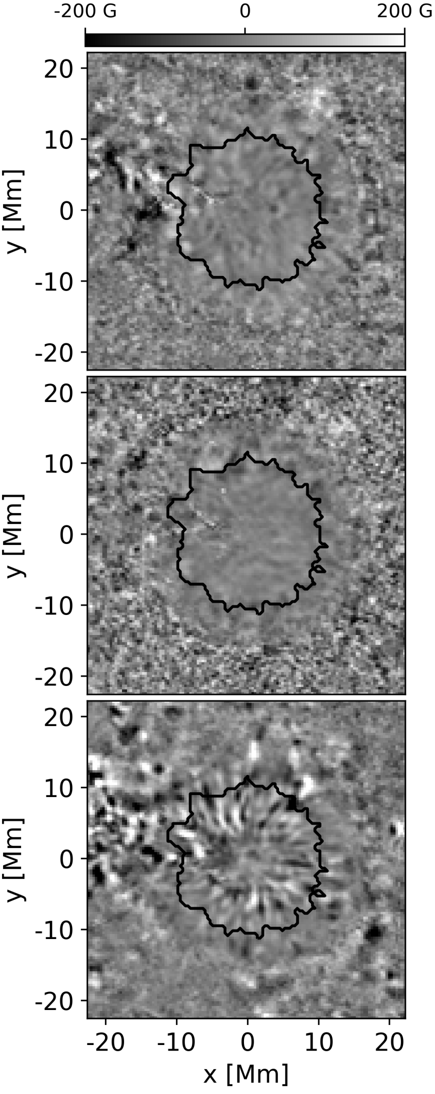

Figure 3.5: Each panel represents one realization of magnetic field fluctuations for each vector component. All panels are plotted on the same scale in units of Gauss displayed by the colorbar on top. The black solid line represents the observed sunspot boundary.

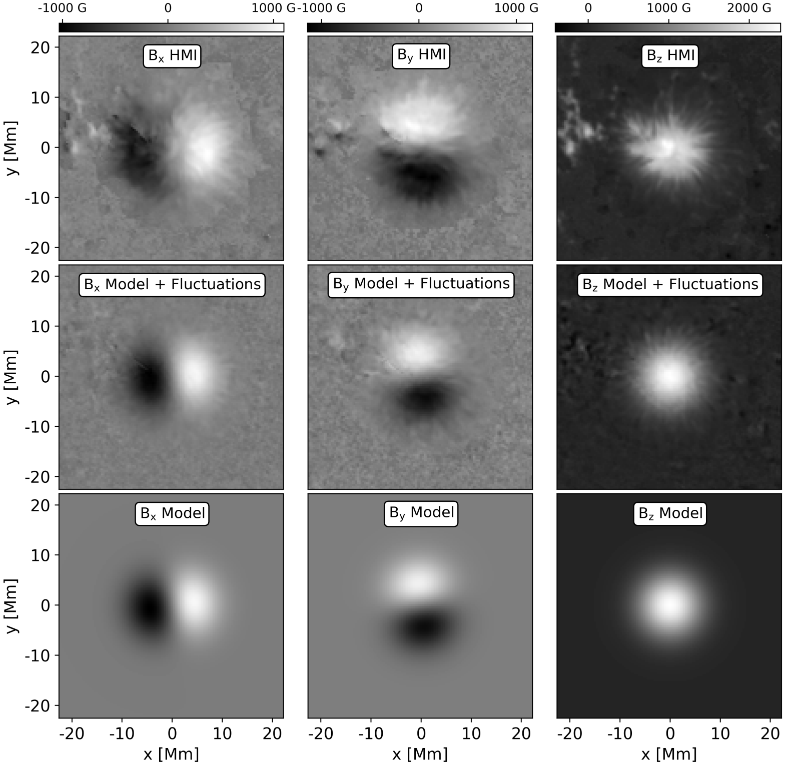

Figure 3.6: The three columns show a comparison of the magnetic field's vector components (B_x, B_y, B_z). The first row shows the HMI observation of active region NOAA 11072's leading sunspot (2010.05.25 03:00:00 TAI), which serves as the reference for our sunspot model. The second and third rows display the model with and without temporal fluctuations, respectively. Every column is plotted on the same scale in units of Gauss displayed by the colorbar on top of the column.

averages don't represent the local twist present in the observation. We found that fitting only the positive or negative values of B_θ yields values of 0.125 and -0.175 for the parameter b, respectively. Since the magnetic field twist of the reference sunspot has a preference to be negative, we chose $b = -0.15$.

The parameters that we found to best describe the reference sunspot with uniform twist are $B_0 = 2370$ G, $h_0 = 5.2$ Mm, $a_0 = 0.77$ Mm, $b = -0.15$.

3.6 Summary and implementation of twist measurement methods

Now we present various methods proposed in the literature to estimate the twist density directly from a single photospheric observations and describe their numerical implementation.

3.6.1 The twist proxy α

The force-free parameter α can serve as a helicity proxy (Pevtsov et al. 2014) to estimate the twist in uniformly twisted flux tubes (see appendix 3.10.6 for an interpretation of α in terms of twist). We lack information in photospheric observations how the B_x and B_y components of the magnetic field change as a function of height (z-direction in a local Cartesian coordinate system) and we can only compute the vertical current density J_z (e.g. Pevtsov et al. 1994, Longcope et al. 1998).

This vertical current density can be calculated from the force-free equation,

$$\nabla \times \mathbf{B} = \mathbf{J} = \alpha \mathbf{B}, \tag{3.5}$$

with

$$J_z = \frac{\partial B_y}{\partial x} - \frac{\partial B_x}{\partial y}. \tag{3.6}$$

Consequently we can compute the local twist proxy α_z at a specific location with

$$\alpha_z = \frac{J_z}{B_z}. \tag{3.7}$$

Note that α is a pseudo-scalar and the subscript z denotes that it was derived only from the vertical field component and vertical current density. Positive (negative) values of α_z correspond to right-handed (left-handed) magnetic field twist, respectively.

Numerically, we calculated the derivatives by using Savitzky-Golay filter (Savitzky and Golay 1964, appendix 3.10.3) of cubic/quartic order and a stencil size of five pixels. Note that J_z can also be calculated in integral form by using Stokes' theorem (see appendix 3.10.4). The stencil size was chosen based on our own tests on how the stencil size impacts spacial averages of α_z (see appendix 3.10.5) and the results by Fursyak (2018).

3.6.2 Average twist

Pevtsov et al. (1995) used a single best fit value of α from linear force-free field extrapolations to characterize the twist for whole active regions. Longcope et al. (1998) used an average $\langle \alpha_z \rangle$ for entire active regions, which can be calculated from photospheric observations without the need of any extrapolations:

$$\alpha_{\mathrm{av}} = \langle \alpha_z \rangle = \left\langle \frac{J_z}{B_z} \right\rangle. \tag{3.8}$$

Hagino and Sakurai (2004) proposed two weighted averages of α_z over a whole active region or spot to determine its twist:

$$\alpha_{\rm av}^{\rm abs} = \frac{\sum J_z \, {\rm sign}\,[B_z]}{\sum |B_z|} \tag{3.9}$$

and

$$\alpha_{\rm av}^{\rm sqr} = \frac{\sum J_z \, B_z}{\sum B_z^2}. \tag{3.10}$$

$\alpha_{\rm av}^{\rm abs}$ and $\alpha_{\rm av}^{\rm sqr}$ are weighted by absolute and squared B_z, respectively, which is represented by the superscripts "abs" and "sqr". They argue that these weighted averages have the advantage of putting less weight on weak field, especially close to the polarity inversion line, where singularities of α_z are more likely to occur.

The area over which α_z is averaged depends on the area of interest that is studied. In section 3.8 we will investigate averages over a small central area of the spot, the umbra and the whole spot.

3.6.3 Peak twist

Under the assumption that a spot can be approximated by a monolithic uniformly twisted magnetic flux tube, Leka et al. (2005) show that the α_z profile of this field structure has a peak directly at the spot's center (flux tube axis), which they name $\alpha_{\rm Peak}$. Based on the flux tube model by Gold and Hoyle (1960) they demonstrate that $\alpha_{\rm Peak}$ directly relates to the constant twist density q of the field's structure ($\alpha_{\rm Peak} = 2q$).

In order to calculate $\alpha_{\rm Peak}$ for a single sunspot, we estimated the location of the flux tube axis by computing the spot's flux weighted center of $|B_z|$. We calculated a map of α_z values (Eq. 3.7) for each pixel within the spot and boxcar-smoothed this map to 2" as suggested by Leka et al. (2005). We used the absolute values of this smoothed map to detect the α_z-peak closest to the estimated flux tube axis. $\alpha_{\rm Peak}$ is then the signed and smoothed α_z value at the peak's location.

3.6.4 Twist density

Nandy et al. (2008) proposed to fit the twist density q to quantify the magnetic twist in a single spot. Again, under the assumption that the magnetic field in a sunspot resembles a uniformly twisted flux tube, q can be measured by fitting the slope of the equation

$$\frac{B_\theta}{B_z} = qr + d, \tag{3.11}$$

where r is the distance from the flux tube axis. B_θ and B_z are the magnetic field in azimuthal direction and along the tube's axis, respectively. The tube's axis is estimated by calculating the flux-weighted center of $|B_z|$ of the sunspot. Note that Nandy et al. (2008) allowed a non-zero intercept d to occur in their Fig. 2. This violates the assumption of a vertical uniformly twisted flux tube, where the fitted function is expected to go through zero at $r = 0$, which is equivalent to a vanishing B_θ at the flux tube's axis. A physical interpretation of this intercept is not clear to us.

This method was carried out in a cylindrical coordinate system (B_r, B_θ, B_z, see appendix 3.10.1). We fit the ratio B_θ over B_z for each pixel as a function of the pixel's distance from the estimated flux tube axis r. The resulting slope corresponds to the twist density q. We tested this method by both allowing an intercept and by forcing the fit through the origin (d=0).

3.7 Example sunspot model with correlated magnetic field fluctuations compared to HMI observations

In this section we qualitatively compare the magnetic field and its twist between our sunspot model with one realization of magnetic field fluctuations and the SDO/HMI observations of the reference sunspot in active region NOAA 11072.

3.7.1 The vector magnetic field

Fig. 3.6 shows that visually the model spot with correlated magnetic field fluctuations resembles the HMI observation of active region NOAA 11072's leading sunspot (2010.05.25 03:00:00). It even exhibits a filamentary structure especially noticeable in B_z, which is not present in the model without fluctuations of the magnetic field. The fluctuation maps (Fig. 3.5) have smoother and weaker fluctuations within the sunspot, and stronger, more chaotic fluctuations in the quiet Sun, as one would expect from the observations.

3.7.2 The magnetic field's twist

Fig. 3.7 compares α_z-profiles of the original SDO/HMI observation of the reference sunspot and our model with and without one realization of temporal fluctuations of the magnetic field.

Our sunspot model without fluctuations describes a uniformly left-handedly twisted magnetic field structure. The α_z-profile is azimuthally symmetric and α_z increases with distance from the spots centers. The sign of α_z changes in the penumbra, which signals the presence of return currents (see appendix 3.10.6).

The reference sunspot has a more complicated structure than the model without temporal fluctuations. Even in the center of the spot areas of opposite sign of α_z exist. Towards the penumbra positive values of α_z become more frequent and one could assume a ring of return currents similar to the model. After applying magnetic field fluctuations to the model, a similar structure of the α_z pattern compared to the observations develops.

Our definition of fluctuations include the dynamic variations of the magnetic field. Correlated changes in the magnetic field's direction of adjacent pixels can produce spatially coherent changes in twist and its sign in our model. Sunspot observations show typically a strong radial field component and exhibit only weak twist (i.e. a weak azimuthal field component, $B_\theta << B_r$). A source of fluctuations of the magnetic field is the forced-environment of the photosphere, where the magnetic field can be buffeted by plasma flows, which can cause sign changes of the real twist. Such an effect is expected to be stronger where the magnetic field strength is weaker, i.e. the penumbral parts of the sunspot, where we see the strongest variations of α_z within sunspots. Also interactions

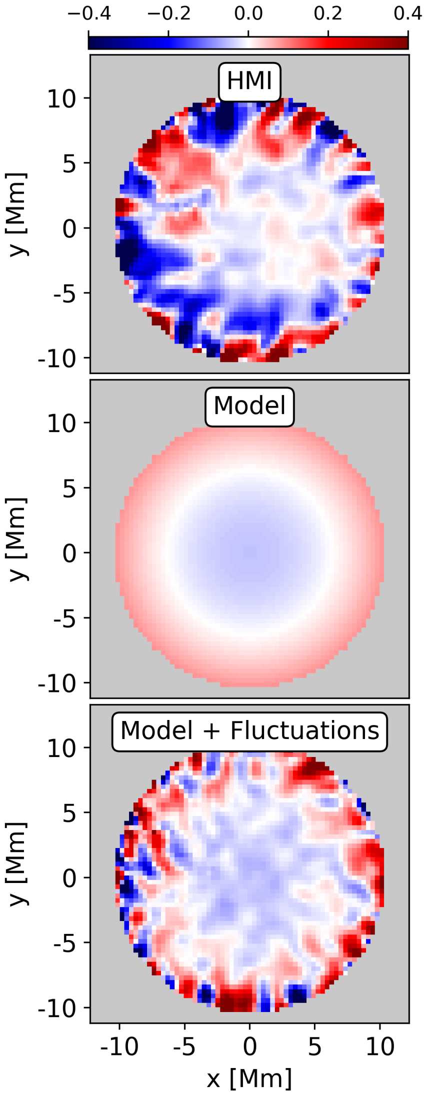

Figure 3.7: Comparison of α_z maps measured from the original HMI observation (top), the model without (middle) and with fluctuations of the magnetic field (bottom). The colorbar on top shows the α_z values in Mm^{-1}.

with magnetic flux surrounding a sunspot could cause deviations from a uniformly twisted field structure. Complex patterns of α_z and magnetic field twist even within the umbra of sunspots have been described in literature (e.g. Pevtsov et al. 1994, Socas-Navarro 2005, Su et al. 2009).

Fig. 3.8 and Fig. 3.9 show the temporal evolution of α_z and its sign for the leading sunspot of active region NOAA 11072, respectively. In Fig. 3.8 we find that in most parts of the umbra α_z is in the order of 10^{-2} Mm^{-1}, while penumbral α_z values are typically at least one order of magnitude larger consistent with other α_z-measurements in sunspots (e.g. Tiwari et al. 2009a, Wang et al. 2021).

We find patches of α_z with opposite signs throughout the reference sunspot, consistent with previous studies of sunspots (e.g. Pevtsov et al. 1994, Socas-Navarro 2005, Su et al. 2009). The shape of these patches are in agreement with findings by Su et al. (2009), who describe a mesh like pattern in the umbra and a thread like pattern in the penumbra. Fig. 3.9 shows that many of these patches persist over timescales of hours.

We find a similar distribution of α_z values and patterns in the sunspot model with a realization of magnetic field fluctuations. The uncertainty of the mean α_z (standard deviation of α_z divided by the number of pixels considered) within the model sunspot with fluctuations is of the order of 10^{-3} Mm^{-1}. This is the same order of uncertainty that Leka and Skumanich (1999) and Leka (1999) measured in active regions observed with the Image Vector Magnetograph at Mees Solar Observatory.

Features in the pattern structure appear to be on a smaller scale in our model. Pevtsov et al. (1994) studied the magnetic field's helical structure of three active regions and estimate that the lifetime of such patches can exceed a day. Our model only describes the spatial correlation of magnetic field fluctuations but does not address their temporal correlation. Therefore, these patches appear uncorrelated from one realization to the other. Whether the temporal variations of the magnetic field are responsible for the twist and current patterns that we can observe in real sunspots, can not be said from our model yet. To further investigate this question, one has also to consider the temporal correlation of the magnetic fluctuations.

3.8 Sensitivity of twist measurements to correlated temporal fluctuations of the magnetic field

We used Monte-Carlo simulations to test the sensitivity of twist measurement methods described in section 3.6 to fluctuations of the magnetic field. We used our magnetic field fluctuation model (described in section 3.4) in 10,000 realisations to create different fluctuation maps and superimposed them on the sunspot model (section 3.5). We evaluated in each iteration the different twist proxies in the umbra (up to $r = h_0$). We also tested the robustness of the twist measurement methods based on the area they are averaged over. We evaluated α_{av} in a small umbral area with a radius of 1.75 Mm from the spot's center ($\alpha_{\mathrm{av}}^{\mathrm{center}}$, white circle in Fig. 3.10) and up to the penumbra/quiet Sun boundary ($\alpha_{\mathrm{av}}^{\mathrm{spot}}$, black dotted circle in Fig. 3.10, up to $r = 2h_0$). Fluctuations of the magnetic field in our model can result in vertical field B_z close to zero in the penumbra, which can create singularities when calculating $\alpha_z = J_z/B_z$. Therefore, we only measure α_z for pixels that are above a B_z threshold of 50 Gauss.

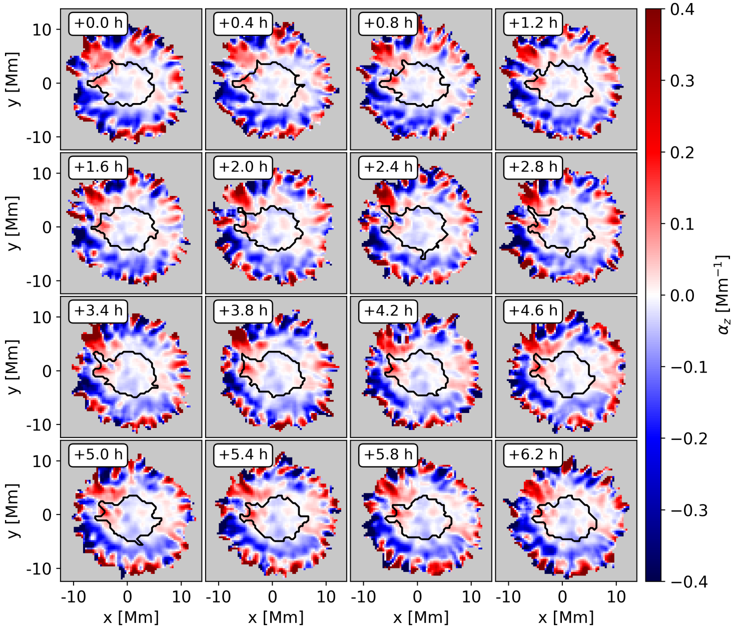

Figure 3.8: The temporal evolution of α_z in the leading sunspot of active region NOAA 11072. The time relative to the first observation (2010.05.25 03:00:00 TAI) is shown in hours in the top left of each panel. The black solid line represents the umbra-penumbra boundary.

The analytically calculated reference values of α_z and q that represent the uniform twist of our model best (see Appendix 3.10.6) are $\alpha_{\mathrm{Peak}}^{\mathrm{ref}} = 2q \approx -0.048\ \mathrm{Mm}^{-1}$.
Fig. 3.11 and Fig. 3.12 show the distribution of the calculated twist proxies from the Monte-Carlo simulations for each method. Tab. 3.1 compares the mean result and standard deviation from the Monte-Carlo simulations against the expected value from the model without fluctuations. It is important to note that the "Model" values in Tab. 3.1 are derived when a method is applied in the fluctuation-free model. The errors given in Tab. 3.1 show the standard deviation of the Monte-Carlo simulations. We find that the expectation values of the averaging methods and the twist density fits are not biased by magnetic field fluctuations.

The averaging methods of α_z show a big spread in their results, but have robust measurements under magnetic field fluctuations. These different spatial averages of α_z can still be related to the twist density based on the azimuthal symmertric behavior of α_z in our simple model. We derive $\alpha_z(r) = 2q\left[1 - (\log_e 2)\left(\frac{r}{h_0}\right)^2\right]$ in appendix 3.10.6. We can

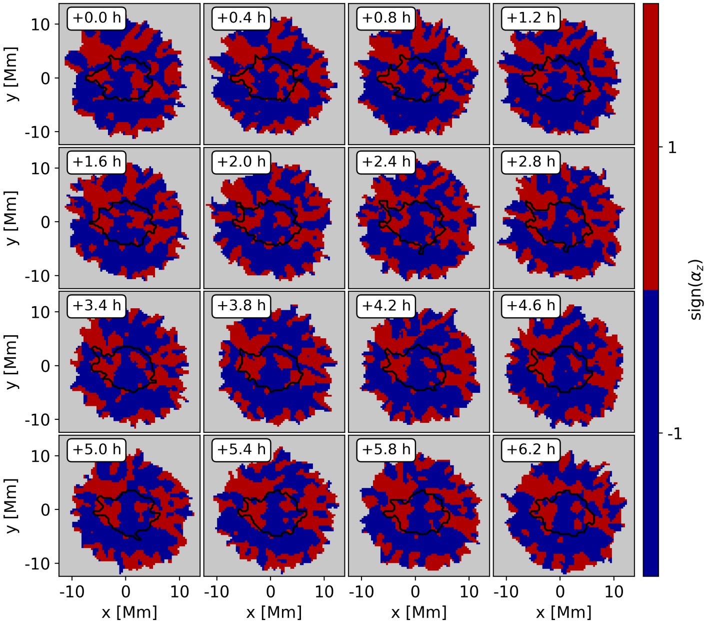

Figure 3.9: The temporal evolution of the sign of α_z in the leading sunspot of active region NOAA 11072. The time relative to the first observation (2010.05.25 03:00:00 TAI) is shown in hours in the top left of each panel. The black solid line represents the umbra-penumbra boundary.

calculate the average value of α_z in a circular area with radius r around the spot's center

$$\langle\alpha_z\rangle_r = \frac{1}{\pi r^2}\int_0^r\int_0^{2\pi}\alpha_z(\tilde{r})\,\tilde{r}d\tilde{r}d\theta = \left[2-(\log_e 2)\left(\frac{r}{h_0}\right)^2\right]q. \tag{3.12}$$

Consequently, we find the following relation between the twist density q and $\langle\alpha_z\rangle_r$

$$q = \frac{\langle\alpha_z\rangle_r}{2-(\log_e 2)\,(r/h_0)^2}. \tag{3.13}$$

This equation is consistent with the relation of $\alpha_{Peak} = 2q$ at the center of the spot. It also describes the different spatial averages of α_z that we measure, when the averaging radius was changed (see Fig. 3.11 and Fig. 3.12). We measure a larger $\langle\alpha_z\rangle$ when averaged over a small area at the spot's center ($\alpha_{\rm av}^{\rm center}$) compared to the average over the umbra ($\alpha_{\rm av}$). When the averaging radius becomes sufficiently large enough (e.g. $\alpha_{\rm av}^{\rm spot}$), $\langle\alpha_z\rangle$ retrieves the opposite sign compared to α_z in the center of the spot.

The expectation value of the $\alpha_{\rm Peak}$ method is noticeably biased to overestimate the twist density. Since this method characterizes the twist density with a single peak value

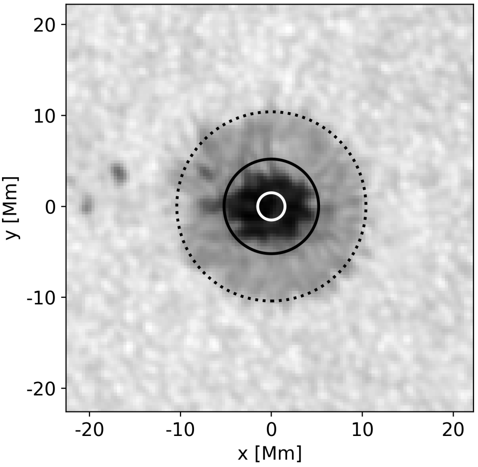

Figure 3.10: HMI continuum image of the leading sunspot of active region NOAA 11072 (2010.05.25 03:00:00 TAI), which was used as a reference for the model presented in this work. The black solid line outlines the umbral area that was considered for most twist calculation methods. The white solid line and the black dotted line correspond to the areas, that were used to get spatial averages of α_z close to the spot's center ($\alpha_{\mathrm{av}}^{\mathrm{center}}$) and over the whole spot ($\alpha_{\mathrm{av}}^{\mathrm{spot}}$), respectively.

closest to the spot's center, it is likely to pick up any enhanced signal caused by the fluctuations of the magnetic field.

The twist density fit (Nandy et al. 2008) fit retrieves the analytical twist density value. We find a larger spread in the resulting values when no zero-intercept is forced. These are expected results, since our sunspots model's equations can be exactly reduced to the fitting equation by Nandy et al. (2008). Crouch (2012) shows that fitting techniques can be sensitive to small discrepancies between the fitting and reference model. Observations suggest that sunspots are more complicated and can have a non-uniformly twisted field structures (e.g. Socas-Navarro 2005, Su et al. 2009). Another complication for real sunspots is, that this method requires to be perfectly able to locate the flux tube axis as a center for the coordinate transformation to cylindrical coordinates. This is a simple task in our model without fluctuations, since the model spot's central axis and flux weighted center fall into the same place by definition. Even with magnetic field fluctuations, they are always located close to each other. In real sunspots the axis of the spot does not have to be in the same place as its flux weighted center. And, of course, a sunspot may not have an underlying uniformly twisted vertical field structure.

In section 3.5 we chose the model parameter $b = -0.15$, which governs the twist in our model. We tested various values of b, ranging from untwisted field ($b = 0$) to highly twisted field ($b = 10$) and found that the amount of twist in the model does not influence the findings about the robustness of the twist measurements described in this section.

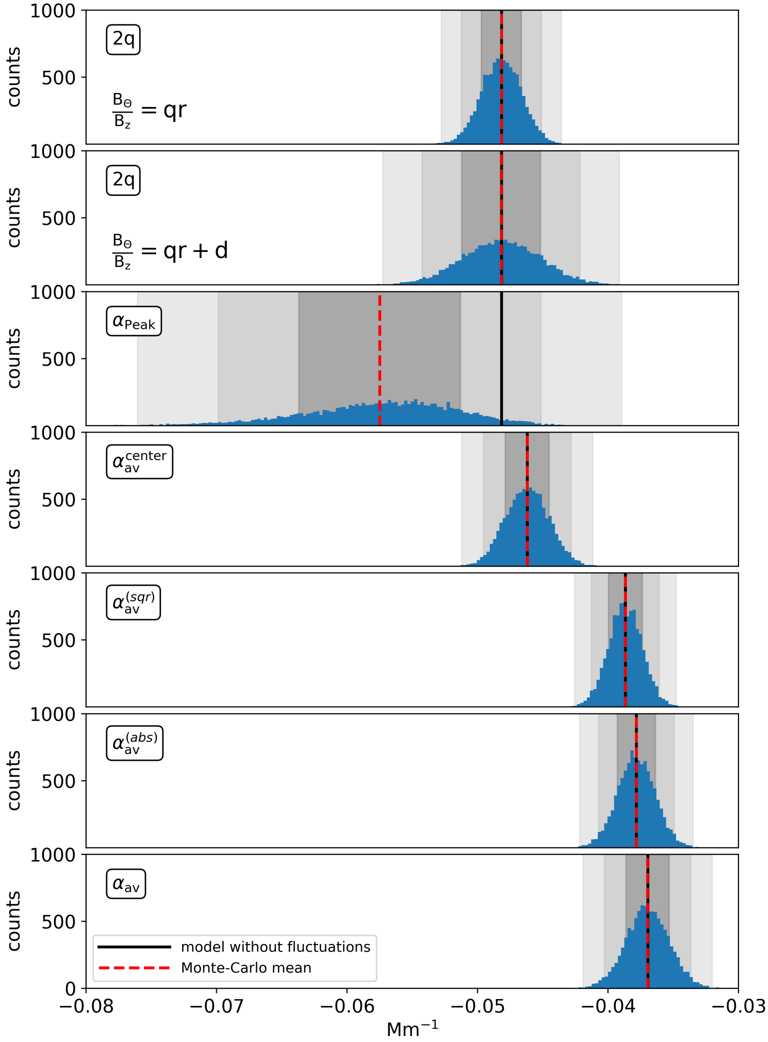

Figure 3.11: Monte-Carlo simulation results for methods described in section 3.6. The q values have been multiplied by two, to make them directly comparable to α_z (see appendix 3.10.6). The black line indicates the model's reference value, that is expected from the model without any fluctuations. The red dashed line shows the mean value from the Monte-Carlo simulations. The gray shaded areas represent the range of 1, 2 and 3 σ around the Monte-Carlo mean.

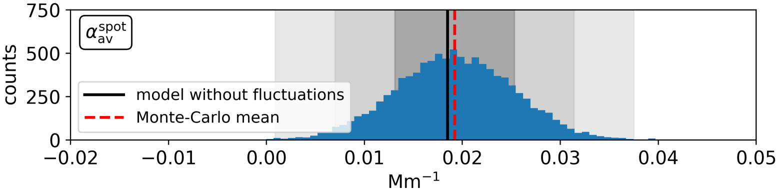

Figure 3.12: Monte-Carlo simulation results when α_z is spatially averaged over the whole sunspot. The solid black line indicates the model's reference value, that is expected from the model without any fluctuations. The red dashed line shows the mean value from the Monte-Carlo simulations. The gray shaded areas represent the range of 1, 2 and 3 σ around the mean.

Table 3.1: Comparison of the different twist calculation methods between the model reference without any fluctuations of the magnetic field (Model) and the Monte-Carlo simulations (MC Sim.). All values are given in Mm^{-1}.

Method	Model	MC Sim.
$2q\ \left(\frac{B_\Theta}{B_z} = qr\right)$	−0.048	−0.048 ± 0.002
$2q\ \left(\frac{B_\Theta}{B_z} = qr + d\right)$	−0.048	−0.048 ± 0.003
α_{Peak}	−0.048	−0.058 ± 0.006
$\alpha_{\mathrm{av}}^{\mathrm{center}}$	−0.046	−0.046 ± 0.002
$\alpha_{\mathrm{av}}^{\mathrm{sqr}}$	−0.039	−0.039 ± 0.001
$\alpha_{\mathrm{av}}^{\mathrm{abs}}$	−0.038	−0.038 ± 0.001
α_{av}	−0.037	−0.037 ± 0.001
$\alpha_{\mathrm{av}}^{\mathrm{spot}}$	0.019	0.019 ± 0.006

3.9 Summary and Conclusion

We derived a model for the spatially correlated fluctuations of the magnetic field in a sunspot based on HMI observations of active region NOAA's 11072 leading sunspot. We superposed realizations of the fluctuations on the magnetic field of the semi-empirical sunspot model described in Cameron et al. (2011) with added uniform twist. We carried out Monte-Carlo simulations to test the robustness of the different measures of the twist to the fluctuations.

We considered measurement methods based either on estimating the force-free parameter α_z or the magnetic field's twist density q. In the absence of fluctuations, and for the sunspot model used in this paper, the value of α_z at the center of the sunspot is twice the twist parameter q (see Leka et al. 2005). For our chosen twist profile, α_z is not uniform and changes sign in the penumbra of the model spot.

Including the spatially correlated temporal fluctuations of the magnetic field qualitatively reproduces features seen in vertical current density J_z and α_z observations. Patches with opposite sign of α_z appear throughout the sunspot model at random locations from one realization to another. Although we do not consider temporal correlations of the fluctuations, we note that such features can persist for hours in observations (Pevtsov et al.

1994).

All measures except α_{Peak} have expectation values consistent with that of the model without fluctuations. The fluctuations do not introduce a bias. The measures based on spatial averages of α_z have different expectation values, because they average over different portions of the non-uniform α_z profile. Due to the sign change of α_z in the penumbra of our model, any spatial averages of α_z that reach too far out from the spot's center can have the opposite sign from α_z near the center of the spot. The expectation value of α_{Peak} is biased with respect to the model without fluctuations. The magnitude of the bias is related to the level of the magnetic field fluctuations.

For most methods, the spread of results from the Monte-Carlo simulations is less than the spread in expectation values of the individual methods. Therefore, the choice of method is more significant than the impact of the magnetic field fluctuations on the measurements.

Our results are for the particular sunspot model given by Eqns. 3.2-3.4. This is a particularly simple, axisymmetric, sunspot model. For sunspots with a more complex structure, for example non-uniformly twisted sunspots, the applicability and meaning of the different measures needs to be carefully considered (e.g. Crouch 2012). In this regard we note that the SDO/HMI observations of the leading spot of active region NOAA 11072 had fine structure in α_z which persisted for longer than 7 hours. This persistent fine structure suggests a more complicated underlying field structure than that of our uniformly twisted model. The long-lived fine structure found in AR 11072 is consistent with previous studies of other sunspots (e.g. Pevtsov et al. 1994, Su et al. 2009).

As was previously noted by Leka (1999), a single parameter will not in general characterize a sunspot's twist. In this paper we have shown that there exist a range of different, complementary, parameters which all describe somewhat different aspects of the magnetic field line twist in sunspots. We have shown that most of these measures are robust to fluctuations of the field.

Acknowledgements

CB is a member of the International Max Planck Research School (IMPRS) for Solar System Science at the University of Göttingen. CB conducted the analysis, contributed to the interpretation of the results, and wrote the manuscript. We thank Jesper Schou for helpful discussions. We thank Graham Barnes for useful comments on the manuscript. The HMI data used are courtesy of NASA/SDO and the HMI Science Team. ACB, RHC and LG acknowledge partial support from the European Research Council Synergy Grant WHOLE SUN #810218. The data were processed at the German Data Center for SDO, funded by the German Aerospace Center under grant DLR50OL1701. This research made use of the Astropy (Astropy Collaboration et al. 2013, 2018), Matplotlib (Hunter 2007), NumPy (Van Der Walt et al. 2011) and SciPy (Virtanen et al. 2020) Python packages.

3.10 Appendix

3.10.1 Vector transformation

3.10.1.1 Local Cartesian Coordinates

The hmi.b_720s (Hoeksema et al. 2014) provides the vector magnetic field in spherical coordinates aligned with the line-of-sight (LoS). It includes the absolute field strength B, the inclination angle inc with respect to the LoS and the azimuth angle azi (whose ambiguity has to be resolved) measured in a plane perpendicular to the LoS. We study the magnetic field in a local Cartesian and cylindrical coordinate system, where B_z is pointing radially outwards from the Sun. In order to transform the spherical coordinate system to a local Cartesian coordinate system, we followed the transformations described in Gary and Hagyard (1990).

First the spherical vector components were transformed to a Cartesian system, where B_ζ is aligned with the LoS, while B_ξ and B_η lay in the plane perpendicular to the LoS:

$$B_\xi = -B\sin(\mathrm{inc})\sin(\mathrm{azi}) \tag{3.14}$$

$$B_\eta = B\sin(\mathrm{inc})\cos(\mathrm{azi}) \tag{3.15}$$

$$B_\zeta = B\cos(\mathrm{inc}). \tag{3.16}$$

Then we rotated the coordinate system (Eq. 3.17) so that B_ζ points radially outward from the Sun and becomes B_z. B_x and B_y point from solar east to west and south to north, respectively. The rotation matrix is

$$\begin{bmatrix} B_x \\ B_y \\ B_z \end{bmatrix} = \begin{bmatrix} a_{11} & a_{12} & a_{13} \\ a_{21} & a_{22} & a_{23} \\ a_{31} & a_{32} & a_{33} \end{bmatrix} \begin{bmatrix} B_\xi \\ B_\eta \\ B_\zeta \end{bmatrix} \tag{3.17}$$

with the transformation matrix coefficients a_{ij}

$$\begin{aligned}
a_{11} &= -\sin B_0 \sin P \sin(L-L_0) + \cos P \cos(L-L_0) \\
a_{12} &= +\sin B_0 \cos P \sin(L-L_0) + \sin P \cos(L-L_0) \\
a_{13} &= -\cos B_0 \sin(L-L_0) \\
a_{21} &= -\sin B\,[\sin B_0 \sin P \cos(L-L_0) + \cos P \sin(L-L_0)] - \\
&\qquad -\cos B\,[\cos B_0 \sin P] \\
a_{22} &= +\sin B\,[\sin B_0 \cos P \cos(L-L_0) - \sin P \sin(L-L_0)] + \\
a_{23} &= -\cos B_0 \sin B \cos(L-L_0) + \sin B_0 \cos B \\
a_{31} &= +\cos B\,[\sin B_0 \sin P \cos(L-L_0) + \cos P \sin(L-L_0)] - \\
&\qquad -\sin B\,[\cos B_0 \sin P] \\
&\qquad +\cos B\,[\cos B_0 \cos P] \\
a_{32} &= -\cos B\,[\sin B_0 \cos P \cos(L-L_0) + \sin P \sin(L-L_0)] + \\
&\qquad +\sin B\,[\cos B_0 \cos P] \\
a_{33} &= +\cos B \cos B_0 \cos(L-L_0) + \sin B \sin B_0.
\end{aligned}$$

L and B describe the heliographic longitude and latitude of the individual pixel, while L_0 and B_0 are the longitude and latitude of the solar disc's center, respectively. P is the solar position angle.

3.10.1.2 Cylindrical Coordinates

We transformed from the local Cartesian coordinate system to a local cylindrical coordinate system by calculating

$$\begin{bmatrix} B_r \\ B_\theta \\ B_z \end{bmatrix} = \begin{bmatrix} \cos\theta & \sin\theta & 0 \\ -\sin\theta & \cos\theta & 0 \\ 0 & 0 & 1 \end{bmatrix} \begin{bmatrix} B_x \\ B_y \\ B_z \end{bmatrix}, \tag{3.18}$$

with $\theta = \arctan 2(y, x)$. The flux-weighted center of a spot is defined as the origin ($x = 0, y = 0$) for this transformation. In this coordinate system B_z is the component normal to the surface. B_r and B_θ are located in a plane parallel to the surface. B_r points radially away from the spot's center and B_θ is always perpendicular to B_r and B_z.

3.10.2 Possible causes for the measured spatial correlation of magnetic field fluctuations

We tested various effects that could introduce the spatial correlation of temporal fluctuations of neighboring pixels. To assess the effect of the Postel projections on these correlations, we created artificial full-disk HMI maps. We filled pixels with random Gaussian white noise with a mean of zero and standard deviation of one. We created Postel-projected time series of submaps at different locations on the solar disk, based on the center to limb angle (CTL) of the submap's center. We followed the same detrending procedure as described in section 3.4, but we did not find any correlations of adjacent pixels neither at disk center (CTL = 0°) nor close to the limb (CTL = 60°).

We compared different ways of detrending the data: different order of polynomials for fitting (order 3, 4 and 5), differences to previous data points and running averages. All different detrending methods show similar correlations of adjacent pixels.

We found no relation of the detrended signals to the known 12 and 24 hours period systematics of HMI that are caused by the satellite's orbit and change in radial velocity relative to the Sun.

The point spread function (PSF) of HMI definitely contributes to the correlations of adjacent pixels. Fig. 3.13 shows an estimate of HMI's PSF by Yeo et al. (2014). Fig. 3.14 shows cuts along the x- and y-axis through the center of the normalized PSF and the average correlations of adjacent pixels shown in Fig. 3.4. We find that the fluctuations of the vector magnetic field components are correlated up to spatial scales 30% larger than that expected from the HMI point spread function.

We suggest that these correlations are caused by the PSF and the dynamic changes of the magnetic field over time with respect to its underlying global field structure of the sunspot.

3.10.3 Derivatives with different stencil sizes

We can evaluate derivatives with different stencil sizes by using Savitzky-Golay filter (Savitzky and Golay 1964) of cubic/quartic order for stencil sizes of 5 and 7 pixels or take

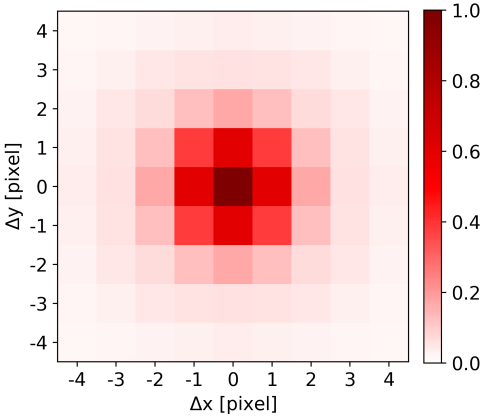

Figure 3.13: Normalized point spread function for HMI estimated by Yeo et al. (2014).

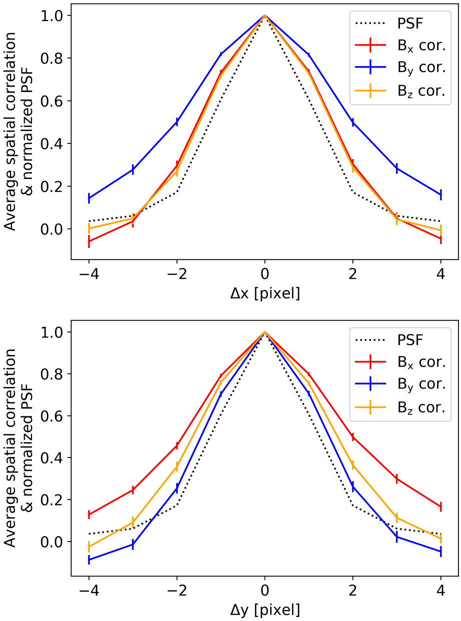

Figure 3.14: Cuts through the center along the x-axis (top panel) and the y-axis (bottom panel) of the average spatial correlation of neighboring pixels (Fig. 3.4) and the normalized estimated PSF by Yeo et al. (2014) (Fig. 3.13). The errorbars represent the standard error of the spatially averaged correlation.

Table 3.2: Weighting factors g(i) and normalization factors N for stencil sizes S of 7, 5 and 3 pixels for Eq. 3.19.

i	$g(i)$		
	$S = 7$	$S = 5$	$S = 3$
-3	22	0	0
-2	-67	1	0
-1	-58	-8	-1
0	0	0	0
1	58	8	1
2	67	-1	0
3	-22	0	0
N	252	12	2

a central differences approach for a stencil of 3 pixels:

$$\frac{\partial f(x)}{\partial x} = \frac{1}{Nh} \sum_{i=-(S-1)/2}^{(S-1)/2} g(i) f(x+i), \tag{3.19}$$

where x describes the location of a pixel counted as integer, for which we want to calculate the derivative. S is the stencil size, N is a normalization factor, h is the pixel scale and g is a weighting factor. The weighting and normalization factor for the different stencil sizes are listed in Tab. 3.2.

3.10.4 Using Stokes' theorem for calculating J_z

Instead of using derivatives for calculating J_z (Eq. 3.6), one can also use Stokes' theorem:

$$J_z^{\mathrm{Int.}} = \frac{1}{\mathrm{A_L}} \oint_L \mathbf{B}_{\mathrm{hor}} \cdot d\mathbf{L}, \tag{3.20}$$

where the vertical current density is calculated for a pixel in the center of an area A_L outlined by a contour L. We calculated the integral by using the composite Simpson's rule over a square, where L is the edge of the square with a side length of 3, 5 or 7 pixels, in accordance to the stencil size when using derivatives.

Using Stokes' theorem for calculating α_z leads on average to slightly lower values compared to the differential form. This effect can be attributed to the integral form using more pixels for the calculations and averaging over an area. The results of Monte-Carlo simulations are shown in Fig. 3.15 and Fig. 3.16 as well as Tab. 3.3.

3.10.5 Comparison of different stencil sizes for calculating J_z

We tested stencil sizes of 3, 5 and 7 pixels in Monte-Carlos simulations as described in section 3.8 to determined how many pixels should be considered for calculating the vertical current density J_z and subsequently α_z. The average twist proxy values and their standard deviation from these simulations are listed in Tab. 3.4 & 3.5. The different stencil sizes do not noticeably impact the end result when we used the Savitzky-Golay filter.

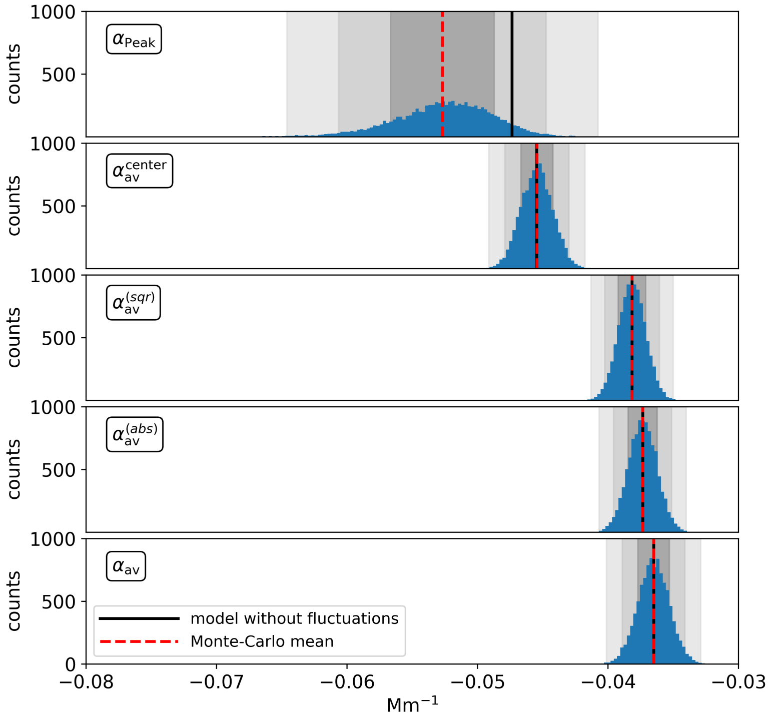

Figure 3.15: Monte-Carlo simulation results for methods based on α_z when Stokes' theorem is used for calculating J_z. The black solid line indicates the model's reference value, that is expected from the model without any fluctuations. The red dashed line shows the mean value from the Monte-Carlo simulations. The dark/light gray shaded areas represent the range of 1, 2 or 3 σ around the Monte-Carlo mean.

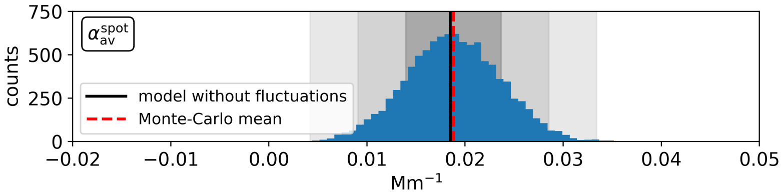

Figure 3.16: Monte-Carlo simulation results when α_z is calculated with Stokes' theorem and spatially averaged over the whole sunspot. The black solid line indicates the model's reference value, that is expected from the model without any fluctuations. The red dashed line shows the mean value from the Monte-Carlo simulations. The gray shaded areas represent the range of 1, 2 and 3 σ around the mean.

Table 3.3: Comparison of the different twist calculation methods between the model reference without any fluctuations of the magnetic field (Model) and the Monte-Carlo simulations (MC Sim.). All parameters were calculated by using Stokes' theorem. Values are given in Mm^{-1}.

Method	Model	MC Sim.
α_{Peak}	-0.047	-0.053 ± 0.004
$\alpha_{\mathrm{av}}^{\mathrm{center}}$	-0.046	-0.046 ± 0.001
$\alpha_{\mathrm{av}}^{\mathrm{sqr}}$	-0.038	-0.038 ± 0.001
$\alpha_{\mathrm{av}}^{\mathrm{abs}}$	-0.038	-0.038 ± 0.001
α_{av}	-0.037	-0.037 ± 0.001
$\alpha_{\mathrm{av}}^{\mathrm{spot}}$	0.018	0.019 ± 0.005

Table 3.4: Monte-Carlo simulation results for using derivatives to calculate α_z with stencil sizes of 3, 5 and 7 pixels, when α_z was evaluated in the model spot's umbra.

Dif	3	5	7
α_{Peak}	-0.058 ± 0.006	-0.058 ± 0.006	-0.058 ± 0.007
$\alpha_{\mathrm{av}}^{\mathrm{sqr}}$	-0.039 ± 0.001	-0.039 ± 0.001	-0.039 ± 0.001
$\alpha_{\mathrm{av}}^{\mathrm{abs}}$	-0.038 ± 0.001	-0.038 ± 0.001	-0.038 ± 0.001
α_{av}	-0.037 ± 0.001	-0.037 ± 0.001	-0.037 ± 0.001

In contrast, we find that with bigger areas the measured twist goes down when Stokes' theorem (see appendix 3.10.4) was applied. Similar to the Monte-Carlo simulations described in section 3.8 only the expectation value of the α_{Peak} method is biased in all test cases.

Fursyak (2018) tested the effect of differently sized areas for calculating J_z in differential and integral forms using observations from Hinode and HMI. They conclude that integrating over side lengths of five pixels provides the best compromise between smoothing noise but still preserving significant features.

Since the results from our tests do not show a clear favorite, we chose to calculate J_z with stencil sizes of 5 pixel in accordance to Fursyak (2018).

Table 3.5: Monte-Carlo simulation results for using integration to calculate α_z over square areas with side lengths of 3, 5 and 7 pixels, when α_z was evaluated in the model spot's umbra.

Int.	3	5	7
α_{Peak}	-0.057 ± 0.006	-0.053 ± 0.004	-0.050 ± 0.004
$\alpha_{\mathrm{av}}^{\mathrm{sqr}}$	-0.039 ± 0.001	-0.038 ± 0.001	-0.038 ± 0.001
$\alpha_{\mathrm{av}}^{\mathrm{abs}}$	-0.038 ± 0.001	-0.038 ± 0.001	-0.037 ± 0.001
α_{av}	-0.037 ± 0.001	-0.037 ± 0.001	-0.036 ± 0.001

3.10.6 Interpretation of α_z

It is often difficult to interpret α_z measurements. Ideally we would expect to measure the same α_z or twist density q value at each location within a uniformly twisted flux tube (which is the case in thin flux tube models). While this is true for the twist density q in our sunspot model without magnetic field fluctuations, α_z varies with the distance from the spot's center, where the α_z profile peaks.

Leka et al. (2005) used the Gold-Hoyle flux tube model (Gold and Hoyle 1960) to show the connection between α_z and the twist density. This model consists of an axial and azimuthal magnetic field component. Leka et al. (2005) demonstrate that only at the center of the flux tube, where the radial distance from its axis r equals zero, the twist density can be retrieved from α_z measurements directly. They describe the following relationship between α_z, the twist density q and the distance from the flux tube axis as:

$$\alpha_z(r) = \frac{2q}{1 + q^2 r^2}. \tag{3.21}$$

Note that in this configuration α_z goes towards zero when r increases to infinity. This finding led them to propose the α_{Peak} method.

We can find a similar relationship between α_{Peak} and the twist density q for our empirical sunspot model. Taking the model's equation for B_θ (Eq. 3.4) with $q = \frac{b}{8a_0\sqrt{1+b^2}}$, we get the twist density equation from Nandy et al. (2008):

$$B_\theta(r) = q r B_z. \tag{3.22}$$

Together with the model's B_z component,

$$B_z(r) = B_0 \exp\left[-(\log_e 2)\left(\frac{r}{h_0}\right)^2\right], \tag{3.23}$$

we can use derivatives in cylindrical coordinates to calculate α_z. Note that B_r in Eq. 3.3 does not depend on the azimuthal angle θ. Then the radial profile of α_z is:

$$\begin{aligned}\alpha_z &= \frac{1}{rB_z}\left[\frac{\partial(rB_\theta)}{\partial r} - \cancel{\frac{\partial B_r}{\partial\theta}}\right] = \\ &= \frac{1}{rB_z}\frac{\partial}{\partial r}\left\{qB_0 r^2 \exp\left[-(\log_e 2)\left(\frac{r}{h_0}\right)^2\right]\right\} =. \\ &= 2q\left[1 - (\log_e 2)\left(\frac{r}{h_0}\right)^2\right]\end{aligned} \tag{3.24}$$

We get a maximum value of α_z (α_{Peak}) at the flux tube's center, i.e. $r = 0$. Therefore, we find the same relationship of $\alpha_{\mathrm{Peak}} = 2q$ as Leka et al. (2005).

In our empirical sunspot model α_z changes sign at a certain distance from the sunspot's center. We can determine where alpha changes sign by setting α_z in Eq. 3.24 equal to zero to get

$$r_{\alpha_z=0} = \frac{h_0}{\sqrt{\log_e 2}} \approx 1.2\, h_0. \tag{3.25}$$

The parameter h_0 describes the distance of the umbra/penumbra boundary measured from the model spot's center. Disregarding fluctuations of the magnetic field, within the umbra the sign of the twist and α_z are the same, according to our model.

Since $\alpha_z = J_z/B_z$, such a sign reversal can only happen in our sunspot model with positive polarity, if the sign of the vertical current density J_z changes. Such rings of return currents at the umbra/penumbra boundary of observed sunspots are reported in literature (e.g. Tiwari et al. 2009a). We note that positive and negative vertical currents are balanced in our model.

4 Twist measurements in emerging active regions

In this chapter I characterize measurements of the twist proxy α_z based on an independent data set of 182 active regions observed by SDO/HMI (HEAR survey, Schunker et al. 2016). The first goal is to examine whether the previously reported hemispheric helicity sign rule (HHSR, e.g. Longcope et al. 1998) can be retrieved from a statistical sample data. The second goal is to characterize the average temporal evolution of magnetic twist in emerging active regions.

4.1 Data and methods

I studied active regions belonging to the HEAR survey by Schunker et al. (2016). This survey contains 182 active regions, which are tracked up to 7 days before and after their emergence in Postel projected vector magnetograms (1024 × 1024 pixel, 0.35 Mm pixel scale) based on the hmi.b_720s series (Hoeksema et al. 2014).

The emergence time of an active region (t_{em}) is defined as the time, when the total unsigned magnetic flux of the respective active region reaches 10% of its peak value within 36 hours after the active region is first mentioned in the NOAA records. The observations available for each active region are organized in data chunks of approximately 6.8 hours, called time intervals (TIs). The TI labeled TI+0 contains the observations at the emergence time, while positive TIs represent post-emergence time and negative TIs contain observations before the emergence. I refer to each TI also with its mid-time relative to the emergence time of the active region. As an example, TI+0 is equivalent to t_{em} + 0.10d, because the mid-time of TI+0 is 0.1 days after the emergence time.

All observations of an active region in one datacube TI are temporally averaged to a single observation to reduce noise. The results of this chapter do not change, whether I used TI-averaged observations or measured the twist in each observation individually.

All HMI observations currently contained in the HEAR survey were made between 2010 and 2014. Therefore, they all belong to the same solar cycle 24 (2008-2019). In this time period the leading polarity in the northern/southern hemisphere was negative/positive, respectively.

Chapter 3 shows that twist estimation methods based on spatial averages of α_z make reliable measurements in our simple sunspot model with a fluctuating magnetic field. However, they can not retrieve the known twist density of our model directly, but a conversion factor has to be applied based on the azimuthally symmetric α_z profile (Section 3.8). As mentioned in the previous chapter and as I will show in Section 4.2, real sunspots have usually a more complex magnetic field structure than our simple model and it is not clear if using a conversion factor would still retrieve the twist density. Nevertheless, Leka and Skumanich (1999) states that by applying the same method on each observation, active-region comparisons are possible, at least in a qualitative sense.

To characterize the magnetic twist in active regions, I chose the spatial average of α_z weighted by the squared vertical magnetic field B_z, $\langle\alpha_{\mathrm{z}}^{\mathrm{sqr}}\rangle$, to minimize the effect of weak field, where vector magnetic field measurements have larger uncertainties. It also puts more weight on the center of magnetic polarity patches, where α_z should more closely relate to the twist density, if the magnetic field in these patches resembles the ideal picture of uniformly twisted flux tubes.

I restricted the area, where α_z is calculated, to pores and umbral/penumbral areas of active regions. In order to detect such features, I used HMI continuum observations of active regions, which are also provided by the HEAR survey based on the HMI data product hmi.ic_45s (Hoeksema et al. 2014). I normalized the continuum image of each observation following the procedure described in Gottschling et al. (2021). I convolved the observation with a Gaussian with a standard deviation of 5 degree (173 pixels or 60.55 Mm) and divide the original observation by this background. The pixel values in the normalized continuum observation can then be used to detect umbrae (<0.65), penumbrae (between 0.65 and 0.85) and quiet Sun (>0.85). I note that Gottschling et al. (2021) used an upper limit of 0.95 for penumbrae. I chose a value of 0.85, which works better from visual inspection in the context of the data set that I used. I created masks for each available observations, where the normalized continuum maps had values below 0.85 to identify pixels for the α_z calculations.

I excluded 30 active regions from the survey. These include active regions that don't follow Hale's law, are discarded due to their complexity, unreliable detection of the continuum masks or other strong magnetic field structures in the vicinity of the active region. The full list of active regions used in this study can be found in Appendix A.

4.2 Examples of twist measurements in two active region observations

Section 3.7 showed that the magnetic field structure in a sunspot can be more complicated than our simple uniformly twisted model and has areas with opposite sign of twist that persist for hours. In this Section I present maps of the vector magnetic field (B_x,B_y,B_z), continuum, vertical current density J_z and twist proxy α_z measurements in two active regions.

The first example is the simple bipolar active region NOAA AR 11080 (Fig. 4.1 and Fig. 4.2) approximately one day after emergence (TI+5). Fig. 4.3 and Fig. 4.4 show NOAA AR 11158 four days after emergence (TI+20), which is not included in the later statistical studies, due to its complexity. I present NOAA AR 11158 because it nicely illustrates aspects of measured α_z profiles that also occur in other simpler active regions. The black and yellow contours in these figures represent the continuum masks used for calculating α_z and outline the negative/positive polarity patches, respectively.

The idealized picture of simple bipolar active regions like NOAA 11080 is that a single uniformly twisted flux tube connects both polarity patches in a loop-like structure.

If this loop is viewed from top, the sign of the observed magnetic field twist changes from the leading to the following polarity, where the foot-points of the flux tube are located. This is the case in NOAA AR 11080, where the dominant sign of the vertical current $J_z = (\mathbf{\nabla} \times \mathbf{B})_z$, which corresponds to the chirality of the observed field, changes from the positive to the negative polarity. Since also the sign of B_z changes from one foot-point to the other, the sign of $\alpha_z = J_z/B_z$ is expected to be the same in both polarities, as expected from a uniformly twisted flux tube.

Previous results on the HHSR state that the magnetic field is preferentially left-handed ($\langle\alpha_z\rangle < 0$) in the northern and right-handed ($\langle\alpha_z\rangle > 0$) in the southern hemisphere. In this context, it is interesting to note that NOAA AR 11080 emerged in the southern hemisphere at about −23° latitude and has $\langle\alpha_z^{\mathrm{sqr}}\rangle = -0.038 \pm 0.005\ \mathrm{Mm}^{-1}$. In the southern hemisphere the HHSR predicts on average positive values of α_z. Therefore, NOAA AR 11080 represents an exception to the HHSR.

The second example, NOAA AR 11158, is dominated by positive α_z values ($\langle\alpha_z^{\mathrm{sqr}}\rangle = 0.050 \pm 0.004\ \mathrm{Mm}^{-1}$). This is consistent with the HHSR, since the active region emerged on the southern hemisphere at −19° latitude. A curious feature of this active region is the negative polarity patch in the south-east. It shows the opposite (negative) sign of α_z with respect to all the other parts of the active region. This contradicts the idea that this polarity patch is connected to another patch by a uniformly twisted field structure.

The polarity patches in both active regions are rarely close to being circular, which is an assumption to interpret measurements of α_z as a twist density of a uniformly twisted flux tube. For example, the leading positive polarity patch of active region 11080 is elongated to the east, caused by the presence and emergence of weak field in this area. I usually observed circular patches with a similar α_z-profile to our model (compare Fig 3.7) only for a short period after flux emergence, and the complexity of the α_z-profiles increased within few hours after the emergence. Large field structures, like the leading polarity in the north-west of active region 11158, that still resemble the model are a rare occurrence.

4.3 Measuring the hemispheric helicity sign rule

The first question of interest is, whether the HHSR can be retrieved from spatial averages of α_z over active regions in the HEAR survey. Longcope et al. (1998) measured unweighted spatial averages of α_z ($\langle\alpha_z\rangle$) in vector magnetograms of 203 active regions from the Haleakala Stokes Polarimeter (Mickey 1985). They assessed the uncertainty of $\langle\alpha_z\rangle$ for one active region from observations of the same active region at different times. They plotted the values of each active region against the active region's heliographic latitude and found by linear regression a slope of $-2.7 \times 10^{-10}\ \mathrm{deg}^{-1}\ \mathrm{m}^{-1}$.

I measured $\langle\alpha_z^{\mathrm{sqr}}\rangle$ in 152 active region in every available TI from TI+0 ($\mathrm{t_{em}}$ + 0.10 days) to TI+20 ($\mathrm{t_{em}}$ + 4.54 days) by averaging over all positive and negative polarity patches. Each data point in Fig. 4.5 shows the average $\langle\alpha_z^{\mathrm{sqr}}\rangle$ for one active region, plotted against the solar latitude of their emergence. The errorbars represent the standard error of $\langle\alpha_z^{\mathrm{sqr}}\rangle$ from different observations (i.e. TIs) of the respective active region.

A linear least-squares fit to the data yields a slope of $(-2.39 \pm 0.50) \times 10^{-10}\ \mathrm{deg}^{-1}\ \mathrm{m}^{-1}$, which is in agreement with the findings by (Longcope et al. 1998). The slope and its un-

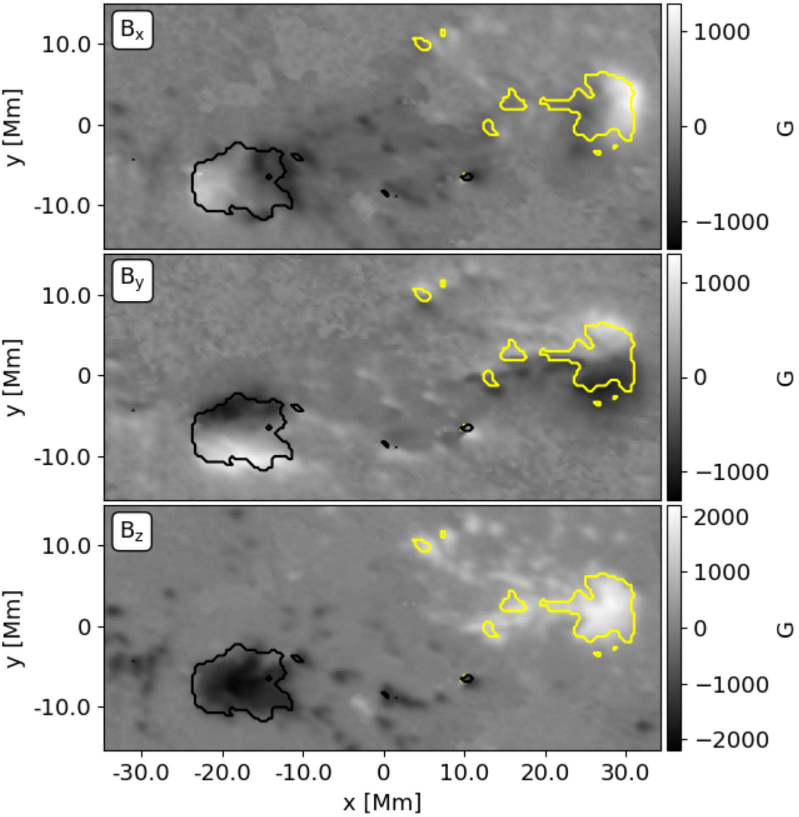

Figure 4.1: SDO/HMI vector magnetic field observation of active region 11080 (2010.06.11 03:48:00 TAI). The B_x, B_y and B_z components are shown from the top to the bottom panel, respectively. The yellow and black contours outline the positive and negative polarity patches, respectively.

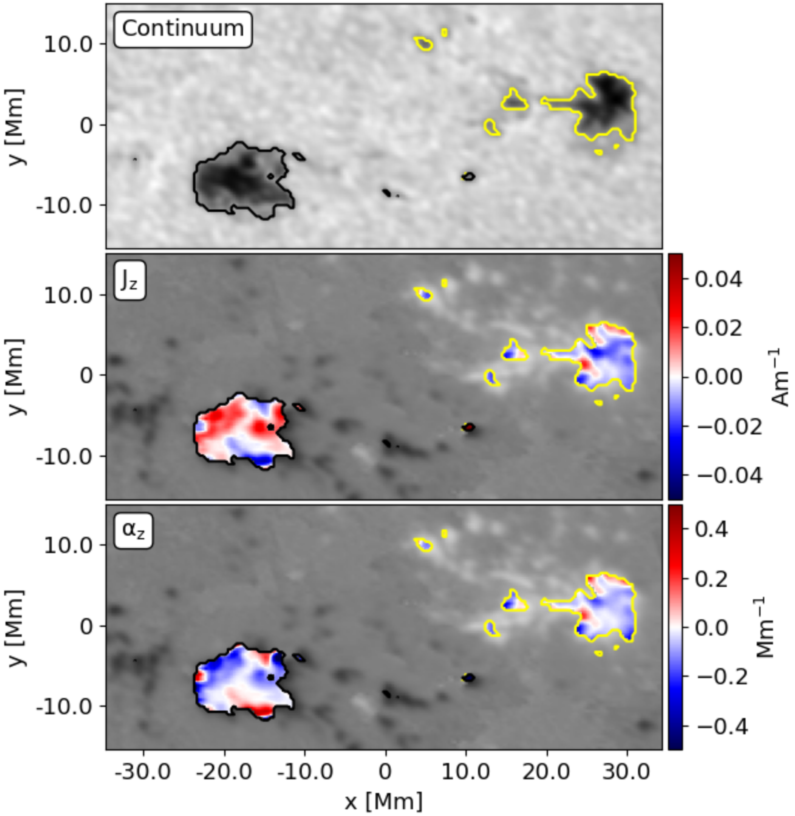

Figure 4.2: Continuum, vertical current and α_z maps of active region 11080. The top panel shows the continuum observation (2010.06.11 03:52:30 TAI). The middle and bottom panel display the vertical current and force-free parameter α_z in red and blue. The background shows the vertical field B_z in gray scale. The yellow and black contours outline the positive and negative polarity patches, respectively.

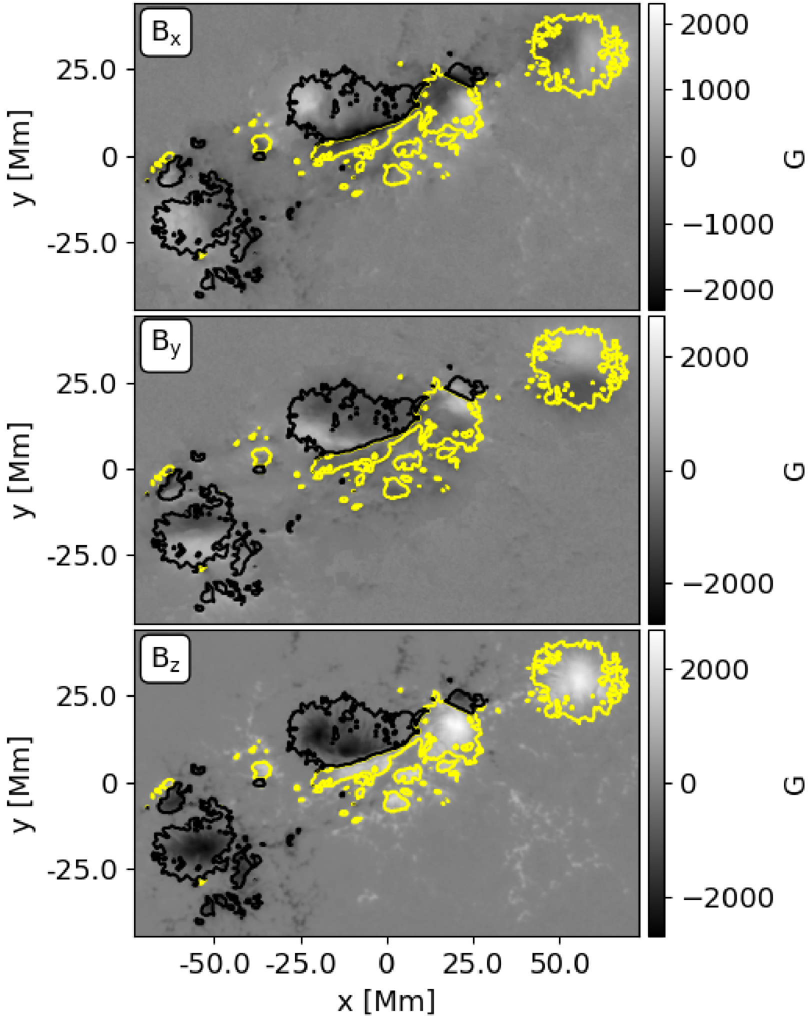

Figure 4.3: SDO/HMI vector magnetic field observation of active region 11158 (2011.02.15 11:12:00 TAI). The B_x, B_y and B_z components are shown from the top to the bottom panel, respectively. The yellow and black contours outline the positive and negative polarity patches, respectively.

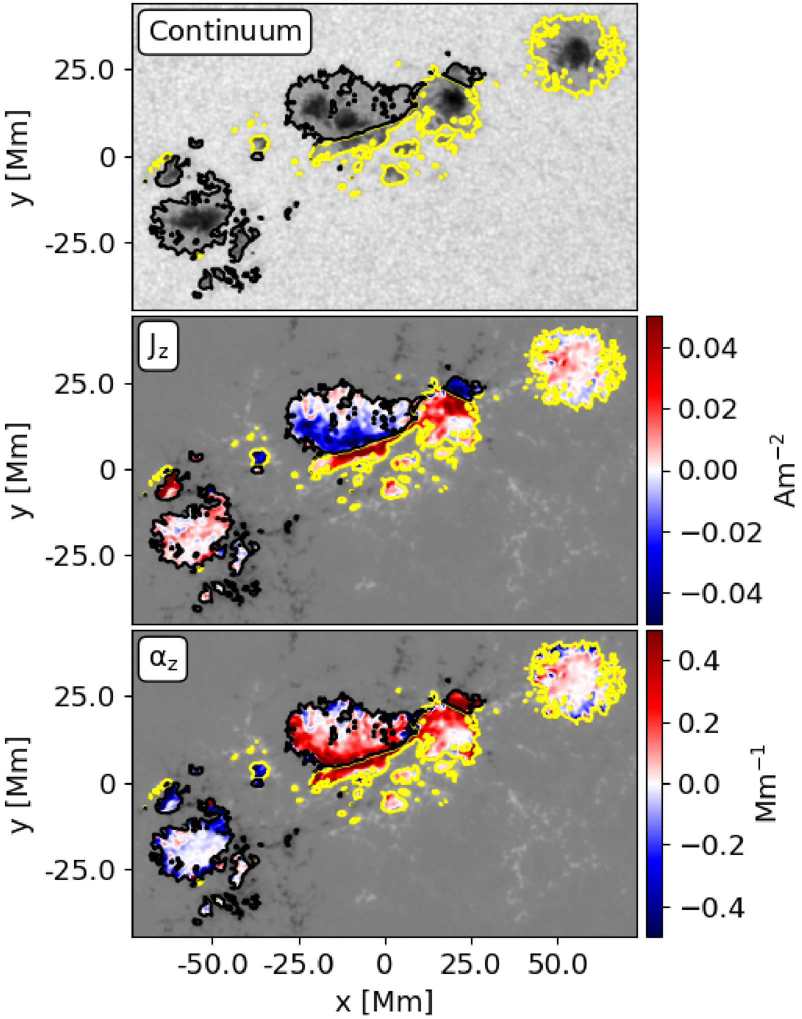

Figure 4.4: Continuum, vertical current and α_z maps of active region 11158. The top panel shows the continuum observation on (2011.02.15 11:08:15 TAI). The middle and bottom panel display the vertical current and force-free parameter α_z in red and blue. The background shows the vertical field B_z in gray scale. The yellow and black contours outline the positive and negative polarity patches, respectively.

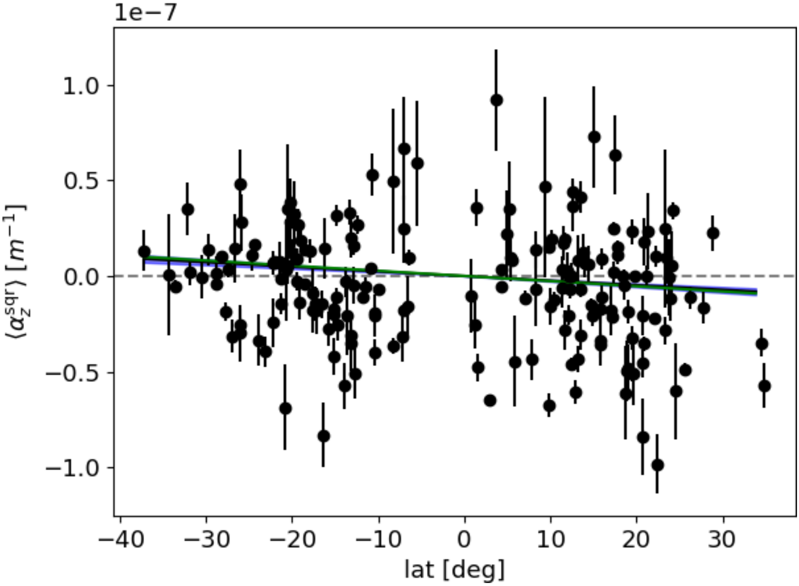

Figure 4.5: Spatial average of α_z weighted by B_z^2 of active regions versus solar latitude. Each data point represents the mean of measurements in one active region. The errorbars show the standard deviation derived from observations in different TIs of the same active region. The blue shaded area represents the uncertainty of the best linear fit with a slope of $(-2.39 \pm 0.50) \times 10^{-10}$ deg^{-1} m^{-1}. The green line represents the result from Longcope et al. (1998) with a slope of -2.7×10^{-10} deg^{-1} m^{-1}.

certainty represent the mean and standard deviation from Monte-Carlo simulations, where I shifted the data points within their uncertainties in 1000 realizations.

The HHSR derived from α_z only shows a very weak statistical tendency. This is also reflected in the amount of active regions that obey the HHSR. I find that 44 of 75 (59%) active regions in the northern and 37 of 77 (48%) in the southern hemisphere obey the HHSR.

4.4 Evolution of twist in the leading and following polarity of emerging active regions

As the next step, I wanted to study how α_z evolves in active regions during their emergence. Section 4.2 explains that under the assumption of uniform twist in an active region (or at least a preferential direction of the twist in accordance to the HHSR), leading and following polarities of active regions should have the same sign of α_z. Section 1.1.4 explains that the leading and following polarities of active regions have many asymmetrical properties including their helicity fluxes.

Therefore, I investigated the evolution of $\langle \alpha_z^{\mathrm{sqr}} \rangle$ not only for the whole active region, but also in the leading and following polarity, separately. I calculated $\langle \alpha_z^{\mathrm{sqr}} \rangle$ in each TI-averaged observation of an active region for the leading, following and both polarities and average the resulting values of every active region at a specific TI in the northern and southern hemisphere.

Fig. 4.6 presents the result of this study. There is a clear separation with opposite signs of $\langle \alpha_z^{\mathrm{sqr}} \rangle$ between the two polarities in both hemisphere. Only the leading polarities (negative/positive in the northern/southern hemisphere) follow the HHSR. These results imply that leading and following polarities are twisted in opposite directions.

Within the uncertainties, $\langle \alpha_z^{\mathrm{sqr}} \rangle$ stays constant in both polarities during the observation time and a clear evolution cannot be seen following the emergence.

Another consequence of these findings is that positive vertical currents exists in both polarities ($\alpha_z = J_z/B_z$). This is not intuitive, since currents in the picture of uniformly twisted flux tubes and force-free magnetic field models travel along the magnetic field. If the magnetic field in positive and negative polarities are connected by a monolithic flux tube, one would assume that currents flow from one polarity to the other, and one would measure the opposite sign of vertical currents in the different polarities.

I measured the net current of active regions in the data set by integrating the vertical current density J_z over whole active regions and the surrounding quiet Sun. I found that the vertical currents in active regions are still balanced. Therefore, active regions have "drains" for these net positive currents.

The finding that only the leading polarities follow the HHSR raises the question, how the HHSR could still be retrieved in Section (Section 4.3). This can possibly be explained with a systematic effect caused by the asymmetries of leading and following polarities. The leading polarity patches are usually larger, stronger in field strength and more coherent than the dispersed following ones (Fan and Gibson 2004). Consequently, the flux concentration in individual patches of the following polarity is lower and sunspots do not develop to the same extent as for the leading polarity. I use continuum observations (i.e. sunspot images) as reference for the masks that determine, where α_z is calculated. Therefore, it is likely that I consider more pixels of the leading polarity in each observation and put an artificial weight on the average sign of α_z, favoring the leading polarity. A similar effect may have also occurred in other studies of the HHSR, where α_z is usually averaged over whole active regions.

4.5 Vertical current and twist in an averaged polarity patch

The asymmetric behavior of leading and following polarities described in Section 4.4 is inconsistent with twisted flux tube models. Therefore, I studied the properties of stacked and averaged leading and following polarities in more detail. The procedure to stack and average polarities is the same for the leading and following polarity. The results from averaged leading and following polarities are qualitatively equivalent, with results from the following polarity being noisier, due to their weaker and more dispersed field structure. Therefore, I focus in this Section only on the leading polarity.

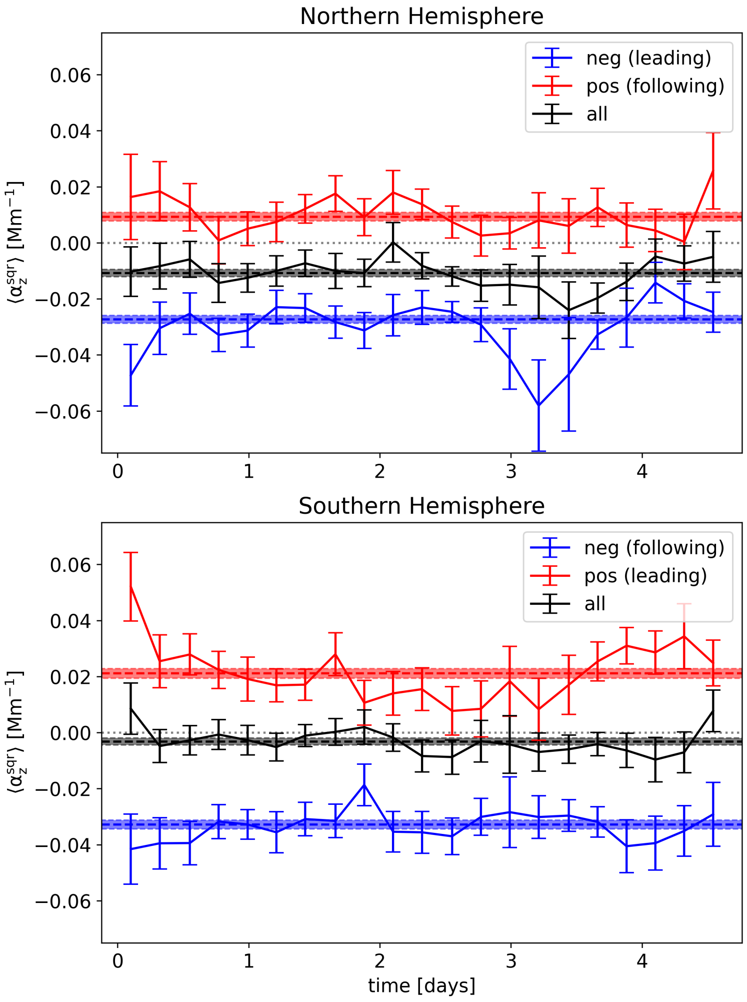

Figure 4.6: Spatial average $\langle \alpha_z^{\mathrm{sqr}} \rangle$ over all active region's negative (neg) and positive (pos) polarities as well as averages over both polarities (all) in the northern and southern hemisphere (top/bottom panel, respectively) versus time relative to emergence (t_{em}). The errorbars represent the standard error based on observations from different active regions within the same TI. The shaded areas represent the mean and standard error of the curves with the same color.

To create an average leading polarity patch, I identified in every observation the leading polarity patch that has the highest total magnetic flux. I detected its flux-weighted center of $|B_z|$ and shifted the whole map, so that the flux-weighted center of the patch is located in the center of the whole map. I adjusted vector magnetograms of active regions from the southern hemisphere by flipping the observation in the latitudinal direction and changing the sign of B_x and B_z to make them comparable to magnetograms from the northern hemisphere. This procedure was repeated for each active region in one TI and eventually all maps were averaged for that TI. Fig. 4.7 displays example magnetograms of the averaged stacked leading polarity at emergence (TI+0) and approximately 1.2 days (TI+5) and 2.3 days (TI+10) after emergence (t_{em}).

Fig. 4.8 and 4.9 show maps of the vertical current J_z and the force-free parameter α_z of the stacked leading polarity, respectively. These figures display regions with opposite sign clearly separated by an inversion line in the center of the spot. This is an unexpected result, since I would anticipate a uniform structure if there are only net positive or negative currents or in the case of field structure with return currents a similar profile to our sunspot model shown in Fig. 3.7 (middle panel).

When I measured J_z and α_z in a small central area with a radius of 5.25 Mm (15 px, black dotted circles in Fig. 4.8 and 4.9), I still measure a dominant positive current and negative $\langle \alpha_z^{\mathrm{sqr}} \rangle$, consistent with my previous results and the HHSR for a leading polarity patch on the northern hemisphere. The averaged following polarity shows a net positive current in the center as well, but due to having the opposite polarity $\langle \alpha_z^{\mathrm{sqr}} \rangle$ is positive, disobeying the HHSR.

Another feature of Fig. 4.8 and 4.9 is the apparent rotation of the inversion line. During their lifetime, active regions travel across the visible solar disk from east to west, due to the solar rotation. Active regions in the HEAR survey are tracked in time intervals relative to their emergence on the visible solar disk. Therefore, observations of later TIs are likely further west than earlier TIs. Consequently, the stacked polarity patches from earlier/later TIs contain preferentially patches from active regions that are further east/west. This suggests that the rotation of the inversion line in Fig. 4.8 and 4.9 might be related to the longitudinal position relative to the central meridian.

To assess this rotation, I repeated the process of stacking the main polarity patches, but now I separated observations based on their longitudinal location from −60° to 60° relative to the solar central meridian in bins of 15°. This way, I get a stacked polarity patch for each TI in each longitude bin. Fig. 4.10 shows the vertical current maps J_z for each latitude bin.

I determined the coordinates of the center of mass for positive $(x_{\mathrm{p}}, y_{\mathrm{p}})$ and negative values $(x_{\mathrm{n}}, y_{\mathrm{n}})$ in the central area of the spot with a radius of 5.25 Mm (15 pixel, black dotted circle in Fig. 4.8 and 4.9), which are marked with plus and minus signs, respectively in Fig. 4.8 and 4.9. I calculated the angle γ of the line connecting the plus and minus sign with regard to the east-west direction to characterize the orientation of the inversion line:

$$\gamma = \arctan\left(\frac{y_{\mathrm{n}} - y_{\mathrm{p}}}{x_{\mathrm{n}} - x_{\mathrm{p}}}\right). \tag{4.1}$$

Decreasing values of γ refer to a clockwise rotation. Fig. 4.11 shows the average angle of the inversion line plotted against the longitude relative to the solar central meridian. One can see a clear rotation, suggesting a systematic effect in the data. What kind of

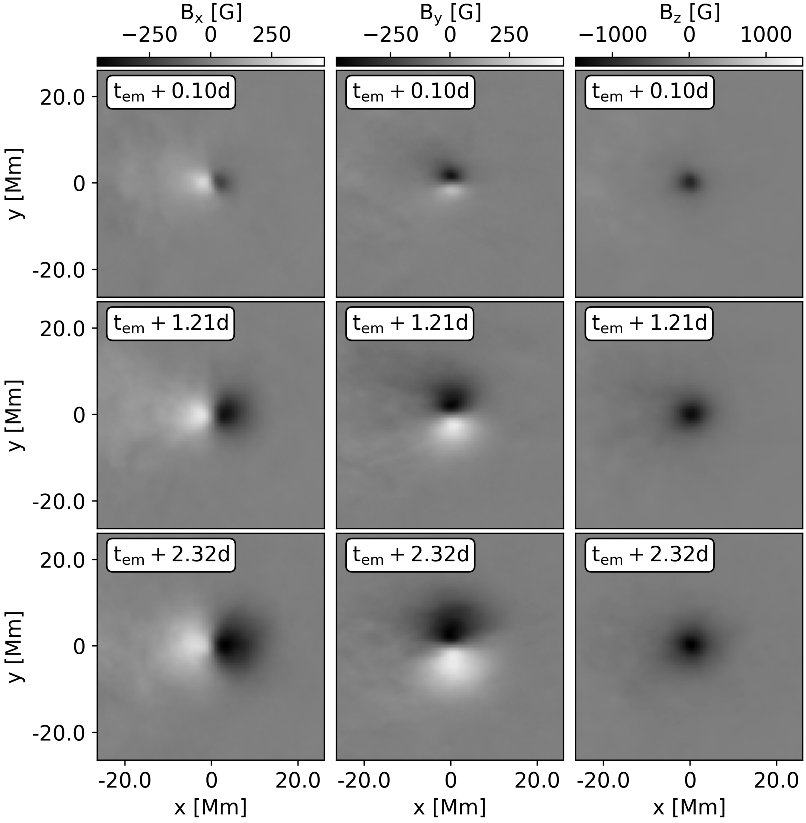

Figure 4.7: Vector magnetic field components of the averaged leading polarity based on 152 active regions. The columns from left to right show the B_x, B_y and B_z vector components of the magnetic field. The top, middle and bottom row show the stacked and averaged leading polarity 0.10, 1.21 and 2.32 days after the emergence time ($\mathrm{t_{em}}$), respectively.

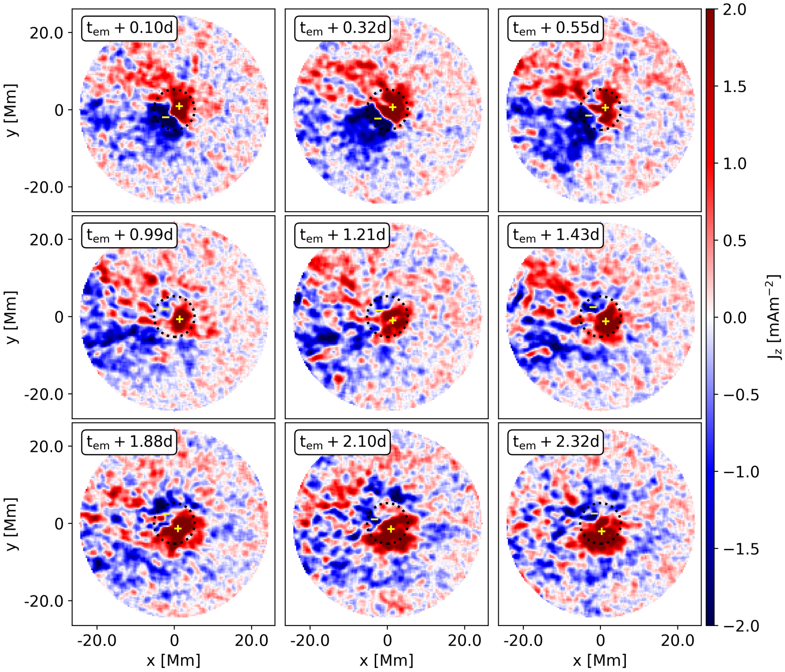

Figure 4.8: Profile of the vertical current J_z in the average leading polarity at different times after the emergence (t_{em}). The yellow plus and minus symbols represent the center of mass of positive and negative values of J_z within the dotted black circle, respectively.

systematic effect is responsible for this rotation is not clear and might be a research topic for further studies.

4.6 Summary and Discussion

I showed in this chapter by the example of a simple bipolar and a complex active region that the field structure often does not resemble the picture of monolithic uniformly twisted flux tubes that connect individual polarity patches. Individual patches also have usually a more complex structure than our simple model as presented in Section 3.5. Therefore, the interpretation of α_z remains difficult and can only be used as a proxy to characterize the magnetic field's complexity.

Under this premise, I showed that the HHSR previously reported in literature (e.g. Longcope et al. 1998) can be retrieved from active regions in the HEAR survey with a spatial average of α_z weighted by B_z^2, $\langle \alpha_z^{\mathrm{sqr}} \rangle$. However, a closer inspection of the active region's leading and following polarities revealed that only the leading polarities follow the

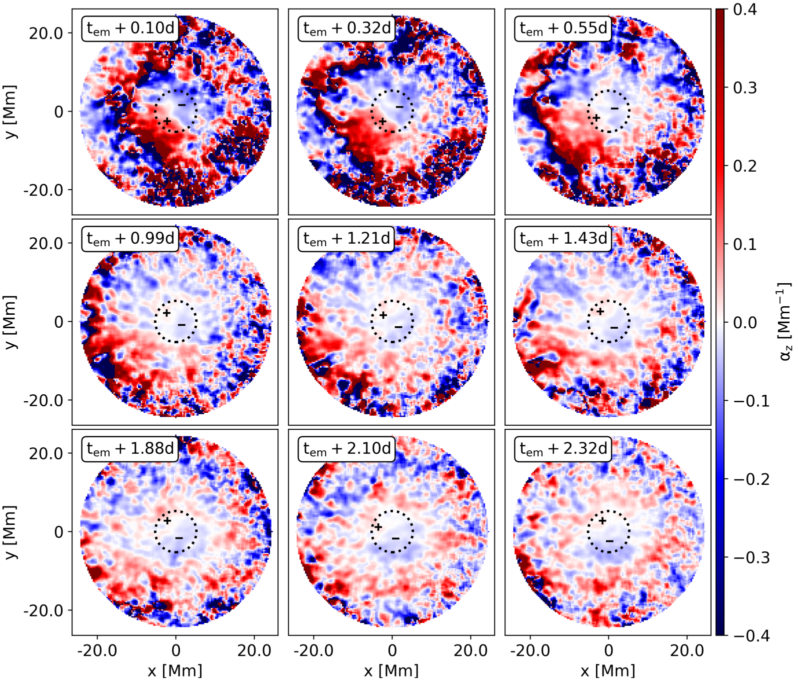

Figure 4.9: Profile of the the force-free parameter α_z in the average leading polarity at different times after the emergence (t_{em}). The yellow plus and minus symbols represent the center of mass of positive and negative values of α_z within the dotted black circle, respectively.

HHSR in the northern and southern hemisphere, while the following polarities have twist of the opposite sign. This is an inconsistent result with models of uniformly twisted flux tubes but not completely unprecedented. Tian and Alexander (2009) measured helicity flux in 15 emerging bipolar active regions. They found that the leading polarity experiences a 3-10 times larger helicity injection rates than the following polarities. Their plots also reveal that the helicity injection in the following polarity in many cases has periods, where the opposite sign of helicity is injected. This can result in leading and following polarity patches with opposite sign of twist. That the HHSR could still be retrieved with averages over whole active regions can be attributed to the leading polarity contributing more pixels to the spatial average and having stronger magnetic field, which becomes noticeable in the weighting (B_z^2) of the average.

Another implication of having $\langle\alpha_z^{\mathrm{sqr}}\rangle$ with opposite signs in the leading and following polarities of active regions is that active regions have a net positive current in both magnetic polarity patches. Still, the vertical current in the observed active regions is balanced. Therefore, the current has to be compensated somewhere. One possibility are rings of

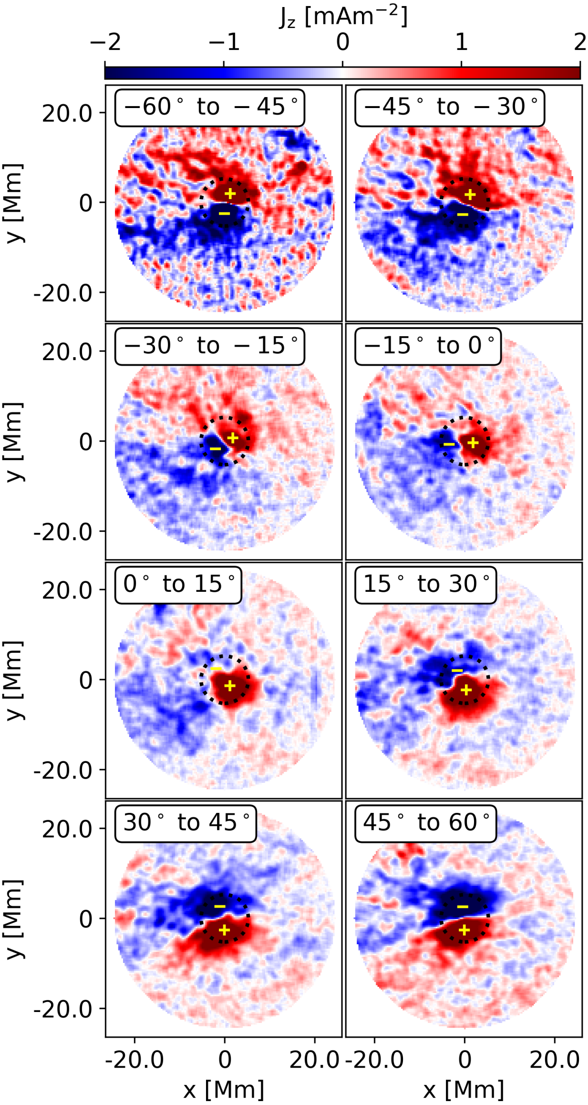

Figure 4.10: Maps of the vertical current J_z of the average leading polarity in different longitude bins. The yellow plus and minus symbols represent the center of mass of positive and negative values of J_z within the dotted black circle, respectively.

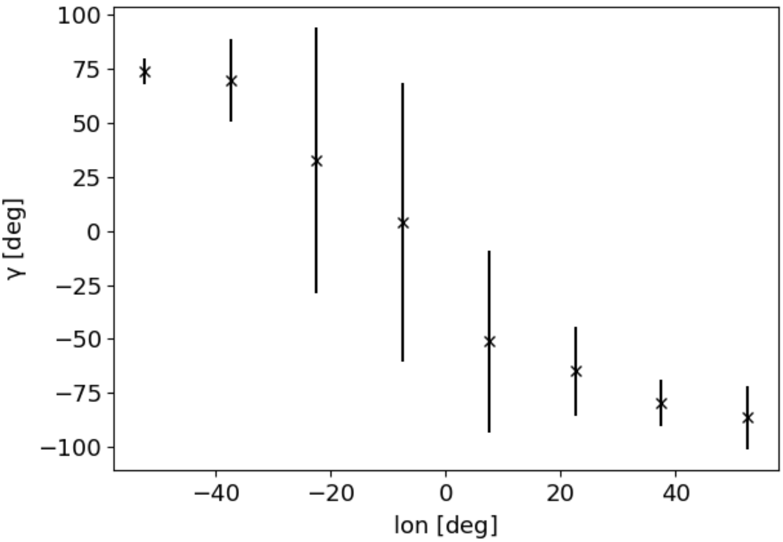

Figure 4.11: The angle of the connection line between positive and negative centers of mass (J_z) in the averaged leading polarity relative to the east-west direction (tilt in Fig. 4.8) as a function of longitude. The errorbars are derived from the variation of averaged leading polarities at different TIs in one latitude bin.

return currents that surround the area of positive current. Such a ring of return currents exists in our sunspot model, presented in the previous chapter, and are also reported in literature (e.g. Zhang 2006, Tiwari et al. 2009a) for individual cases.

Finally, I presented an averaged leading polarity of active regions in the HEAR survey, which has a split profile of positive and negative J_z and α_z values in the center. This profile rotates as a function of solar longitude. The following polarity shows the same behavior. In both, the averaged leading and following polarity, the same results concerning the HHSR and the predominant current can be retrieved from their central area, as described above. However, the split and rotating profiles of J_z and α_z, depending on their position relative to the central meridian, hints at a systematic effect in the observations, which needs further investigation.

Acknowledgements

The data used in this chapter are courtesy of NASA/SDO and the HMI Science Team.

5 Discussion and outlook

5.1 Joy's law

Chapter 2 shows that active regions emerge on average with zero tilt and Joy's law develops within a day after the emergence. The creation of the tilt is driven by an inherit north-south separation speed of the polarities with unknown origin. The evolution of the magnetic field is linked to the conservation of magnetic helicity. Therefore, studying the evolution of writhe (as a proxy for the tilt) and twist in emerging active regions can give further insights into Joy's law and the driving source of the north-south separation speed.

A possible explanation is that the magnetic field on average emerges with just the right amount of twist and writhe so that the whole field structure appears to be east-west aligned. The observed magnetic footpoints of the flux tubes shift in the photosphere according to the flux tube's helical structure, while the field further rises into the solar atmosphere. This could explain the change in the observed tilt angle of active regions during the emergence process. The movement of the footpoints stops, when the magnetic field structure is fully emerged. Their eventual orientation can then be interpreted as Joy's law (López Fuentes et al. 2003).

Another explanation is that Joy's law is caused by an unwinding of flux tubes after the emergence. In chapter 2 we speculate based on findings by Birch et al. (2019) that supergranulation guides the emerging magnetic field into east-west aligned north-south converging flows, which causes the polarities to emerge on average east-west aligned, i.e. without tilt. Many theories predict that a flux tube, that rises through the convection zone, has to be inherently twisted, due to a strong tendency for fragmentation (Schuessler 1979, Longcope et al. 1996, Fan et al. 1998a, Abbett et al. 2000, Fan 2001). The HHSR predicts that this twist has a preferential sign in the northern/southern hemisphere. The forces imposing the twist onto the flux tube may no longer be present when the flux tube reaches the photosphere and the flux tube may unwind. Such behavior is supported through observations (e.g. Sangeetha et al. 2020). The flux tube has to compensate any loss of twist with writhe to conserve magnetic helicity, which would create the observed tilt.

Robust quantitative measurements of the twist are necessary to test these theories.

5.2 Interpretation of α_z

Chapter 3 shows that in a simple uniformly twisted magnetic field model, the force-free parameter α_z can robustly measure the twist density q even in a fluctuating magnetic field. However, observed active regions have in general a more complex structure (section 4.2) and the interpretation of α_z in terms of twist is not straightforward. I agree with Leka and Skumanich (1999) that spatial averages of α_z usually underestimate the magnetic complexity of active regions or even individual sunspots.

There are many aspects that need to be further explored to better interpret α_z in terms of twist. For example, it is usually assumed that flux tubes are uniformly twisted. The twist is one component of the magnetic field's helicity, which is a quantity calculated in 3-dimensional space. In contrast, α_z is calculated on a 2-dimensional plane. Therefore, α_z can only be interpreted as a twist density. The total twist of a uniformly twisted flux tube (Eq. 3.1) could then be calculated by integrating the twist density along the length of the flux tube, but the shape and length of the flux tube is not known from photospheric observations.

The assumption that the magnetic field in a single flux tube is uniformly twisted might also not be true. We know that the radius R of a vertical flux tube expands with height in the solar atmosphere, because of the gas pressure gradient (Aschwanden 2005). The axial field decreases faster ($B_z \propto R^{-2}$, due to magnetic flux conservation) than the azimuthal field ($B_\theta \propto R^{-1}$, due to current conservation) with height, which creates a more twisted field (Fan et al. 1998b).

Furthermore, Longcope and Welsch (2000) state that twist can be transported along the magnetic field via torsional Alfvén waves and subphotospheric twist can still be injected into the observed magnetic field after emergence.

Chapter 3 showed that a uniformly twisted sunspot model with a spatially correlated fluctuating field can create α_z profiles that look similar to observations. These profiles have areas with opposite sign of twist throughout the modelled sunspot. In observations these patches persist for hours (Pevtsov et al. 1994, e.g.). So far, we only considered the spatial correlations of the magnetic field fluctuations. The temporal correlations can be incorporated in the model to further investigate the impact of magnetic field fluctuations on these structures.

Twist represents helicity on small scales, therefore understanding the magnetic fine structure in sunspots is crucial. We need vector magnetic field observations of emerging active regions in high spatial, temporal and spectral resolution to better understand this fine structure and its evolution. For example, observations with the Sunrise mission (Solanki et al. 2010, 2017) revealed a lot of magnetic fine structure in sunspots that is not resolved in HMI observations (e.g. Chitta et al. 2017).

All of that being said, spatial averages of α_z can still be used to qualitatively learn about the dominant sign of the magnetic field's twist in the solar photosphere.

5.3 Measurements of twist and vertical currents in HMI observations

I presented measurements of the twist proxy α_z in emerging active regions in chapter 4. I showed that the HHSR can be retrieved from the HEAR survey (Schunker et al. 2016) but found that on average only the leading polarity obeys the HHSR. This result may be rooted in an inherit asymmetry of the helicity fluxes in leading and following polarities as reported by Tian and Alexander (2009).

Only 59% (48%) of active regions in the northern (southern) hemisphere followed the HHSR in my study. Although it is known that the HHSR is in general only a weak statistical tendency, this quota is quite low. Manek and Brummell (2021) suggests that the HHSR is only weakly pronounced in the period from solar minimum to solar maximum (see section 1.3.3). All studied active regions were observed during the rise of the 24th solar cycle (2010-2014). Therefore, my findings can be explained by Manek and Brummell (2021)'s theory. Big data sets of vector magnetograms of active regions are needed that span multiple solar cycle to investigate whether the strength of the HHSR varies throughout the solar cycle or not. A first step could be to extend the HEAR survey to all currently available HMI observations up to 2021.

A consequence of the asymmetry between leading and following polarities is that in both polarities a dominant positive vertical current exists. The net vertical current over whole active regions is balanced in the observations. Therefore, there have to be areas where this positive current is compensated. Various studies (e.g. Tiwari et al. 2009a, Su et al. 2009) suggest the existence of return currents at the umbra-/penumbra boundary of sunspots. The study of many individual sunspots and smaller magnetic features in the HEAR survey can give further insights into the current structure of these magnetic features.

This study also revealed an apparent rotation of the vertical current and α_z profiles in an averaged leading polarity patch. These profiles rotate as a function of longitudinal distance of the averaged polarity patch from the central meridian. This is most likely caused by some systematic projection effect in the observation. It was recently reported that a sign bias exists in HMI vector magnetograms for the east-west aligned field (Griñón-Marín et al. 2021, Pevtsov et al. 2021). The sign of this magnetic field component changes as the observed field crosses the central meridian for magnetic field with weak to medium field strength. Systematic projection effects in observations are known for a long time (e.g. Beckers and Schröter 1969). Their origin and effect on measurements of α_z and the HHSR has to be studied in further detail.

Bibliography

Abbett, W. P., Fisher, G. H., and Fan, Y.: 2000, *ApJ* **540(1)**, 548

Aschwanden, M. J.: 2005, *Physics of the Solar Corona. An Introduction with Problems and Solutions (2nd edition)*, Springer Verlag

Astropy Collaboration, Price-Whelan, A. M., Sipőcz, B. M., Günther, H. M., Lim, P. L., Crawford, S. M., Conseil, S., Shupe, D. L., Craig, M. W., Dencheva, N., Ginsburg, A., VanderPlas, J. T., Bradley, L. D., Pérez-Suárez, D., de Val-Borro, M., Paper Contributors, P., Aldcroft, T. L., Cruz, K. L., Robitaille, T. P., Tollerud, E. J., Coordination Committee, A., Ardelean, C., Babej, T., Bach, Y. P., Bachetti, M., Bakanov, A. V., Bamford, S. P., Barentsen, G., Barmby, P., Baumbach, A., Berry, K. L., Biscani, F., Boquien, M., Bostroem, K. A., Bouma, L. G., Brammer, G. B., Bray, E. M., Breytenbach, H., Buddelmeijer, H., Burke, D. J., Calderone, G., Cano Rodríguez, J. L., Cara, M., Cardoso, J. V. M., Cheedella, S., Copin, Y., Corrales, L., Crichton, D., D'Avella, D., Deil, C., Depagne, É., Dietrich, J. P., Donath, A., Droettboom, M., Earl, N., Erben, T., Fabbro, S., Ferreira, L. A., Finethy, T., Fox, R. T., Garrison, L. H., Gibbons, S. L. J., Goldstein, D. A., Gommers, R., Greco, J. P., Greenfield, P., Groener, A. M., Grollier, F., Hagen, A., Hirst, P., Homeier, D., Horton, A. J., Hosseinzadeh, G., Hu, L., Hunkeler, J. S., Ivezić, Ž., Jain, A., Jenness, T., Kanarek, G., Kendrew, S., Kern, N. S., Kerzendorf, W. E., Khvalko, A., King, J., Kirkby, D., Kulkarni, A. M., Kumar, A., Lee, A., Lenz, D., Littlefair, S. P., Ma, Z., Macleod, D. M., Mastropietro, M., McCully, C., Montagnac, S., Morris, B. M., Mueller, M., Mumford, S. J., Muna, D., Murphy, N. A., Nelson, S., Nguyen, G. H., Ninan, J. P., Nöthe, M., Ogaz, S., Oh, S., Parejko, J. K., Parley, N., Pascual, S., Patil, R., Patil, A. A., Plunkett, A. L., Prochaska, J. X., Rastogi, T., Reddy Janga, V., Sabater, J., Sakurikar, P., Seifert, M., Sherbert, L. E., Sherwood-Taylor, H., Shih, A. Y., Sick, J., Silbiger, M. T., Singanamalla, S., Singer, L. P., Sladen, P. H., Sooley, K. A., Sornarajah, S., Streicher, O., Teuben, P., Thomas, S. W., Tremblay, G. R., Turner, J. E. H., Terrón, V., van Kerkwijk, M. H., de la Vega, A., Watkins, L. L., Weaver, B. A., Whitmore, J. B., Woillez, J., Zabalza, V., and Contributors, A.: 2018, *AJ* **156**, 123

Astropy Collaboration, Robitaille, T. P., Tollerud, E. J., Greenfield, P., Droettboom, M., Bray, E., Aldcroft, T., Davis, M., Ginsburg, A., Price-Whelan, A. M., Kerzendorf, W. E., Conley, A., Crighton, N., Barbary, K., Muna, D., Ferguson, H., Grollier, F., Parikh, M. M., Nair, P. H., Unther, H. M., Deil, C., Woillez, J., Conseil, S., Kramer, R., Turner, J. E. H., Singer, L., Fox, R., Weaver, B. A., Zabalza, V., Edwards, Z. I., Azalee Bostroem, K., Burke, D. J., Casey, A. R., Crawford, S. M., Dencheva, N., Ely, J., Jenness, T., Labrie, K., Lim, P. L., Pierfederici, F., Pontzen, A., Ptak, A., Refsdal, B., Servillat, M., and Streicher, O.: 2013, *A&A* **558**, A33

Babcock, H. W.: 1961, *ApJ* **133**, 572

Beckers, J. M. and Schröter, E. H.: 1969, *Sol. Phys.* **10(2)**, 384

Berger, M. and Field , G.: 1984, *Journal of Fluid Mechanics* **147**, 133

Berger, M. A.: 1984, *Geophysical & Astrophysical Fluid Dynamics* **30(1-2)**, 79

Berger, M. A. and Ruzmaikin, A.: 2000, *J. Geophys. Res.* **105(A5)**, 10481

Birch, A. C., Braun, D. C., Leka, K. D., Barnes, G., and Javornik, B.: 2013, *ApJ* **762**, 131

Birch, A. C., Schunker, H., Braun, D. C., and Gizon, L.: 2019, *A&A* **628**, A37

Birch, A. C., Schunker, H. S., Braun, D. C., Cameron, R., Gizon, L., Loeptien, B., and Rempel, M.: 2016, *Science Advances*

Borrero, J. M. and Ichimoto, K.: 2011, *Living Reviews in Solar Physics* **8(1)**, 4

Borrero, J. M., Tomczyk, S., Kubo, M., Socas-Navarro, H., Schou, J., Couvidat, S., and Bogart, R.: 2011, *Sol. Phys.* **273(1)**, 267

Brandenburg, A.: 2005, *ApJ* **625(1)**, 539

Brandenburg, A., Rädler, K.-H., Rheinhardt, M., and Subramanian, K.: 2008, *ApJ* **687(1)**, L49

Brandenburg, A. and Schmitt, D.: 1998, *A&A* **338**, L55

Burnette, A. B., Canfield, R. C., and Pevtsov, A. A.: 2004, *ApJ* **606(1)**, 565

Caligari, P., Moreno-Insertis, F., and Schussler, M.: 1995, *ApJ* **441**, 886

Cameron, R. and Schüssler, M.: 2015, *Science* **347**, 1333

Cameron, R. H., Duvall, T. L., Schüssler, M., and Schunker, H.: 2018, *A&A* **609**, A56

Cameron, R. H., Gizon, L., Schunker, H., and Pietarila, A.: 2011, *Sol. Phys.* **268(2)**, 293

Canfield, R. C. and Pevtsov, A. A.: 1998, in K. S. Balasubramaniam, J. Harvey, and D. Rabin (eds.), *Synoptic Solar Physics*, Vol. 140 of *Astronomical Society of the Pacific Conference Series*, p. 131

Carrington, R. C.: 1858, *MNRAS* **19**, 1

Charbonneau, P.: 2020, *Living Reviews in Solar Physics* **17(1)**, 4

Chatterjee, P., Choudhuri, A. R., and Petrovay, K.: 2006, *A&A* **449(2)**, 781

Chen, F., Rempel, M., and Fan, Y.: 2017, *ApJ* **846(2)**, 149

Chitta, L. P., Peter, H., Solanki, S. K., Barthol, P., Gandorfer, A., Gizon, L., Hirzberger, J., Riethmüller, T. L., van Noort, M., Blanco Rodríguez, J., Del Toro Iniesta, J. C., Orozco Suárez, D., Schmidt, W., Martínez Pillet, V., and Knölker, M.: 2017, *ApJS* **229(1)**, 4

Chou, D.-Y. and Wang, H.: 1987, *Sol. Phys.* **110(1)**, 81

Choudhuri, A. R.: 2003, *Sol. Phys.* **215(1)**, 31

Choudhuri, A. R., Chatterjee, P., and Nandy, D.: 2004, *The Astrophysical Journal* **615(1)**, L57

Choudhuri, A. R. and D'Silva, S.: 1990, *A&A* **239(1-2)**, 326

Choudhuri, A. R. and Gilman, P. A.: 1987, *ApJ* **316**, 788

Crouch, A. D.: 2012, *Sol. Phys.* **281(2)**, 669

Dasi-Espuig, M., Solanki, S. K., Krivova, N. A., Cameron, R., and Peñuela, T.: 2010, *A&A* **518**, A7

Démoulin, P. and Berger, M. A.: 2003, *Sol. Phys.* **215(2)**, 203

Démoulin, P., Mandrini, C. H., Van Driel-Gesztelyi, L., Lopez Fuentes, M. C., and Aulanier, G.: 2002, *Sol. Phys.* **207(1)**, 87

DeVore, C. R.: 2000, *ApJ* **539(2)**, 944

Driel-Gesztelyi, L. and Green, L.: 2015, *Living Reviews in Solar Physics* 12

D'Silva, S. and Choudhuri, A. R.: 1993, *A&A* **272**, 621

Duan, A., Jiang, C., Toriumi, S., and Syntelis, P.: 2020, *ApJ* **896(1)**, L9

Fan, Y.: 2001, *ApJ* **546(1)**, 509

Fan, Y.: 2005, *ApJ* **630(1)**, 543

Fan, Y.: 2009, *Living Reviews in Solar Physics* **6(1)**, 4

Fan, Y., Fisher, G. H., and McClymont, A. N.: 1994, *ApJ* **436**, 907

Fan, Y. and Gibson, S. E.: 2004, *ApJ* **609(2)**, 1123

Fan, Y. and Gong, D.: 2000, *Sol. Phys.* **192**, 141

Fan, Y., Zweibel, E. G., and Lantz, S. R.: 1998a, *ApJ* **493(1)**, 480

Fan, Y., Zweibel, E. G., Linton, M. G., and Fisher, G. H.: 1998b, *ApJ* **505(1)**, L59

Ferriz-Mas, A., Schmitt, D., and Schuessler, M.: 1994, *A&A* **289**, 949

Fisher, G. H., Fan, Y., and Howard, R. F.: 1995, *ApJ* **438**, 463

Fursyak, Y. A.: 2018, *Geomagnetism and Aeronomy* **58(8)**, 1129

Gary, G. A.: 2001, *Sol. Phys.* **203(1)**, 71

Gary, G. A. and Hagyard, M. J.: 1990, *Sol. Phys.* **126**, 21

Gilman, P. A. and Charbonneau, P.: 1999, *Washington DC American Geophysical Union Geophysical Monograph Series* **111**, 75

Gold, T. and Hoyle, F.: 1960, *MNRAS* **120**, 89

González Hernández, I., Komm, R., van Driel-Gesztelyi, L., Baker, D., Harra, L., and Howe, R.: 2013, *Journal of Physics Conference Series* **440(1)**, 012050

Gottschling, N., Schunker, H., Birch, A. C., Löptien, B., and Gizon, L.: 2021, *arXiv e-prints* p. arXiv:2105.10501

Green, L. M., López fuentes, M. C., Mandrini, C. H., Démoulin, P., Van Driel-Gesztelyi, L., and Culhane, J. L.: 2002, *Sol. Phys.* **208(1)**, 43

Griñón-Marín, A. B., Pastor Yabar, A., Liu, Y., Hoeksema, J. T., and Norton, A.: 2021, *arXiv e-prints* p. arXiv:2109.09131

Haddad, C. N.: 2009, *Cholesky factorizationCholesky Factorization*, pp 374–377, Springer US, Boston, MA

Hagino, M. and Sakurai, T.: 2004, *PASJ* **56**, 831

Hagino, M. and Sakurai, T.: 2005, *PASJ* **57**, 481

Hale, G. E.: 1908, *ApJ* **28**, 315

Hale, G. E.: 1927, *Nature* **119(3002)**, 708

Hale, G. E., Ellerman, F., Nicholson, S. B., and Joy, A. H.: 1919, *ApJ* **49**, 153

Hale, G. E. and Nicholson, S. B.: 1925, *ApJ* **62**, 270

Hao, J. and Zhang, M.: 2011, *ApJ* **733(2)**, L27

Herdiwijaya, D., Makita, M., and Anwar, B.: 1997, *PASJ* **49**, 235

Hoeksema, J. T., Liu, Y., Hayashi, K., Sun, X., Schou, J., Couvidat, S., Norton, A., Bobra, M., Centeno, R., Leka, K. D., Barnes, G., and Turmon, M.: 2014, *Sol. Phys.* **289(9)**, 3483

Holder, Z. A., Canfield, R. C., McMullen, R. A., Nandy, D., Howard, R. F., and Pevtsov, A. A.: 2004, *ApJ* **611(2)**, 1149

Hood, A. W. and Hughes, D. W.: 2011, *Physics of the Earth and Planetary Interiors* **187(3)**, 78

Howard, R. F.: 1991, *Sol. Phys.* **136**, 251

Howard, R. F.: 1992, *Sol. Phys.* **142**, 233

Howard, R. F.: 1994, *Sol. Phys.* **149**, 23

Howard, R. F.: 1996, *Sol. Phys.* **167**, 95

Hunter, J. D.: 2007, *Computing in Science & Engineering* **9(3)**, 90

Jiang, J., Cameron, R. H., and Schüssler, M.: 2014, *ApJ* **791**, 5

Karak, B. B. and Miesch, M.: 2017, *ApJ* **847**, 69

Keller, H. U. and Friedli, T. K.: 1992, *QJRAS* **33(2)**, 83

Knizhnik, K. J., Leake, J. E., Linton, M. G., and Dacie, S.: 2021, *ApJ* **907(1)**, 19

Kosovichev, A. G. and Stenflo, J. O.: 2008, *ApJ* **688(2)**, L115

Leamon, R. J., Canfield, R. C., Blehm, Z., and Pevtsov, A. A.: 2003, *ApJ* **596(2)**, L255

Leighton, R. B.: 1969, *ApJ* **156**, 1

Leka, K. D.: 1999, *Sol. Phys.* **188(1)**, 21

Leka, K. D., Canfield, R. C., McClymont, A. N., and van Driel-Gesztelyi, L.: 1996, *ApJ* **462**, 547

Leka, K. D., Fan, Y., and Barnes, G.: 2005, *ApJ* **626(2)**, 1091

Leka, K. D. and Skumanich, A.: 1999, *Sol. Phys.* **188(1)**, 3

Lin, H., Kuhn, J. R., and Coulter, R.: 2004, *ApJ* **613(2)**, L177

Longcope, D. and Choudhuri, A. R.: 2002, *Sol. Phys.* **205**, 63

Longcope, D., Linton, M., Pevtsov, A., Fisher, G., and Klapper, I.: 1999, *Washington DC American Geophysical Union Geophysical Monograph Series* **111**, 93

Longcope, D. W., Fisher, G. H., and Arendt, S.: 1996, *ApJ* **464**, 999

Longcope, D. W., Fisher, G. H., and Pevtsov, A. A.: 1998, *ApJ* **507(1)**, 417

Longcope, D. W. and Klapper, I.: 1997, *ApJ* **488(1)**, 443

Longcope, D. W. and Malanushenko, A.: 2008, *ApJ* **674(2)**, 1130

Longcope, D. W., Ravindra, B., and Barnes, G.: 2007, *ApJ* **668(1)**, 571

Longcope, D. W. and Welsch, B. T.: 2000, *ApJ* **545(2)**, 1089

López Fuentes, M. C., Démoulin, P., Mandrini, C. H., Pevtsov, A. A., and van Driel-Gesztelyi, L.: 2003, *A&A* **397**, 305

López Fuentes, M. C., Demoulin, P., Mandrini, C. H., and van Driel-Gesztelyi, L.: 2000, *ApJ* **544(1)**, 540

Luoni, M. L., Démoulin, P., Mandrini, C. H., and van Driel-Gesztelyi, L.: 2011, *Sol. Phys.* **270(1)**, 45

Manek, B. and Brummell, N.: 2021, *ApJ* **909(1)**, 72

Manek, B., Brummell, N., and Lee, D.: 2020, in M. J. P. F. G. Monteiro, R. A. García, J. Christensen-Dalsgaard, and S. W. McIntosh (eds.), *Dynamics of the Sun and Stars; Honoring the Life and Work of Michael J. Thompson*, Vol. 57 of *Astrophysics and Space Science Proceedings*, pp 133–135

Martin, S. F., Bilimoria, R., and Tracadas, P. W.: 1994, in R. J. Rutten and C. J. Schrijver (eds.), *Solar Surface Magnetism*, Vol. 433 of *NATO Advanced Study Institute (ASI) Series C*, p. 303

McClintock, B. H. and Norton, A. A.: 2013, *Sol. Phys.* **287(1-2)**, 215

McClintock, B. H. and Norton, A. A.: 2016, *ApJ* **818(1)**, 7

Mickey, D. L.: 1985, *Sol. Phys.* **97(2)**, 223

Moffatt, H. K.: 1978, *Magnetic field generation in electrically conducting fluids*, Cambridge: University Press

Moffatt, H. K. and Ricca, R. L.: 1992, *Proceedings: Mathematical and Physical Sciences* **439(1906)**, 411

Moreno-Insertis, F., Caligari, P., and Schuessler, M.: 1994, *Sol. Phys.* **153(1-2)**, 449

Moreno-Insertis, F. and Emonet, T.: 1996, *ApJ* **472**, L53

Nandy, D.: 2006, *Journal of Geophysical Research (Space Physics)* **111(A12)**, A12S01

Nandy, D., Mackay, D. H., Canfield, R. C., and Martens, P. C. H.: 2008, *Journal of Atmospheric and Solar-Terrestrial Physics* **70(2-4)**, 605

Parker, E. N.: 1955, *ApJ* **121**, 491

Parker, E. N.: 1975, *ApJ* **198**, 205

Parker, E. N.: 1993, *ApJ* **408**, 707

Pesnell, W. D., Thompson, B. J., and Chamberlin, P. C.: 2012, *Sol. Phys.* **275(1-2)**, 3

Petrovay, K., Brown, J. C., van Driel-Gesztelyi, L., Fletcher, L., Marik, M., and Stewart, G.: 1990, *Sol. Phys.* **127(1)**, 51

Pevtsov, A. A., Berger, M. A., Nindos, A., Norton, A. A., and van Driel-Gesztelyi, L.: 2014, *Space Sci. Rev.* **186(1-4)**, 285

Pevtsov, A. A. and Canfield, R. C.: 1998, *On the Origin of Helicity in Active Region Magnetic Fields*, Vol. 229, p. 85, Kluwer Academic Publishers

Pevtsov, A. A., Canfield, R. C., and Latushko, S. M.: 2001, *ApJ* **549(2)**, L261

Pevtsov, A. A., Canfield, R. C., and Metcalf, T. R.: 1994, *ApJ* **425**, L117

Pevtsov, A. A., Canfield, R. C., and Metcalf, T. R.: 1995, *ApJ* **440**, L109

Pevtsov, A. A., Canfield, R. C., Sakurai, T., and Hagino, M.: 2008, *ApJ* **677(1)**, 719

Pevtsov, A. A., Liu, Y., Virtanen, I., Bertello, L., Mursula, K., Leka, K. D., and Hughes, A. L. H.: 2021, *Journal of Space Weather and Space Climate* **11**, 14

Pipin, V. V., Zhang, H., Sokoloff, D. D., Kuzanyan, K. M., and Gao, Y.: 2013, *MNRAS* **435(3)**, 2581

Priest, E.: 2014, *Magnetohydrodynamics of the Sun*, Cambridge University Press

Rust, D. M. and Kumar, A.: 1996, *ApJ* **464**, L199

Sangeetha, C. R., Tripathi, D., and Rajaguru, S. P.: 2020, *ApJ* **895(1)**, 67

Savitzky, A. and Golay, M. J. E.: 1964, *Analytical Chemistry* **36**, 1627

Scherrer, P. H., Bogart, R. S., Bush, R. I., Hoeksema, J. T., Kosovichev, A. G., Schou, J., Rosenberg, W., Springer, L., Tarbell, T. D., Title, A., Wolfson, C. J., Zayer, I., and MDI Engineering Team: 1995, *Sol. Phys.* **162**, 129

Scherrer, P. H., Schou, J., Bush, R. I., Kosovichev, A. G., Bogart, R. S., Hoeksema, J. T., Liu, Y., Duvall, T. L., Zhao, J., Title, A. M., Schrijver, C. J., Tarbell, T. D., and Tomczyk, S.: 2012, *Sol. Phys.* **275(1-2)**, 207

Schmidt, H. U.: 1968, in K. O. Kiepenheuer (ed.), *Structure and Development of Solar Active Regions*, Vol. 35, p. 95

Schou, J., Antia, H. M., Basu, S., Bogart, R. S., Bush, R. I., Chitre, S. M., Christensen-Dalsgaard, J., Di Mauro, M. P., Dziembowski, W. A., Eff-Darwich, A., Gough, D. O., Haber, D. A., Hoeksema, J. T., Howe, R., Korzennik, S. G., Kosovichev, A. G., Larsen, R. M., Pijpers, F. P., Scherrer, P. H., Sekii, T., Tarbell, T. D., Title, A. M., Thompson, M. J., and Toomre, J.: 1998, *ApJ* **505(1)**, 390

Schuessler, M.: 1979, *A&A* **71(1-2)**, 79

Schunker, H., Birch, A. C., Cameron, R. H., Braun, D. C., Gizon, L., and Burston, R. B.: 2019, *A&A* **625**, A53

Schunker, H., Braun, D. C., Birch, A. C., Burston, R. B., and Gizon, L.: 2016, *A&A*

Schwabe, M.: 1843, *Astronomische Nachrichten* **20(17)**, 283

Seehafer, N.: 1990, *Sol. Phys.* **125(2)**, 219

Seehafer, N.: 1996, *Phys. Rev. E* **53(1)**, 1283

Sivaraman, K. R., Gupta, S. S., and Howard, R. F.: 1999, *Sol. Phys.* **189(1)**, 69

Snodgrass, H. B.: 1984, *Sol. Phys.* **94**, 13

Socas-Navarro, H.: 2005, *ApJ* **631(2)**, L167

Solanki, S. K., Barthol, P., Danilovic, S., Feller, A., Gandorfer, A., Hirzberger, J., Riethmüller, T. L., Schüssler, M., Bonet, J. A., Martínez Pillet, V., del Toro Iniesta, J. C., Domingo, V., Palacios, J., Knölker, M., Bello González, N., Berkefeld, T., Franz, M., Schmidt, W., and Title, A. M.: 2010, *ApJ* **723(2)**, L127

Solanki, S. K., Riethmüller, T. L., Barthol, P., Danilovic, S., Deutsch, W., Doerr, H. P., Feller, A., Gandorfer, A., Germerott, D., Gizon, L., Grauf, B., Heerlein, K., Hirzberger, J., Kolleck, M., Lagg, A., Meller, R., Tomasch, G., van Noort, M., Blanco Rodríguez, J., Gasent Blesa, J. L., Balaguer Jiménez, M., Del Toro Iniesta, J. C., López Jiménez, A. C., Orozco Suarez, D., Berkefeld, T., Halbgewachs, C., Schmidt, W., Álvarez-Herrero, A., Sabau-Graziati, L., Pérez Grande, I., Martínez Pillet, V., Card, G., Centeno, R., Knölker, M., and Lecinski, A.: 2017, *ApJS* **229(1)**, 2

Spoerer, F. W. G. and Maunder, E. W.: 1890, *MNRAS* **50**, 251

Stenflo, J. O. and Kosovichev, A. G.: 2012, *ApJ* **745(2)**, 129

Su, J. T., Sakurai, T., Suematsu, Y., Hagino, M., and Liu, Y.: 2009, *ApJ* **697(2)**, L103

Tang, F., Howard, R., and Adkins, J. M.: 1984, *Sol. Phys.* **91(1)**, 75

Tian, L. and Alexander, D.: 2009, *ApJ* **695(2)**, 1012

Tian, L., Bao, S., Zhang, H., and Wang, H.: 2001, *A&A* **374**, 294

Tian, L. and Liu, Y.: 2003, *A&A* **407**, L13

Tiwari, S. K., Venkatakrishnan, P., Gosain, S., and Joshi, J.: 2009a, *ApJ* **700(1)**, 199

Tiwari, S. K., Venkatakrishnan, P., Gosain, S., and Joshi, J.: 2009b, *ApJ* **700(1)**, 199

Tlatov, A., Illarionov, E., Sokoloff, D., and Pipin, V.: 2013, *MNRAS* **432(4)**, 2975

Török, T. and Kliem, B.: 2003, *A&A* **406**, 1043

Török, T., Kliem, B., and Titov, V. S.: 2004, *A&A* **413**, L27

Tóth, L. and Gerlei, O.: 2004, *Sol. Phys.* **220**, 43

Valori, G., Kliem, B., and Keppens, R.: 2005, *A&A* **433(1)**, 335

Van Der Walt, S., Colbert, S. C., and Varoquaux, G.: 2011, *Computing in Science & Engineering* **13(2)**, 22

van Driel-Gesztelyi, L. and Petrovay, K.: 1990, *Sol. Phys.* **126(2)**, 285

Virtanen, P., Gommers, R., Oliphant, T. E., Haberland, M., Reddy, T., Cournapeau, D., Burovski, E., Peterson, P., Weckesser, W., Bright, J., van der Walt, S. J., Brett, M., Wilson, J., Millman, K. J., Mayorov, N., Nelson, A. R. J., Jones, E., Kern, R., Larson, E., Carey, C. J., Polat, İ., Feng, Y., Moore, E. W., VanderPlas, J., Laxalde, D., Perktold, J., Cimrman, R., Henriksen, I., Quintero, E. A., Harris, C. R., Archibald, A. M., Ribeiro, A. H., Pedregosa, F., van Mulbregt, P., and SciPy 1.0 Contributors: 2020, *Nature Methods* **17**, 261

Wang, J., Yan, X., Kong, D., Xue, Z., Yang, L., Li, Q., Zhang, Y., and Li, H.: 2021, *arXiv e-prints* p. arXiv:2106.02786

Wang, Y. M.: 2013, *ApJ* **775(2)**, L46

Wang, Y. M. and Sheeley, N. R., J.: 1989, *Sol. Phys.* **124(1)**, 81

Wang, Y. M. and Sheeley, N. R., J.: 1991, *ApJ* **375**, 761

Webb, G.: 2018, *Magnetohydrodynamics and Fluid Dynamics: Action Principles and Conservation Laws*, Springer Nature

Weber, M. A., Fan, Y., and Miesch, M. S.: 2011, *ApJ* **741(1)**, 11

Weber, M. A., Fan, Y., and Miesch, M. S.: 2013, *Sol. Phys.* **287**, 239

Welsch, B. T., Abbett, W. P., De Rosa, M. L., Fisher, G. H., Georgoulis, M. K., Kusano, K., Longcope, D. W., Ravindra, B., and Schuck, P. W.: 2007, *ApJ* **670(2)**, 1434

Wiegelmann, T. and Sakurai, T.: 2012, *Living Reviews in Solar Physics* **9(1)**, 5

Wolf, R. and Brunner, W.: 1930, *Astronomische Mitteilungen der Eidgenössischen Sternwarte Zurich* **13**, 67

Woltjer, L.: 1958, *Proceedings of the National Academy of Science* **44(6)**, 489

Wright, A. N. and Berger, M. A.: 1989, *J. Geophys. Res.* **94(A2)**, 1295

Xu, Z.-t.: 1980, *Chinese Astronomy* **4(4)**, 406

Yeates, A. R., Mackay, D. H., and van Ballegooijen, A. A.: 2008, *Sol. Phys.* **247(1)**, 103

Yeo, K. L., Feller, A., Solanki, S. K., Couvidat, S., Danilovic, S., and Krivova, N. A.: 2014, *A&A* **561**, A22

Zeeman, P.: 1897, *Nature* **55**, 347

Zhang, H. and Bao, S.: 1998, *A&A* **339**, 880

Zhang, H., Sakurai, T., Pevtsov, A., Gao, Y., Xu, H., Sokoloff, D. D., and Kuzanyan, K.: 2010, *MNRAS* **402(1)**, L30

Zhang, M.: 2006, *ApJ* **646(1)**, L85

Zwaan, C.: 1981, *Solar magnetic structure and the solar activity cycle. Review of observational data.*, Vol. 450, pp 163–179, NASA

Appendix

A List of active regions used in chapter 4

This is a list with the NOAA number of active regions that I used in chapter 4 to characterize measurements of α_z:

11066,11070,11072,11074,11075,11076,11079,11080,11086,11088,11103,11105,11114,11116,11122,11130,11132,11136,11137,11138,11141,11142,11143,11145,11146,11148,11152,11156,11159,11167,11174,11198,11199,11200,11206,11209,11211,11214,11222,11223,11241,11242,11267,11288,11294,11297,11300,11304,11310,11311,11318,11322,11327,11334,11370,11385,11396,11397,11404,11406,11414,11416,11431,11437,11446,11449,11450,11456,11472,11497,11500,11510,11511,11523,11531,11547,11549,11551,11554,11560,11561,11570,11597,11603,11605,11607,11624,11627,11631,11640,11645,11670,11675,11680,11686,11696,11697,11699,11702,11703,11707,11712,11736,11750,11752,11764,11776,11781,11784,11786,11789,11807,11813,11824,11829,11831,11842,11843,11849,11855,11867,11874,11878,11886,11894,11902,11910,11911,11915,11922,11924,11932,11945,11946,11951,11962,11969,11978,11988,11992,12011,12029,12039,12041,12062,12064,12078,12089,12098,12105,12118,12119

Scientific contributions

Refereed publications

- H. Schunker, **C. Baumgartner**, A.C. Birch, R.H. Cameron, D.C. Braun and L. Gizon: *Average motion of emerging solar active region polarities II. Joy's law*, Astronomy and Astrophysics, 640, A116 (2020)

Accepted publications

- **C. Baumgartner**, A.C. Birch, H. Schunker, R.H. Cameron and L. Gizon: *Impact of spatially correlated fluctuations in sunspots on metrics related to magnetic twist*, accepted by A&A (17.03.2022)

Conference proceedings

- European Solar Physics Meeting 16, online, 6 - 10 September 2021
  Poster & Talk: *Towards measuring magnetic twist in active regions using SDO/HMI*

Acknowledgements

First of all, I want to thank my supervisor Laurent Gizon for providing me with the opportunity to carry out my PhD studies at the Max-Planck Institute for Solar System Research and the International Max Planck Research School (IMPRS). In this context, I also want to thank the IMPRS coordinator Sonja Schuh, who always has an open ear for problems and guides us students through the organizational paperwork.

I am deeply indebted to my day-to-day supervisors Aaron Birch and Hannah Schunker, who guided me patiently through the last three years. This thesis would not have been possible without their support. I also want to thank Robert Cameron and Jesper Schou for many fruitful discussions and helpful insights.

I must also thank my thesis advisory committee member Natalie Krivova for assessing and assuring the progress of my PhD studies. I want to express my gratitude to Stefan Dreizler for being the second referee of my thesis and Wolfram Kollatschny, Hardi Peter, Ramin Yahyapour and Thorsten Hohage for being in my defense committee.

I cannot begin to express my thanks to all the friends that I found during my time in Göttingen, who's friendship - especially during times with COVID - helped me keeping my sanity. In particular, I want to thank Juxhin Zhuleku and Valentin Bickel for the countless enjoyable times that we spent at FIZ or in Thanners, Felix Mackebrandt and Nils Gottschling for all the talks, discussions and memorable cooking sessions we had, Manuel Reinhardt for talking care of my plants, when I could not, and introducing me to Doppelkopf and my fellow Austrians Bernhard Hofer, Stephan Heinemann and Bastian Proxauf, with whom I spent many enjoyable gaming evenings. Many thanks also go to all the current and former members of the institute's band MegaGauss, with whom I had the pleasure to play with. All of you made Göttingen feel like a second home.

My deepest gratitude go to my parents and family for their never ending love, continuous support and without whom I would never have enjoyed so many opportunities.

Curriculum vitae

Personal Data

Name	Christian Baumgartner
Date of Birth	20 May 1989
Place of Birth	Wolfsberg, Austria
Nationality	Austrian

Education

PhD student

Sep. 2018 - Dez. 2021	at the International Max Planck Research School at the University of Göttingen and the Max Planck Institute for Solar System Research, Göttingen, Germany
Thesis	*The tilt and twist of emerging solar active regions*
Advisors	Prof. Dr. Laurent Gizon, Dr. Aaron Birch, Dr. Natalie Krivova, Dr. Hannah Schunker

M.Sc. in Astrophysics

Oct. 2015 - Apr. 2018	at the Karl-Franzens University, Graz, Austria
Thesis	*On the factors determining the eruptive character of solar flares*
Advisors	Assoz. Prof. Dr. Astrid Veronig, Dr. Julia Thalmann

B.Sc. in Physics

Sep. 2012 - Oct. 2015	at the Karl-Franzens University, Graz, Austria
Thesis	*Fundamentals of climate modeling*
Advisors	Dr. Ulrich Foelsche